学位論文

Ultrafast dynamics of reversible photoinduced phase transitions

in optically switching functional materials

$$\left(\begin{array}{c} \text{光スイッチング機能性物質における} \\ \text{可逆的光誘起相転移の超高速ダイナミクス} \end{array} \right)$$

平成 26 年 12 月博士（理学）申請

東京大学大学院理学系研究科 物理学専攻

浅原　彰文

Abstract

Optical control of the electronic, magnetic, and optical properties of solids via photoinduced phase transition (PIPT) has been of great interest in materials science and technology. Ultrafast switching phenomena caused by PIPT have been particularly important, because of their potential applications utilizing the drastic and permanent changes in physical properties within ultrafast time scales; these features should be applicable directly to quickly rewritable optical data storages and quickly operating switching devices. Furthermore, from the viewpoint of fundamental physics, ultrafast PIPT is an important issue to understand the nonequilibrium relaxation dynamics in solids. In relation with the development of various types of PIPT materials, their properties and optical responses have been studied in order to understand their underlying mechanisms and improve their functionalities. Ultrafast spectroscopy directly observing the PIPT dynamics is especially useful to investigate such complicated phenomena.

Based on this background, we have focused on two novel photo-functional materials, rubidium manganese hexacyanoferrate ($RbMn[Fe(CN)_6]$) and nano-granular trititanium pentaoxide (Ti_3O_5). First, $RbMn[Fe(CN)_6]$ is one of Prussian blue analogues, and has been well known for its various photo-functionalities. Particularly, this material has been attracting much attention for the unique ferromagnetic-antiferromagnetic phase switching phenomenon between LTP (low-temperature phase: Fe^{2+}-CN-Mn^{3+}) and PIHTP (photoinduced high-temperature phase: Fe^{3+}-CN-Mn^{2+}) triggered by optically-induced charge transfer. Second, nano-granular Ti_3O_5 is an optical switching oxide showing a metal-semiconductor phase transitions between λ-Ti_3O_5 and β-Ti_3O_5 at room temperature. This novel functionality was the first example achieved in oxides, and then, this material has been greatly expected as a new optical storage material. In these two materials, although their uniqueness and importance of the reversible PIPTs have been recognized, their mechanism and dynamics have been remained unclear. In order to understand these switching phenomena, it is essential to investigate the underlying microscopic changes by probing them from various aspects.

In this thesis, we present the studies on the PIPT dynamics and the optical properties in these two optical switching materials. At first, the dynamics of the reversible PIPTs in $RbMn[Fe(CN)_6]$ was investigated by time-resolved CN vibration spectroscopy. By monitoring the CN stretching vibration modes, which are sensitive to the valence states of the adjacent metal ions, we could quantify not only LTP (Fe^{2+}-CN-Mn^{3+}) and PIHTP (Fe^{3+}-CN-Mn^{2+}) but also the domain boundary configurations between the two phases (Fe^{2+}-CN-Mn^{2+} and Fe^{3+}-CN-Mn^{3+}). As a result, we observed not only the instantaneous charge transfer but also the fast generation of the boundary configuration, suggesting that relatively small domains and/or low-dimensional fjord-like domains are created at the early stage of the transition. This is the first demonstration detecting the nucleation process by directly observing phase boundaries. Furthermore, by irradiating the sample with another light inducing the reverse process to the pump light simultaneously, we demonstrated a pump-probe measurement under the condition where the persistent phase transitions occur.

In addition, the magnetic dynamics in the charge transferred PIPTs in $RbMn[Fe(CN)_6]$ was investigated by time-resolved Faraday rotation spectroscopy. By comparing the results with those from time-resolved absorption spectroscopy, it was suggested that the paramagnetic spin system follows the instantaneous changes in the electronic system, while the lattice system slowly relaxes taking about 90 ps. From these experiments, the electronic, structural, and spin dynamics in the picosecond region in $RbMn[Fe(CN)_6]$ were characterized.

Next, properties in nano-granular Ti_3O_5 were investigated. We first studied terahertz (THz) optical conductivity in this material by THz time domain spectroscopy (THz-TDS). This information is important because Ti_3O_5 shows metal-semiconductor transition, and because the conductivity in nanoparticles is well characterized in the THz frequency range. From fitting analyses, the THz optical conductivity obtained from nano-granular Ti_3O_5 was well reproduced by the Drude-Smith model, which is an extended Drude model characterizing conductivity in nanoparticles. The origin was attributed to the hopping conduction between Ti_3O_5 nanoparticles.

The PIPT dynamics in nano-granular Ti_3O_5 was investigated by time-resolved diffuse reflection spectroscopy. Here, the dynamics of the semiconductor-to-metal transition (β-Ti_3O_5 $\rightarrow$ λ-Ti_3O_5) was mainly characterized. With the time-resolved measurement conducted over a wide range of time scales, from femto- to microseconds, the entire transient behavior was revealed. Based on a detailed spectral analysis, we proposed a model of the PIPT dynamics that the semiconductor-to-metal phase transition occurs within a few hundreds of femtoseconds, and the transient state lasts till several hundreds of microseconds. In the PIPT process, we particularly note that this ultrafast onset and the subsequent λ-phase stabilization process of faster than 10 ps indicate the applicability of this material to ultrafast photo-switching.

In this way, the transient responses in PIPTs of $RbMn[Fe(CN)_6]$ and nano-granular Ti_3O_5 were characterized for the first time. The knowledge obtained here is fundamental in applications and further material developments. In addition, it will lead to the development of new methods measuring persistent phase transitions, and to understanding of similar PIPT materials. We hope our results further promote the research field on PIPT.

Contents

Chapter 1

Introduction

In this thesis, photoinduced phase transitions (PIPTs) in optically switching functional materials are discussed. First of all, the overview of PIPT phenomenon is presented. The basic concept of PIPT is explained by the renowned phenomenological model constructed in early 2000s, and the historical background of PIPT research is reviewed. Subsequently, the concept of optical switching materials is summarized. At the end of this chapter, the objective and the outline of this thesis are described.

1.1   Photoinduced phase transition (PIPT)

1.1.1   Concept of PIPT

PIPT is the phase transition phenomenon induced by optical stimulation. This research field has been particularly promoted since 1990s with the development of ultrafast spectroscopy. Since PIPT enables ultrafast optical control of physical properties of solids, it has potential applications for a variety of ultrafast devices. Furthermore, since PIPT includes nonequilibrium and cooperative relaxation dynamics in solids, it is an important issue from the viewpoint of fundamental solid state physics.

Before explaining the concept of PIPT, that of "phase transition" is briefly introduced. In general, material stabilizes so as to decrease its Helmholtz free energy by changing its state. In some conditions, a group of particles in materials (nuclei, electrons including spin states, etc.) gets ordered through cooperative interactions, and some macroscopic physical properties
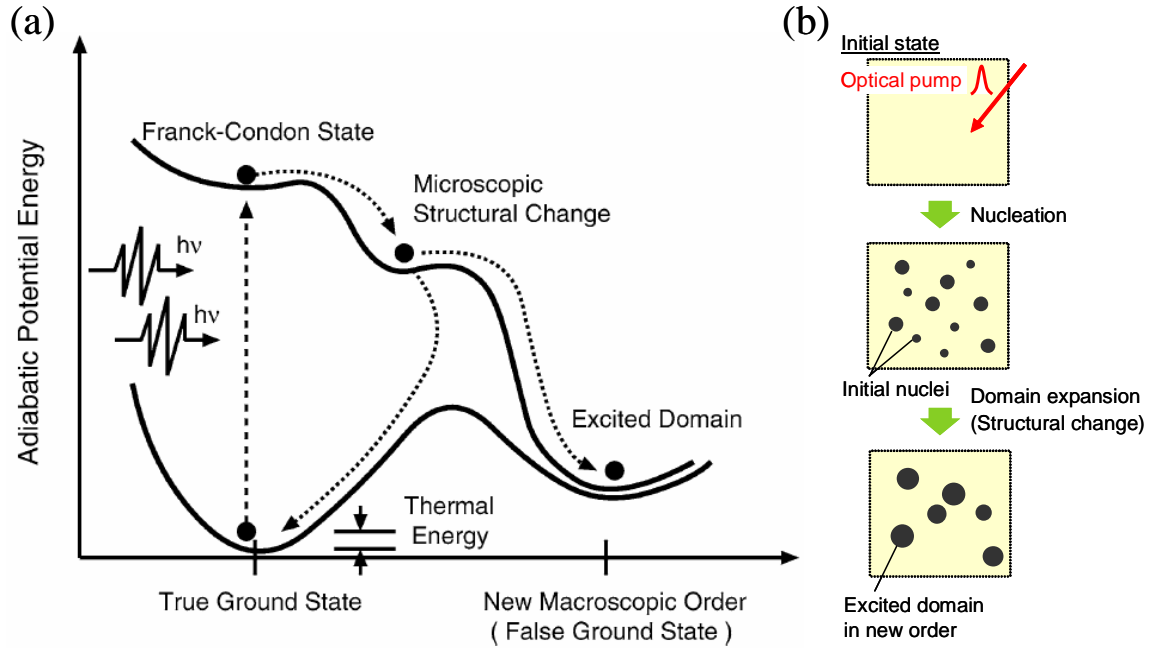
Fig. 1.1: (a) Schematic diagram of PIPT dynamics proposed by Nasu *et al.* [3]. (b) Macroscopic illustration of the PIPT dynamics.

arise. Such a collectively stabilized state can be regarded as a kind of "phase". By applying some external stimuli such as thermal energy, the collective order (phase) can be melted or frozen, inducing drastic changes of the macroscopic properties; this is the phase transition [1]. Depending on the type of materials, a variety of phase transitions can be observed, such as crystal structure, conductivity, magnetism, superconductivity, and so on.

In PIPT, such a drastic change of material property is triggered by optical pumping. The concept has been generally understood by a phenomenological model proposed by Nasu *et al.* [2, 3]. Figure 1.1(a) shows PIPT processes on the schematic energy (adiabatic or free energy) diagram. Here, the vertical axis is equivalent to the adiabatic potential energy in a microscopic viewpoint. The horizontal axis corresponds to a kind of order parameter (the configuration coordinate for structural phase transition, or magnetization for magnetic phase transition, etc.). When photon energy is absorbed by the material, the true ground state located at the minimum of free energy is vertically excited to the Frank-Condon state. This electronic excitation process occurs in a time scale of 10^{-15} s, which is nearly the reciprocal of the excitation photon energy ($\sim \hbar/E$; $E =\sim$eV with visible light). Since this process is too fast, other configurations such as lattice are frozen in this time scale. The Frank-Condon state with

2

high excess energy is unstable, thus, it relaxes to stabler states accompanying microscopic structural changes. Through the relaxation process, a part of the excited state reverts to the initial state, while another part establishes new hidden macroscopic order. The new order prevails via the inherent cooperative interaction so-called a domino effect, and excited domains are created. This metastable state or the "false ground' state" is located at a local minimum of free energy and is separated from the true ground state with the energy barrier higher than the thermal energy. Therefore, the new phase is kept stable (or metastable) there. In this way, the overall PIPT processes are accomplished.

From a macroscopic viewpoint, these processes can be explained in real space as shown in Fig. 1.1(b). When the true ground state is optically excited, after a short time, small domains with microscopic structural changes are randomly created. This newly created states correspond to the embryonic nuclei from which the PIPT process starts. Generally in phase transitions, domains smaller than some critical size are apt to disappear, while those larger than the critical size expand, resulting from the balance between the loss due to surface energy and the gain due to bulk energy [1]. As a result, relatively large nuclei cooperatively expand, and the stable domains with new macroscopic order are created. These are the phenomenological interpretation of PIPT.

As expected from this model, PIPT materials need to have multiple potential minima separated as expressed in Fig. 1.1(a). The energy barrier located between the stable (or metastable) states enables the newly created domain to be stable. This is one of the most important conditions in designing PIPT materials.

In addition, another important feature of PIPT is that nonlinear phenomena can be observed, such as threshold behavior or incubation time for the excitation fluence or time. This arises because PIPT materials include the critical process creating domains as mentioned above. It is noticeable that by investigating such nonlinear phenomena experimentally, we can obtain information which helps us to comprehend the underlying PIPT mechanism.

1.1.2 Research Background of PIPT

History of PIPT research

Historically, the PIPT research started from the report on LIESST (Light Induced Excited Spin State Trapping) phenomenon in spin-crossover complexes in 1984 [4]. In 1990s, PIPT research has been greatly promoted with the development of ultrafast lasers. There were two pioneering

works in this research field. One is about TTF-CA (tetrathiafulvalene-p-chloranil) [5–7], where the transient PIPT from the ground state to a metastable phase was firstly demonstrated in the neutral-ionic phase transition. Another is about a π-conjugated polymer, polydiacetylenes [8, 9], where PIPT from a metastable phase to the ground state was firstly demonstrated in the reversible structural phase transition. Additionally, in these researches, cooperative phenomena such as dynamical domain expansion were observed.

Inspired by them, PIPT researches have been vigorously performed. In particular strongly-correlated materials (transition metal oxides, metal complexes, and low-dimensional organic conductors, etc.) have been studied, because their competing electron-phonon (or electron-spin) correlations often cause a variety of metastable phases. As a representative example, the charge-ordered insulator-to-metal PIPT observed in a manganese oxide [10, 11] was paid much attention. To date, PIPT phenomena have been reported in a wide variety of materials. For example, insulator-metal phase transitions in organic complex $(EDO\text{-}TTF)_2PF_6$ [12, 13], or in transition metal oxides like VO_2 [14–16] were reported. Photoinduced superconducting transition in $YBa_2Cu_3O_{6+x}$ [17, 18] was also reported. Furthermore, in $Pr_{0.7}Ca_{0.3}MnO_3$, PIPT was achieved by direct excitation of the lattice vibration modes with infrared light [19]. These examples are just a part of various PIPT materials. The characteristics of PIPTs greatly differ from each other depending on the materials.

Associated with the development of the experiment, theoretical studies have also made progress since the late 1990s. For example, the first principle calculation in spin-crossover material was performed [20, 21]. In the early 2000s, the phenomenological interpretation of PIPT was given by Nasu [2, 3] which was described in the previous section. In 2009, an innovative idea was proposed that diamond structure is created from graphite via PIPT [22, 23]. Recently, a domain expansion process was also studied by using Monte Carlo simulation [24–26]. Through these researches, understanding of the nature of PIPT phenomenon has been gradually progressed.

As mentioned in this section, the PIPT research has progressed from both of experimental and theoretical aspects. In the future, this research area will be evolved with the development of the related technologies.
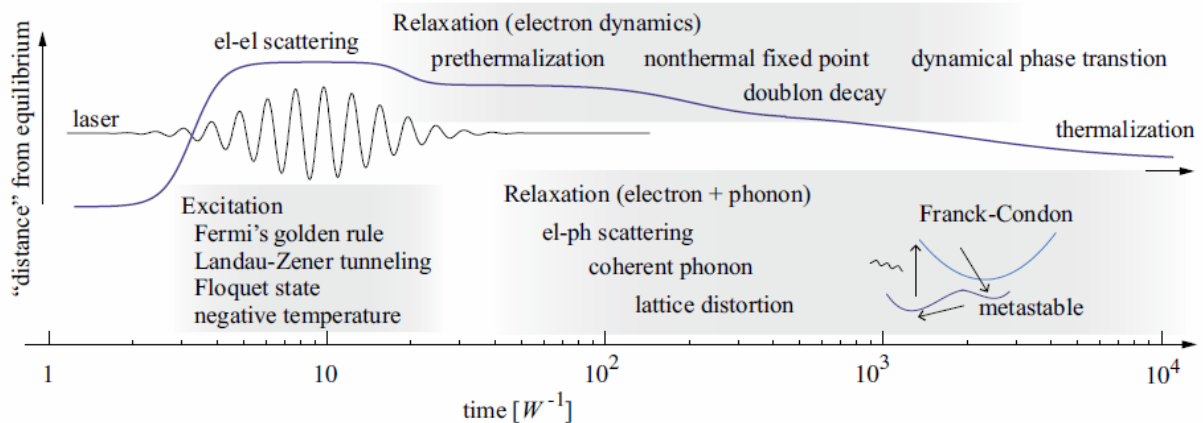
Fig. 1.2: Schematic of the nonequilibrium relaxation dynamics in photoinduced phenomena in solids, which was summarized by Aoki *et al*. [27]. Here, the time scale is rescaled corresponding to the energies of the phenomena. Typically, the time scale of electron-electron scattering roughly lies on the order of 10 fs, and that of electron-phonon scattering is longer than several 100 fs.

Role of ultrafast spectroscopy in PIPT research

Ultrafast spectroscopy has been taking an important role in PIPT researches. Particularly, the spread of the Ti:sapphire femtosecond laser and the optical parametric amplifier in 1990s helped the remarkable development of this research field. The merit of ultrafast spectroscopy is that the relaxation processes in PIPT can be directly traced by time-resolved measurements. By using this advantage, the PIPT dynamics has been studied in order to understand their underlying mechanisms and to improve their functionality.

As discussed in Fig. 1.1, the PIPT mechanism has been understood phenomenologically without considering the detailed processes connecting the true and false ground states. However, in actuality, the dynamics is very complicated, because various types of relaxation processes (or collective interactions) are entangled as shown in Fig. 1.2 [27]. Here, the time scales of these processes are approximated by the reciprocal of the interaction energies. On the rescaled time axis in Fig. 1.2, for example, the typical time scale of electron-electron scattering roughly lies on the order of 10 fs, and that of electron-phonon scattering is around several 100 fs. In order to understand such complicated phenomena, it is needed to unravel the correlation between the degrees of freedom related to electronic, structural, and spin systems by observing the phenomena through various measurements. Ultrafast spectroscopy based on pump-probe measurement is especially useful, because it directly accesses to their

dynamics. The probe method should be selected depending on the target phenomena. For example, transient absorption, transient reflection, or photoelectron spectroscopy are used studying electron dynamics. Infrared absorption spectroscopy, terahertz spectroscopy, Raman scattering measurement, electron beam diffraction, or x-ray diffraction are used studying structural changes. Faraday or Kerr effect, magnetic circular dichroism (MCD), or pick-up coil method are used to probe magnetic properties. Usually, by combining the experimental results obtained from several types of measurements, feasible models are constructed to understand the PIPT mechanism.

1.2   Optical switching materials

In this research, we focus on the PIPT in optical switching materials [28–30]. Here, "optical switching materials" are defined as materials where two different states (phases) are reversibly switched by external optical stimulation. Their electronic, structural, and magnetic properties are optically changed by PIPT. Because the drastic and permanent changes in their physical properties within ultrafast time scales are caused by PIPT, optical switching materials have potential applications to high speed rewritable optical data storages and quickly operating switching devices.

To date, optical switching materials having various types of functionalities have been developed.   As the most typical example, a chalcogenide, GeSbTe (GST) showing crystalline-amorphous switching [31, 32] has been well known as the base material of the rewritable data storage media.   For other examples, photochromic compounds showing light-induced structural switching [33, 34], spin-crossover metal complexes showing reversible LIESST [35, 36], and cyano-bridged assemblies showing reversible photomagnetism [37–39] etc. have been discovered.

In order to design good optical switching materials, there are generally two conditions; (i) existence of bistability in the system and (ii) small structural deformation accompanied by the switching process. (i) The bistability helps each phase to be stably trapped at the corresponding states, as mentioned in the previous section. (ii) The small structural change is also required. If the structural change between the two different states is too large, the phase change is difficult to occur due to their high energy barrier. Even if the phase change occurs, such large deformation will break the material after repetitive switching processes. However, if the structural change

6

is too small, the excited state cannot be trapped and immediately reverts to the ground state. Therefore, moderately small structural change (or moderate strength of cooperative interaction) is essential to realize good optical switching performance. These are important keys to develop optical switching materials.

1.3 Motivation of this research

In researches on optical switching materials, generally, the static properties in initial and final states are to be investigated first. However, the excited states or the relaxation dynamics are not so clear due to their inherent complexity, though they provide information essential for understanding the switching (and PIPT) mechanism. Researches on such dynamics are important for application and development of optical functional materials. Also from the viewpoint of the fundamental physics, it is important for understanding the nonequilibrium and cooperative relaxation dynamics in solids.

In this research, we have focused on two optical switching materials, $RbMn[Fe(CN)_6]$ and nano-granular Ti_3O_5. $RbMn[Fe(CN)_6]$ shows the photoinduced ferromagnetic-antiferromagnetic switching, which is the first example of optical switching between a ferromagnet and an antiferromagnet. Nano-granular Ti_3O_5 shows the photoinduced metal-semiconductor transitions, which is the first example of optical switching metal oxide at room temperature. In these two materials, although the uniqueness and importance of the reversible PIPTs have been recognized, their dynamical mechanisms have remained unclear. The main purpose of this research is to study the PIPT dynamics in these switching phenomena, and to elucidate the transient responses, leading to the comprehension of their underlying PIPT mechanisms.

1.4 Outline of this thesis

After this introduction (Chapter 1), the rest of this thesis is composed of three parts. Part I, II, and III are devoted to $RbMn[Fe(CN)_6]$, nano-granular Ti_3O_5, and Summary, respectively.

First, in Part I (Chapters 2-4), researches on $RbMn[Fe(CN)_6]$ are described. In Chapter 2, the background on $RbMn[Fe(CN)_6]$, its properties and the relevant previous researches etc., are summarized. In Chapter 3, the dynamics of the reversible PIPTs in $RbMn[Fe(CN)_6]$ is

studied by time-resolved CN vibration spectroscopy. Herein, the transient charge transfer and the fast nucleation process in the PIPTs are discussed. In Chapter 4, the magnetic dynamics accompanied by the charge transferred PIPTs in RbMn[Fe(CN)$_6$] is investigated by time-resolved Faraday rotation spectroscopy.

Second, in Part II (Chapters 5-7), researches on nano-granular Ti$_3$O$_5$ are described. In Chapter 5, the previous reports and the properties on Ti$_3$O$_5$ are summarized. In Chapter 6, THz optical conductivity in nano-granular Ti$_3$O$_5$ is studied by THz time-domain spectroscopy and the fitting analysis with the Drude-Smith model. In Chapter 7, the PIPT dynamics in nano-granular Ti$_3$O$_5$ is studied by time-resolved diffuse reflection spectroscopy. The entire transient behavior is discussed with the measurement conducted over a wide range of time scales, and a PIPT scenario is proposed.

Finally, in Part III (Chapter 8), the conclusion throughout this thesis is described, and the future prospects are discussed.

Part I

RbMn[Fe(CN)$_6$]

Chapter 2

Background: RbMn[Fe(CN)$_6$]

In this research, we selected rubidium manganese hexacyanoferrate (RbMn[Fe(CN)$_6$]) as the target material. The main reason of this selection is that RbMn[Fe(CN)$_6$] has a wide variety of multi-functionalities as will be described later and has been vigorously investigated, and thus, this material should be suitable for studying the fundamental features of the PIPTs in cyano-bridged metal complexes.

In this chapter, the previous studies on cyano-bridged metal complexes and the properties of RbMn[Fe(CN)$_6$] are summarized. The knowledge will be useful to understand the experimental results discussed in the following chapters. At the end of this chapter, the motivation of this study is described.

2.1 Cyano-bridged metal complexes

First, we introduce cyano-bridged metal complexes (hereafter, we call it as cyano-complexes). Cyano-complexes are a kind of mixed valence complexes, and their composition formula is expressed as $A_x M[M'(\mathrm{CN})_6]_3 \cdot x\mathrm{H}_2\mathrm{O}$ (A: alkali metal, M, M': transition metal). This material group is also called Prussian blue analogues (PBA), because one of the members $\mathrm{Fe}_4[\mathrm{Fe}(\mathrm{CN})_6]_3 \cdot x\mathrm{H}_2\mathrm{O}$ has been one of the most important blue dyes in the art history since the 18th century. As for their structure, transition metal ions bridged by CN^- ligands construct a three- (or two-) dimensional lattice network. In some cases, alkali metal ions are placed on the interstitial sites of the lattice. Figure 2.1 shows some examples of the cyano-complexes; (a) Mn-Fe [38, 39] and (b) Co-Fe cyano-complexes [40–42] have typical three-dimensional
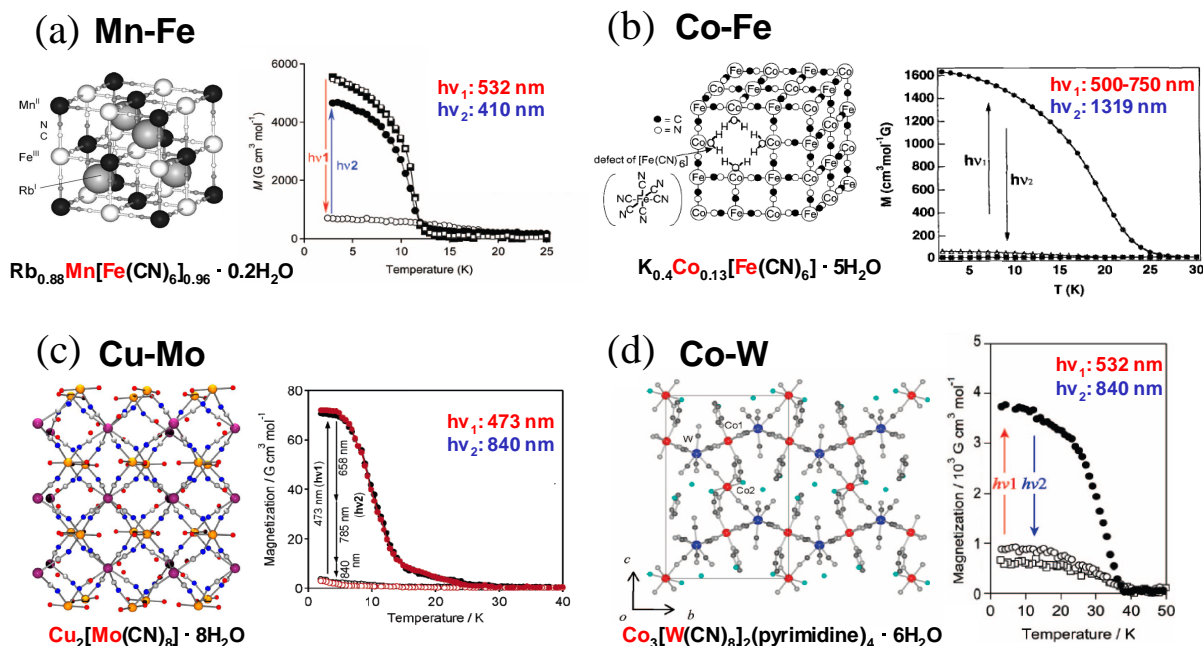
Fig. 2.1: Examples of cyano complexes showing reversible magnetic PIPTs. Their crystal structure (left side) and the magnetization changes induced by temperature and optical excitations (right side) in (a) $Rb_{0.88}Mn[Fe(CN)_6]_{0.96} \cdot H_2O$ [38, 39], (b) $K_{0.4}Co_{0.13}[Fe(CN)_6] \cdot 5H_2O$ [40–42], (c) $Cu_2[Mo(CN)_8] \cdot 8H_2O$ [43–45], and (d) $Co_3[W(CN)_8]_2(pyrimidine)_4 \cdot 6H_2O$ [46–49]. These materials show the ferro- (or ferri-) magnetic phase transition at low temperatures in common.

cubic structures, while (c) the Cu-Mo cyano-complex [43–45] has a three-dimensional structure constructed by Mo ions with 8 CN^- ligands, and (d) the Co-W cyano-complex [46–49] has a complex two-dimensional structure. Their electronic, structural, and magnetic characteristics are greatly modified by changing their composition, the morphology (the size or shape), or stoichiometry (the amount of defects). Furthermore, in cyano-complexes, charge transfer between the metal ions tends to occur by external stimulations, such as thermal energy or photon absorption, indicating that charge-transfer-typed PIPT is likely to occur in cyano-complexes. Therefore, we can design a wide variety of PIPT materials in cyano-complexes, meaning that this material group provides a suitable platform for the research field of PIPT.

To date, cyano-complexes having various types of interesting functionalities have been developed; for instance, photo-switched chirality [50], photoinduced magnetic pole inversion [51], moisture sensitive phase transition [52] etc. Reversible phase transitions, which we are

focusing in this thesis, have been reported in some cyano-complexes such as Mn-Fe [38, 39], Co-Fe [40–42], Cu-Mo [43–45], Co-W [46–49] cyano-complexes. Figure 2.1 summarizes the characteristics of the reversible magnetic PIPTs in these materials. Here, the crystal structure is shown in the left side, and the temperature dependence of the magnetization M is in the right side. From these figures, it is found that the photoinduced ferro- (or ferri-) magnetic phase transitions occur at low temperatures. Although the details of these PIPTs depend on its compositions, they show the similar phenomena. These PIPTs have the following common features: (i) these phase transitions are triggered by photoinduced charge transfer between their metal ions and (ii) the bidirectional switching phenomena are achieved by irradiating light at different wavelengths. The key point of this reversibility is the existence of two stable phases having different valence states, and the existence of the charge transfer absorption bands inducing phase transitions in opposite directions.

2.2 Properties of RbMn[Fe(CN)$_6$]

In this research, we selected rubidium manganese hexacyanoferrate (RbMn[Fe(CN)$_6$]) as the target material. Below, the properties of RbMn[Fe(CN)$_6$] are summarized.

2.2.1 Interesting phenomena found in RbMn[Fe(CN)$_6$]

As for RbMn[Fe(CN)$_6$], there have been a variety of previous researches. First, RbMn[Fe(CN)$_6$] shows phase transitions induced by various external stimuli. Besides temperature induced phase transition summarized later, for instance, pressure-induced phase transition [53], x-ray-induced phase transition [54], and electric-field-induced phase transition [55] have been reported. This causability of the phase transition by such various stimuli indicates that RbMn[Fe(CN)$_6$] has well-balanced bistability and is suitable for investigating PIPT phenomenon.

This material has been further fascinating because it shows other many interesting phenomena, such as simultaneous occurrence of ferroelectricity and ferromagnetism [56], negative thermal expansion rate [57], magnetic-induced second harmonic generation (MSHG) [58], and so on.

In this way, RbMn[Fe(CN)$_6$] is suitable as the research platform of PIPT and has a wide variety of multi-functionalities. Thus, we selected this material as the target material for

13
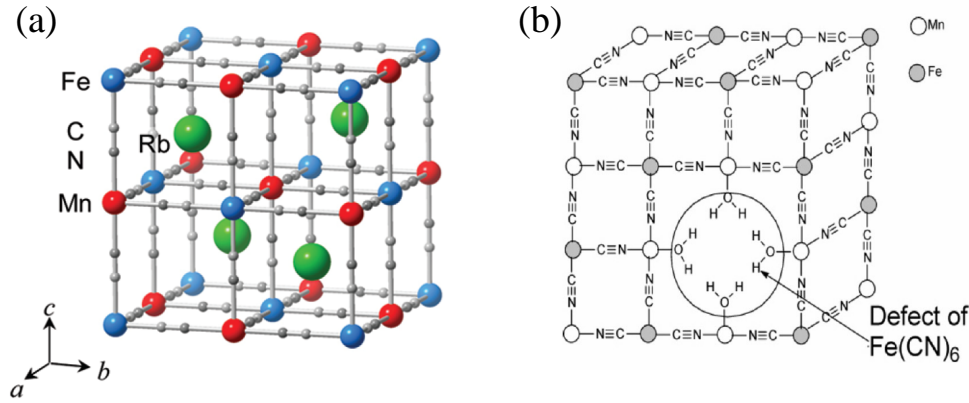
Fig. 2.2: The structures of (a) RbMn[Fe(CN)$_6$] [59, 60] and (b) Rb$_x$Mn[Fe(CN)$_6$]$_y$ $\cdot$ zH$_2$O including lattice defects [61].

studying the fundamental features of the PIPTs in cyano-bridged metal complexes.

2.2.2 Basic crystal structure

Figure 2.2(a) shows the structure of RbMn[Fe(CN)$_6$]. The precise composition formula of RbMn[Fe(CN)$_6$] is Rb$_x$Mn[Fe(CN)$_6$]$_y$$\cdot$$zH_2$O including defects, and the structure is shown in Fig. 2.2(b) [61]. The Fe and Mn ions are bridged by CN$^-$ ligands and construct a three-dimensional lattice, and Rb$^+$ ions are alternately placed on the interstitial sites. There are also some defects where one Fe(CN)$_6$ is replaced by six H$_2$O molecules. Since these defects work as a buffer to relax the strain energy when lattice deformation occurs accompanying the phase transition, the causability of the phase transition can be modified by the stoichiometry of the sample [62].

2.2.3 Temperature induced phase transition with hysteresis

RbMn[Fe(CN)$_6$] exhibits a temperature-induced phase transition[1] with a large hysteresis loop between high-temperature phase (HTP) and low-temperature phase (LTP) as shown in the central graph in Fig. 2.3 [59, 63, 64]. The properties in each phase have been well investigated [59, 63–73]. In HTP, the metal ions are Fe^{3+} [d^5, low spin (LS), $S = 1/2$] and Mn^{2+} [d^5, high spin (HS), $S = 5/2$], where S denotes the total spin angular momentum in an atom. The crystal

---

[1]The PIPT in RbMn[Fe(CN)$_6$] at lower temperatures was shown in Fig. 2.1(a). This phenomenon will be detailed in Sec. 2.2.6.
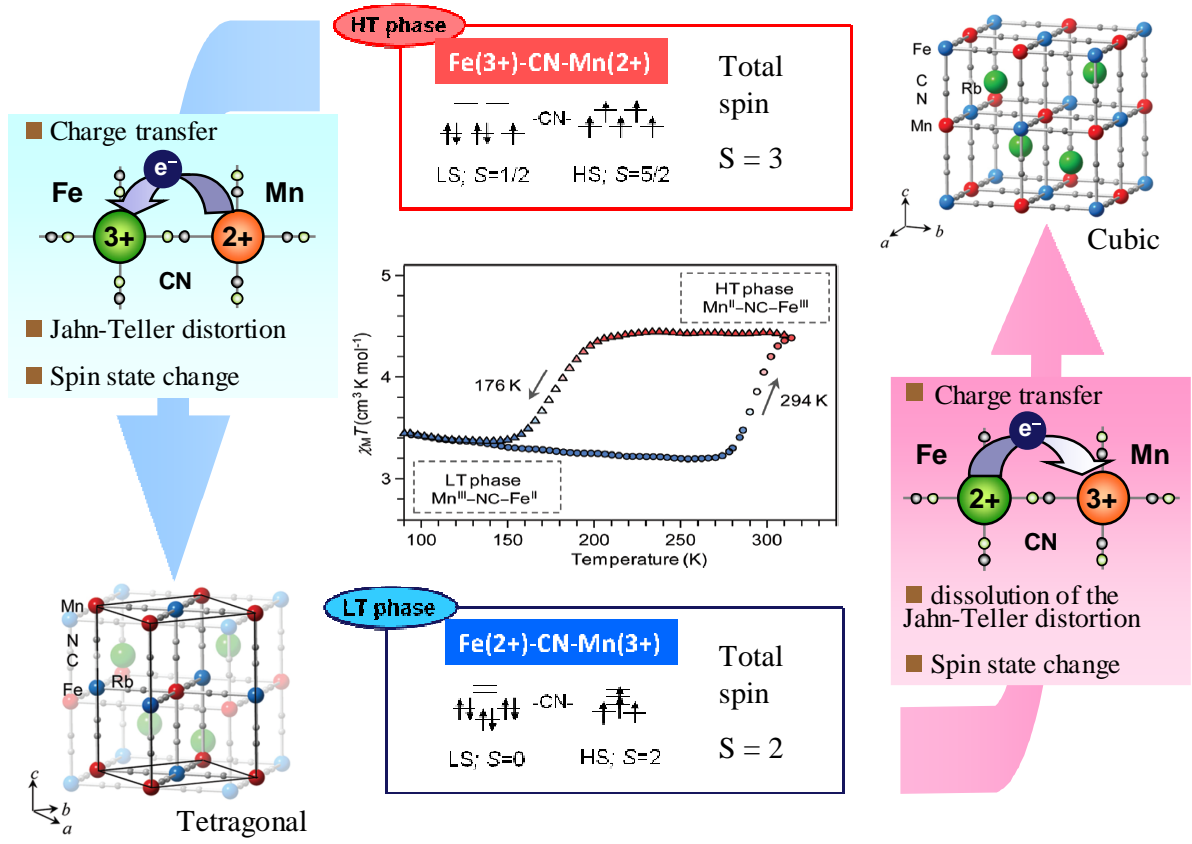
Fig. 2.3: The summary of electronic, lattice, and magnetic changes associated with the temperature induced phase transitions in RbMn[Fe(CN)$_6$] [59,63,64]. The central graph shows the magnetic susceptibility in the thermal phase transition in Rb$_{0.97}$Mn[Fe(CN)$_6$]$_{0.99}$·0.3H$_2$O with the large hysteresis loop, and the surrounding illustrations at the upper right (lower left) shows the properties in HT (LT) phase. The images on the arrows show the changes accompanying the phase transitions. See the text for details.

structure in HTP is cubic ($F\bar{4}3m$). Upon cooling, HTP transfers to LTP at the lower phase transition temperature $T_{1/2\downarrow}$ (= 176 K in this example). This phase transition is accompanied by charge transfer from Mn to Fe ions, and simultaneously induces the structural and magnetic changes as shown in Fig. 2.3; the charge configurations change to Fe^{2+} [d^6, LS, $S = 0$] and Mn^{3+} [d^4, HS, $S = 2$] by charge transfer. Here, note that this is not a spin-crossover phase transition. At the same time, the crystal structure deforms to tetragonal ($I\bar{4}m2$); the lattice is uniaxially distorted at Mn sites due to Jahn-Teller effect (5-% shrink along a- and b-axis). Inversely, by heating the material in LTP, LTP reverts to HTP at the upper phase transition temperature $T_{1/2\uparrow}$ (= 294 K).

The size of the hysteresis loop, defined by $T_{1/2\uparrow}$ - $T_{1/2\downarrow}$, is several tens or over one

15
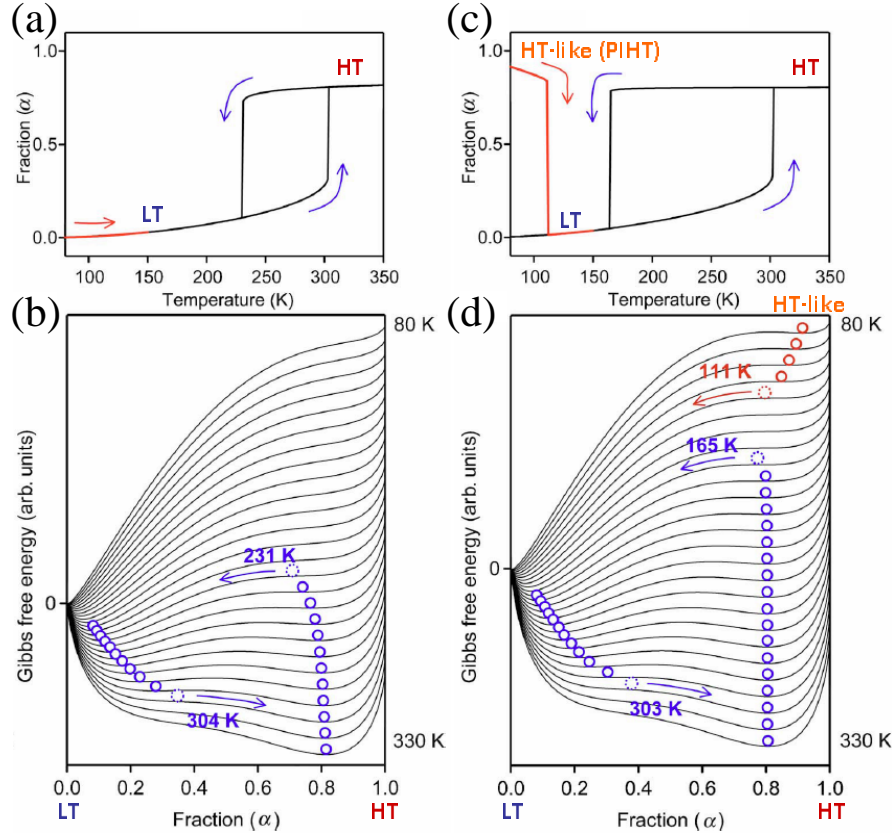
Fig. 2.4: Results of thermodynamical simulations using Slichter-Drickamer model [74, 76]. (a) Thermal hysteresis loop and (b) potential energy curve dependence on temperature in RbMn[Fe(CN)$_6$], and (c), (d) those in Rb$_{0.64}$Mn[Fe(CN)$_6$]$_{0.88}$·1.7H$_2$O. The small circles shown in (b) and (d) correspond to the stable fraction at each temperature.

hundred K in this material. This is exceptionally large among charge-transfer phase transition materials, indicating the existence of strong cooperativity in this phase transition. The size strongly depends on the stoichiometry; with larger amount of H$_2$O, the transition temperature becomes lower and the size of the hysteresis loop becomes larger [62, 74, 75]. This inclination is attributed to the modulation of the elastic interaction in the material by changing the stoichiometry.

The mechanism of this thermal phase transition has been thermodynamically understood by using the Slichter-Drickamer mean-field model (SD model) [74–76]. In the SD model, the interaction between the two phases, HTP and LTP in this case, is taken into account, and the Gibbs free energy G is given as:

$$G = x\Delta H + \gamma x(1-x) + T[R[x\ln x + (1-x)\ln(1-x)] - x\Delta S], \tag{2.1}$$

16

where x is the fraction of HTP (thus, $1 - x$ is that of LTP), ΔH is the transition enthalpy, γ is the temperature-dependent interaction constant ($= \gamma_a + \gamma_b T$), R is the gas constant ($= 8.31$ m^2 kg s^{-2} K^{-1} mol^{-1}), and ΔS is the transition entropy. ΔH and ΔS can be obtained by heat capacity measurements [77], and γ is appropriately set to reproduce the experimental results. Figures 2.4(a) and 2.4(b) show the example of the simulation, (a) thermal hysteresis and (b) potential curve dependences on temperature, in RbMn[Fe(CN)$_6$] ($T_{1/2\uparrow}$ = 304 K, $T_{1/2\downarrow}$ = 231 K). Those in Rb$_{0.64}$Mn[Fe(CN)$_6$]$_{0.88}$·1.7H$_2$O ($T_{1/2\uparrow}$ = 303 K, $T_{1/2\downarrow}$ = 165 K) are also shown in Figs. 2.4(c) and 2.4(d). The used parameters (ΔH, ΔS, γ_a, γ_b) were (1.24 kJ mol^{-1}, 4.54 J K^{-1} mol^{-1}, 20.1 kJ mol^{-1}, 12.0 J K^{-1} mol^{-1}) for RbMn[Fe(CN)$_6$], and (1.68 kJ mol^{-1}, 6.0 J K^{-1} mol^{-1}, 20.5 kJ mol^{-1}, 11.9 J K^{-1} mol^{-1}) for Rb$_{0.64}$Mn[Fe(CN)$_6$]$_{0.88}$·1.7H$_2$O. In these simulations, the hysteresis phenomena were well reproduced by this model. In RbMn[Fe(CN)$_6$] (Fig. 2.4(b)), at 330 K, HTP is the true ground state and is stable. Upon cooling, the shape of the potential curve continuously deforms, and LTP becomes stable under 304 K. However, HTP is still kept due to the energy barrier, reflecting the strong electron-phonon interaction in this material. At 231 K, the energy barrier annihilates, and the HTP transfers to LTP. Inversely upon heating from there, the LTP is kept till 304 K due to the energy barrier, and it transfers to HTP when the sample is further heated. In Rb$_{0.64}$Mn[Fe(CN)$_6$]$_{0.88}$·1.7H$_2$O (Fig. 2.4(d)), besides the hysteresis phenomenon, a hidden HT-like phase was found under 111 K. Such HT-like phase has been found in the samples having moderate quantity of lattice defects, and the existence has been confirmed in photo-irradiated samples [38, 78], which will be discussed in Sec. 2.2.6, or rapidly-cooled samples [79].

2.2.4 Mid-infrared absorption

Next, the optical properties in RbMn[Fe(CN)$_6$] in the mid-infrared frequency region are summarized. This is the basis of the CN vibration spectroscopy, which will be discussed in the next Chapter.

In cyano complexes, the absorption observed in the mid-infrared region (about 2000-2200 cm^{-1}) is ascribed to the stretching vibration modes of the CN groups (Fig. 2.5(a)). From the previous studies, it has been well known that the CN vibration frequency is very sensitive to the valence states of the neighboring metal ions [80–82]. The stretching frequency of free CN$^-$ in aqueous solution is 2080 cm^{-1}. When transition metal ions bond to the each side of CN$^-$, the CN$^-$ works as an electron donor or acceptor to the metal ions, resulting in the modulation of the

(a)

Fe
C
N
Mn
c
a

$C \equiv N$
stretching mode

$\nu = 2000 \sim 2200$ cm^{-1}

(b)
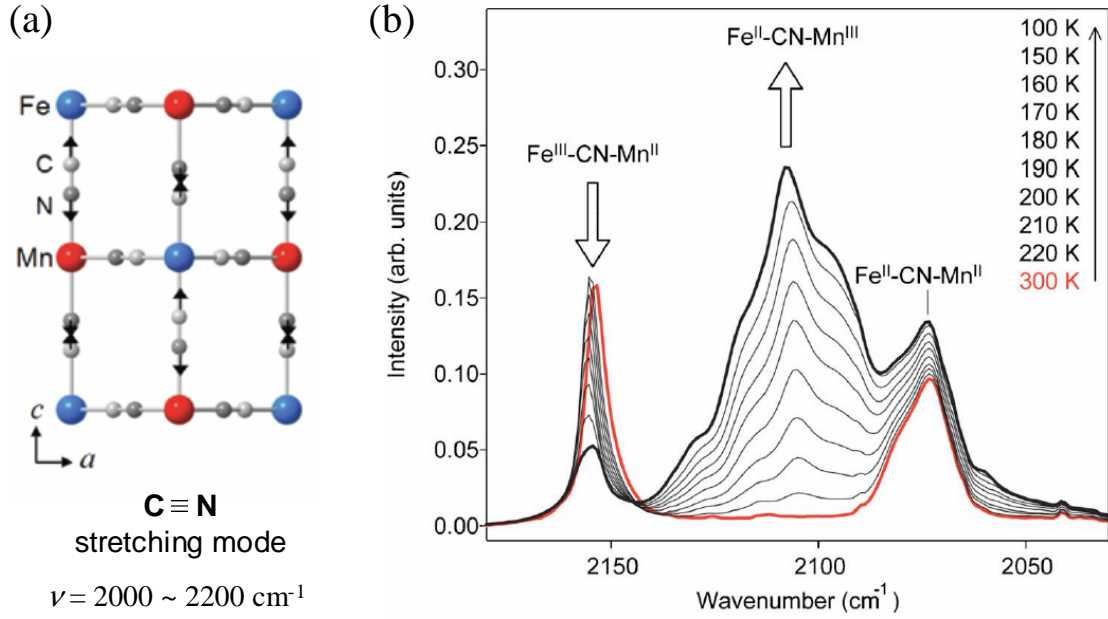
Fig. 2.5: (a) Image of CN stretching vibration mode [59]. (b) The temperature dependence of mid-infrared absorption spectra in $Rb_{0.64}Mn[Fe(CN)_6]_{0.88} \cdot 1.7H_2O$, which is measured by cooling the sample from 300 to 100 K (from HTP to LTP) [74].

CN vibration frequency due to the change of the bonding strength. The CN vibration frequency depends on the valence states of the metal ions; generally, by increasing the oxidation number, the CN frequency becomes larger. The relation between the CN vibration frequency and the valence numbers in hexacyanoferrate have been empirically obtained as summarized in Table 2.1.

Table 2.1: Relation between the frequency of the CN vibration and the valence states in cyano-complexes, where M is transition metal ions [80, 81].

Valence pair	CN vibration frequency (cm^{-1})	Phase in RbMn[Fe(CN)$_6$]
Fe^{2+}-CN-M^{2+}	2060 - 2110	Boundary
Fe^{2+}-CN-M^{3+}	2100 - 2140	LTP
Fe^{3+}-CN-M^{2+}	2145 - 2185	HTP
Fe^{3+}-CN-M^{3+}	2175 - 2210	Boundary

By using this relationship, we can quantify the valence states in RbMn[Fe(CN)$_6$] by performing vibrational spectroscopy, either mid-infrared absorption spectroscopy or Raman scattering spectroscopy. Since the active modes for these two probes are different (When the structure is cubic, T_{1u} is infrared active, and A_{1g} and E_g are Raman active), the observed CN frequencies are slightly different [82].

Figure 2.5(b) shows the mid-infrared absorption spectra observed at various temperatures in the cooling process from 300 to 100 K in Rb$_{0.64}$Mn[Fe(CN)$_6$]$_{0.88}$·1.7H$_2$O. From the empirical law shown in Table 2.1, the sharp peak at 2153 cm^{-1} in the spectrum measured at 300 K is assigned to Fe^{3+}-CN-Mn^{2+}, corresponding to the HTP configuration. The small peak observed at 2073 cm^{-1} is assigned to Fe^{2+}-CN-Mn^{2+} from Table 2.1. This Fe^{2+}-CN-Mn^{2+} component is ascribed to isolated Rb$_2$Mn[Fe(CN)$_6$] microcrystallines, which are slightly included in the synthesis to compensate the charge balance. This assignment is supported by the experimental fact that the component at 2073 cm^{-1} does not change before and after the phase transition. Upon cooling, the HTP peak at 2153 cm^{-1} decreases around the lower side of the hysteresis loop, and the large broad peak centered at 2108 cm^{-1} arises in turn. This absorption band is assigned to Fe^{2+}-CN-Mn^{3+} from the empirical relation, which corresponds to the configuration of LTP. The broadening of this peak is ascribed to the randomness of the environment; random lattice strains of various magnitudes in various directions due to the Jahn-Teller distortion disturb the lattice symmetry, resulting in the lift of their degeneracy and split (or broadening) of the CN vibration peak.

2.2.5   Ultraviolet-visible absorption

Next, the ultraviolet-visible absorption in RbMn[Fe(CN)$_6$] is discussed. In the previous reports [83, 84], the spectra of the dielectric constant ϵ in RbMn[Fe(CN)$_6$] were obtained from the spectroscopic ellipsometry. The spectra of its imaginary part ϵ'' in HTP and LTP are shown in Figs. 2.6(a) and 2.6(b), which roughly correspond to the ultraviolet-visible absorption in RbMn[Fe(CN)$_6$]. The ϵ'' spectrum in HTP (Fig. 2.6(a)) was decomposed into two Lorentzian components at 220 and 405 nm. Both components were assigned to the LMCT (Ligand to Metal Charge Transfer) band, originated from charge transfer from CN group to Fe^{3+} ion. The ϵ'' spectrum in LTP (Fig. 2.6(b)) was decomposed into four Lorentzian components. The component at 210 nm was assigned to the MLCT band originated from charge transfer from Fe^{2+} to CN, that at 457 nm was assigned to the IT (inter-valence transfer) band originated from
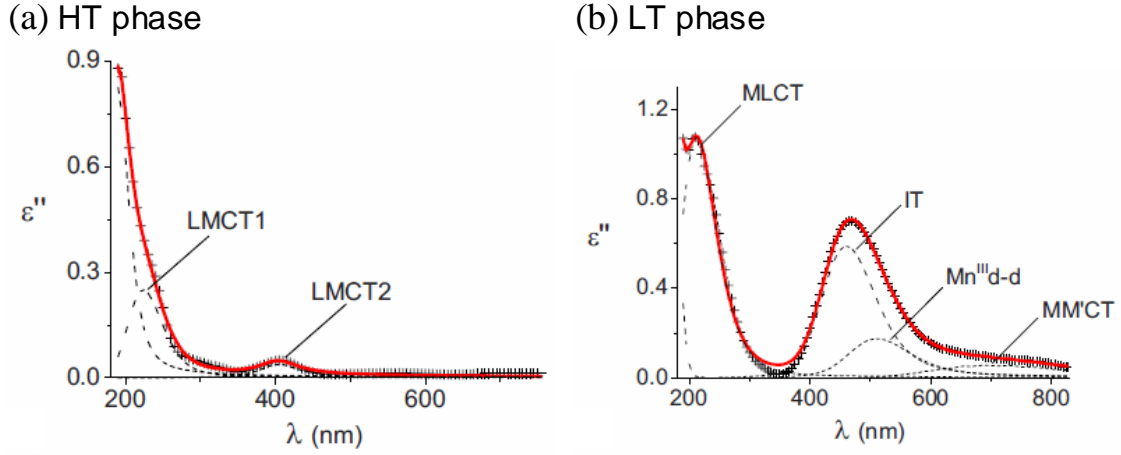
Fig. 2.6: Imaginary parts of dielectric constant ϵ'' of RbMn[Fe(CN)$_6$] in (a) HTP and (b) LTP. The Lorentzian components (dashed line) were obtained by the fitting analysis (red solid line) from the result of the spectroscopic ellipsometry investigation (cross marker) [83, 84].

the direct charge transfer from Fe^{2+} to Mn^{3+}, and those at 508 and 685 nm were assigned to *d-d* transitions in Mn^{3+} ion, respectively. The details of the ultraviolet-visible absorption bands are summarized in Table. 2.2.

Table 2.2: Ultraviolet-visible absorption bands in RbMn[Fe(CN)$_6$] [83, 84].

Phase	Wavelength (nm)	Band	Transition configuration	
HTP	220	LMCT1	CN$^- \to$ Fe^{3+}	$^2T_{2g} \to\,^2 T_{1u}$
	405	LMCT2	CN$^- \to$ Fe^{3+}	$^2T_{2g} \to\,^2 T_{1u}$
LTP	210	MLCT	Fe$^{2+} \to$ CN$^-$	$^1A_{1g} \to\,^1 T_{1u}^{(1)},\,^1 T_{1u}^{(2)}$
	457	IT	Fe$^{2+} \to$ Mn^{3+}	CN$_{2p_x(y)} \to$ Mn$_{3d_{x^2-y^2}}$
	508	*d-d*	Mn^{3+}	$^5B_{1g} \to\,^5 B_{2g},\,^5 E_g$
	685	*d-d*	Mn^{3+}	$^5B_{1g} \to\,^5 A_{1g}$

20
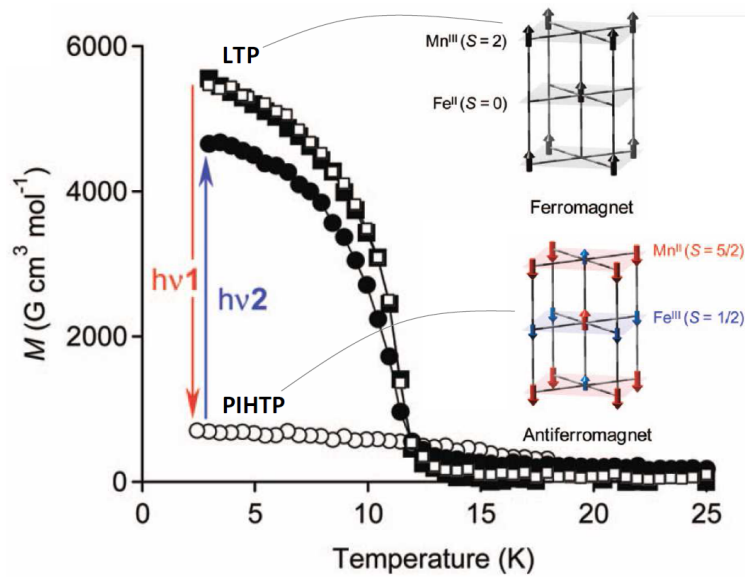
Fig. 2.7: The magnetization *M* changes in the reversible PIPT between LTP (ferromagnetic phase) and PIHTP (antiferromagnetic phase) in RbMn[Fe(CN)$_6$] [38]. This is the same graph introduced in Fig. 2.1(a).
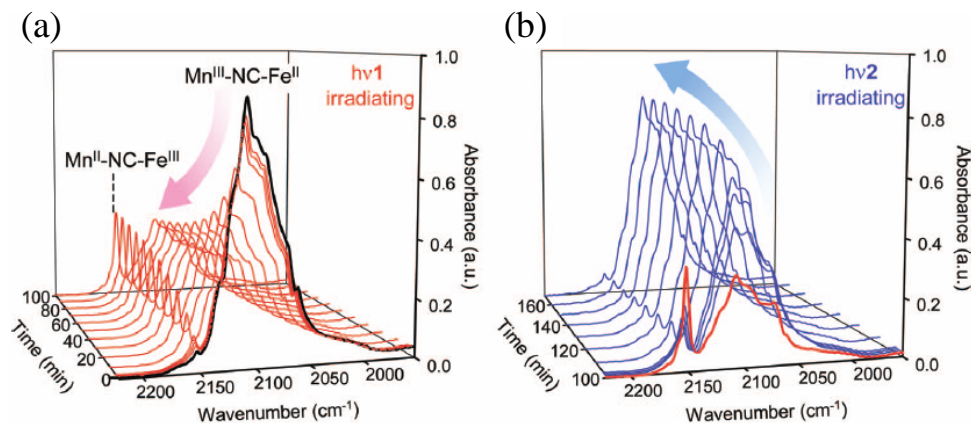
Fig. 2.8: The evolution of the mid-infrared spectra in the PIPT, (a) from LTP to PIHTP and (b) from PIHTP to LTP [38].

2.2.6 PIPTs in RbMn[Fe(CN)$_6$]

Reversible ferro-antiferro magnetic PIPT at low temperatures

The phase transition in RbMn[Fe(CN)$_6$] can be caused not only by temperature change but also by optical excitation. As shown in Fig. 2.7, RbMn[Fe(CN)$_6$] exhibits a reversible magnetic PIPT at low temperatures by light irradiation at two different wavelengths. LTP has the

21
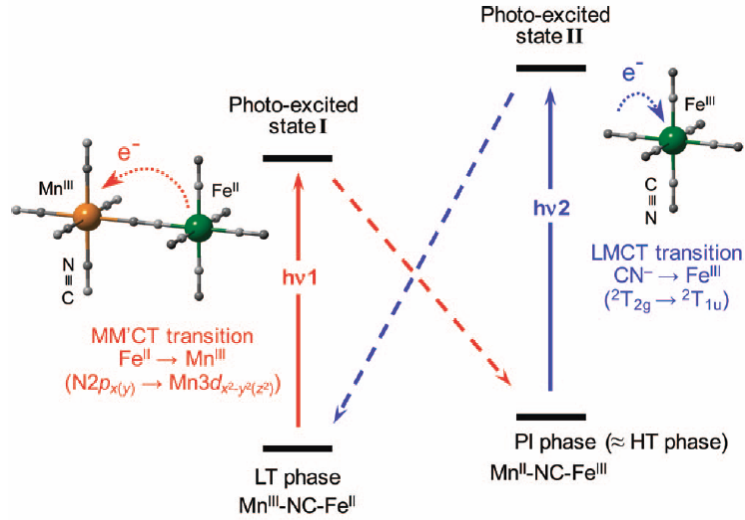
Fig. 2.9: The schematic mechanism of the reversible PIPT in RbMn[Fe(CN)$_6$] [38].

ferromagnetic order (Fig. 2.7) under the Curie temperature of 12 K due to the superexchange interaction between Mn^{3+} ions [85]. When the ferromagnetic LTP is irradiated by green light at 532 nm (hv1), the magnetization M dramatically drops down, and a new photoinduced phase arises. Upon this phase transition, the mid-infrared spectrum changes as shown in Fig. 2.8(a); the broad peak corresponding to Fe^{2+}-CN-M^{3+} (LTP) decreases, and the peak corresponding to Fe^{3+}-CN-M^{2+} arises. This charge configuration is the same as that in HTP, thus, we call the photogenerated state at low temperature as PIHTP (Photo-Induced High Temperature Phase). PIHTP corresponds to the HT-like phase found from the calculation shown in Fig. 2.4(d). PIHTP has the nearly cubic crystal structure with a slight tetragonal distortion, and antiferromagnetic ordering (Fig. 2.7) under the Néel temperature of 11.5 K. Inversely, when PIHTP is irradiated by blue light at 410 nm (hv2), PIHTP is reversed to LTP as confirmed in Figs. 2.7 and 2.8(b). This reversible ferro-antiferro magnetic PIPT can be induced repetitively.

The mechanism of this reversible PIPT has been interpreted as shown in Fig 2.9. When LTP is irradiated by light at 532 nm (hv1), the IT band shown in Fig. 2.6(b) is excited, and electrons at Fe^{2+} are transferred to Mn^{3+}. Then, LTP is excited to a photo-excited state I, and it relaxes to PIHTP. The PIHTP is trapped due to the energy barrier. In the inverse process, when PIHTP is irradiated by blue light at 410 nm (hv2), the LMCT2 band shown in Fig. 2.6(a) is excited, inducing charge transfer from CN^- to Fe^{3+} (photo-excited state II). Subsequently, charges are supplied from Mn^{2+} to CN, and the state relaxes to LTP.

The details of the relaxation dynamics, such as relaxation time scales or the interactions
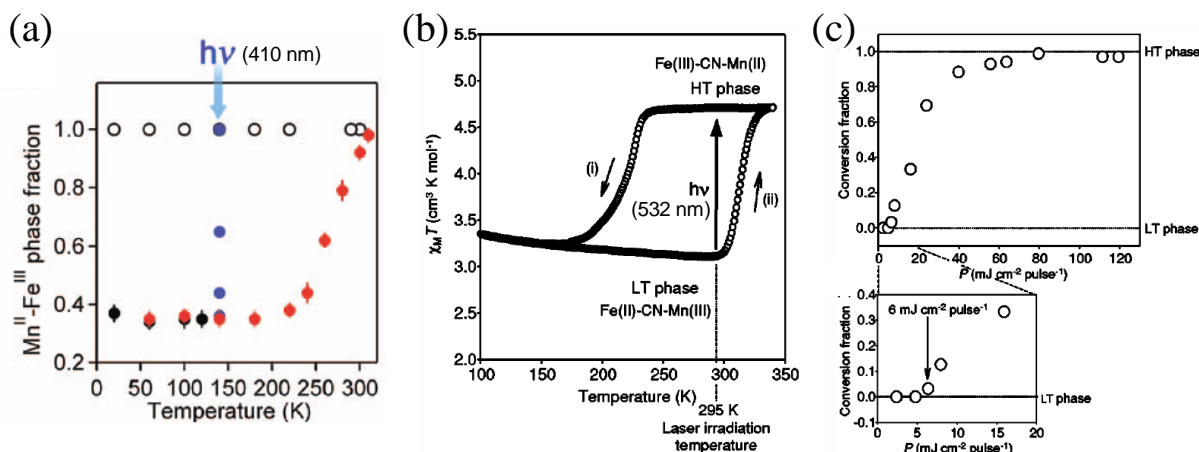
Fig. 2.10: (a) The HTP fraction change in $Rb_{0.43}Mn[Fe(CN)_6]_{0.81}\cdot3H_2O$ by irradiating with 410-nm CW light at 140 K [86]. (b) The thermal hysteresis loop of the magnetic susceptibility showing the excitation conditions, and (c) the conversion fraction from LTP to HTP in $Rb_{0.98}Mn_{1.01}[Fe(CN)_6]\cdot0.2H_2O$ by irradiating with one 532-nm ns pulse [87]. The excitation power dependence shows clear threshold at 6 mJ cm^{-2} pulse^{-1}.

between electronic and structural changes etc., have been still unclear. Therefore, further time-resolved studies are needed to understand the whole PIPT mechanism.

PIPT near thermal hysteresis loop

The phase transition between HTP and LTP can be caused by optical excitation at temperatures around the thermal hysteresis loop. For instance, as shown in Fig. 2.10(a), HTP in $Rb_{0.43}Mn[Fe(CN)_6]_{0.81}\cdot3H_2O$ is transferred to LTP by irradiating with 410-nm CW light at 140 K [86]. In addition, as shown in Figs. 2.10(b) and 2.10(c), LTP in $Rb_{0.98}Mn_{1.01}[Fe(CN)_6]\cdot0.2H_2O$ is transferred to HTP by irradiating with one shot of 532-nm ns laser pulse [87]. In Fig. 2.10(c), the excitation power dependence of the conversion fraction exhibits clear threshold at 6 mJ cm^{-2} pulse^{-1}. Here, the quantum efficiency (the number of the photoconverted sites per one incident photon) was evaluated to be above one (2~5), indicating this process is indeed PIPT involving strong cooperativity. These PIPTs are triggered by optical stimulation of the charge transfer bands shown in Fig. 2.6, which is the same mechanism as in the case of the reversible PIPT at low temperatures mentioned above.

23

2.3 Previous experimental studies on PIPT dynamics in cyano-complexes

Several studies have been previously reported on PIPT dynamics in cyano-complexes. Here, three representative researches are briefly introduced. The first two examples are about ultrafast spectroscopy of cyano-complexes, and the last one is about the Raman scattering measurement in minutes time scale.

2.3.1 *Example 1*: Ultrafast CN vibration spectroscopy in RbMn[Fe(CN)$_6$] at room temperature

In RbMn[Fe(CN)$_6$], HTP-to-PILTP (Photoinduced LTP) transition at room temperature was studied by ultrafast time-resolved CN vibration spectroscopy [88][2]. Herein, bleach of HTP (Fe^{3+}-CN-Mn^{2+}), and increases of LTP (Fe^{2+}-CN-Mn^{3+}) and boundary (Fe^{2+}-CN-Mn^{2+}) were observed in the ps time region. This experiment has been the first demonstration of time-resolved CN vibration spectroscopy in cyano-complexes.

2.3.2 *Example 2*: Ultrafast absorption spectroscopy in Fe cyanides

For other examples, in M-Fe (M = Mn, Fe, Co) typed cyano-complexes, their charge transfer dynamics has been investigated by time-resolved absorption spectroscopy by Kamioka *et al.* [92, 93]. In these articles, they reported the following. In Co-Fe cyanide, the relaxation dynamics after optical pumping could be decomposed into fast and slow components with 20~30 ps and ~2 ns, respectively. The fast component was assigned to the creation of self-trapped charge-transferred Co-Fe pairs with lattice relaxation, and the slow decay component was to the relaxation to the initial state. The decay time elongation was also observed by increasing the excitation density, which was ascribed to the stabilization of the excited domain due to formation of clusters. Also in Mn-Fe and Fe-Fe cyanide, similar relaxation phenomena with two decay components were observed.

---

[2]This study was performed in our research group, however, the author was not directly engaged in this experiment.
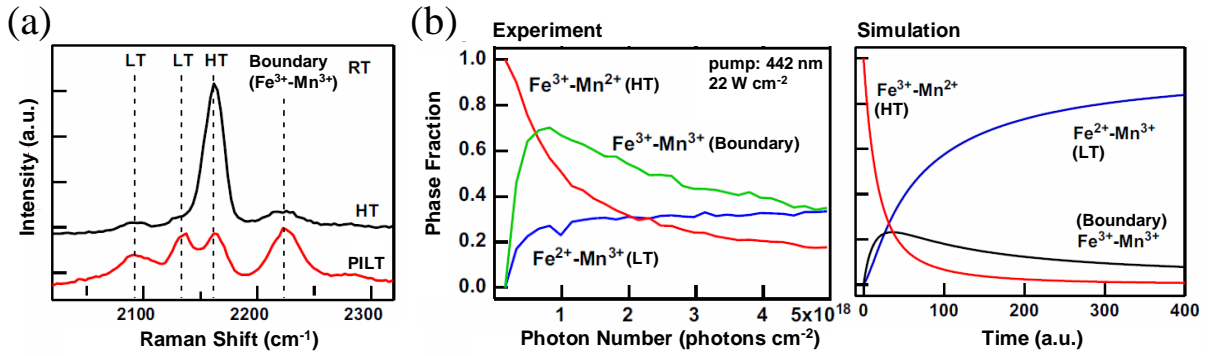
Fig. 2.11: (a) Raman spectra of HTP and PILTP in $Rb_{0.58}Mn[Fe(CN)_6]_{0.78} \cdot 2.7H_2O$ [91]. Under irradiation with 442-nm CW probing laser the spectrum in HTP changes to that in PILTP. (b) Experimental results (left) and simulation (right) of the time evolution of the phase fractions (HTP, LTP, and boundary) [91].

2.3.3 *Example 3*: Raman scattering spectroscopy in $RbMn[Fe(CN)_6]$ probing PIPT in minutes time scale

$RbMn[Fe(CN)_6]$ has also been investigated by Raman scattering spectroscopy [82, 89–91][3]. CN vibrations can be probed by Raman scattering as well as by mid-infrared absorption spectroscopy. The former has two advantages. One is that the Fe^{3+}-CN-Mn^{3+} boundary configuration, which is hard to observe in mid-infrared spectroscopy, can be explicitly detected due to the resonance Raman effect [89] as shown in Fig. 2.11(a). The other is the easiness of the spectral decomposition because the observed peaks are narrower than those observed in mid-infrared spectroscopy. The narrowness of these peaks is probably ascribed to the difference of the selection rules between these two measurements.

As shown in the left graph in Fig. 2.11(b), the dynamics of the HTP-to-PILTP transition in minutes time scale was observed by Raman scattering spectroscopy. The persistent phase transition gradually proceeds; HTP decreases and in turn LTP and boundary arises. It should be noted that the fraction of boundary turns to decrease on the time evolution, indicating the aggregation of the excited LTP domains. The temporal behavior of this boundary component was qualitatively simulated by the calculation using a mean-filed model as shown in the right graph in Fig. 2.11(b). This has been a good demonstration of the direct probe of the domain growth dynamics by using the boundary sensitive CN vibration spectroscopy.

On the other hand, in ultrafast time scale, it was hard to observe the dynamics by

---

[3]These studies were also performed in our research group, and the author was partially engaged in this study.

time-resolved Raman scattering spectroscopy because of the weak Raman signal. Mid-infrared spectroscopy seems to be preferable for observing the transient dynamics because of the higher signal to noise ratio. The probe method should be selected depending on the objective.

2.4   Objective of this research

In researches on $RbMn[Fe(CN)_6]$, its static properties have been well investigated as mentioned above. However, the excited states or the relaxation dynamics are not so clear especially at low temperatures. Thus, time-resolved studies are required to observe the microscopic changes and to understand the underlying PIPT mechanism.

In our study, the first objective is to understand the dynamics of the reversible PIPTs at low temperatures in $RbMn[Fe(CN)_6]$ by using time-resolved CN vibration spectroscopy (Chapter 3). As described in Sec. 2.2.4, CN stretching vibration modes are very sensitive to the valence states of the adjacent metal ions. Hence, by measuring the mid-infrared absorption, it is expected that we can quantify not only LTP (Fe^{2+}-CN-Mn^{3+}) and PIHTP (Fe^{3+}-CN-Mn^{2+}) but also the domain boundary configurations (Fe^{2+}-CN-Mn^{2+} and Fe^{3+}-CN-Mn^{3+}). By directly monitoring their valence states, the charge transfer dynamics will be well characterized, which is significant, because the phase transition is triggered by charge transfer. In addition, by monitoring the phase itself (LTP, PIHTP) and the domain boundary configurations simultaneously, this experiment will give some insight for nucleation process of the PIPT.

Our second objective is to understand the magnetic dynamics associated with the charge-transfer PIPT in $RbMn[Fe(CN)_6]$ (Chapter 4). As shown in Fig. 2.3, electronic, structural, and magnetic changes occur simultaneously in the phase transition in $RbMn[Fe(CN)_6]$. Therefore, in order to understand the microscopic changes, their dynamics should be separated. It is expected that the magnetic dynamics can be separately observed by time-resolved Faraday rotation spectroscopy. By comparing the results with those from time-resolved absorption spectroscopy, the electronic, structural, and magnetic dynamics will be characterized.

Chapter 3

Time-resolved CN Vibration Spectroscopy

In this chapter, we investigated the dynamics of the reversible PIPTs at low temperatures between LTP and PIHTP in RbMn[Fe(CN)$_6$][1]. The visible-pump mid-infrared-probe transient absorption spectroscopy (time-resolved CN vibration spectroscopy) was applied as the measurement method. Since CN stretching vibration modes are very sensitive to the valence states of the adjacent metal ions, CN vibration spectroscopy can quantify not only LTP (Fe^{2+}-CN-Mn^{3+}) and PIHTP (Fe^{3+}-CN-Mn^{2+}) but also the phase boundary configurations (Fe^{2+}-CN-Mn^{2+} and Fe^{3+}-CN-Mn^{3+}). By monitoring the phase itself (LTP, PIHTP) and the phase boundary configurations simultaneously, the charge transfer dynamics including the nucleation process in the PIPT is discussed.

Below, the advantages and the previous researches of CN vibration spectroscopy in cyano-complexes are firstly described. Next, the experimental configurations, the results, and discussions are described. Finally, the conclusion, the PIPT scenario constructed from the results, is summarized.

3.1 CN vibration spectroscopy

In the mid-infrared frequency region, there is a wide variety of specific molecular vibrations. Thus, mid-infrared absorption spectroscopy has often been used to assign the molecules and to characterize their properties.

As explained in the last Chapter (Secs. 2.2.4, 2.3.1, and 2.3.3), the CN stretching

---

[1]The main results discussed in this chapter were summarized in our research papers, Ref. [95, 96].
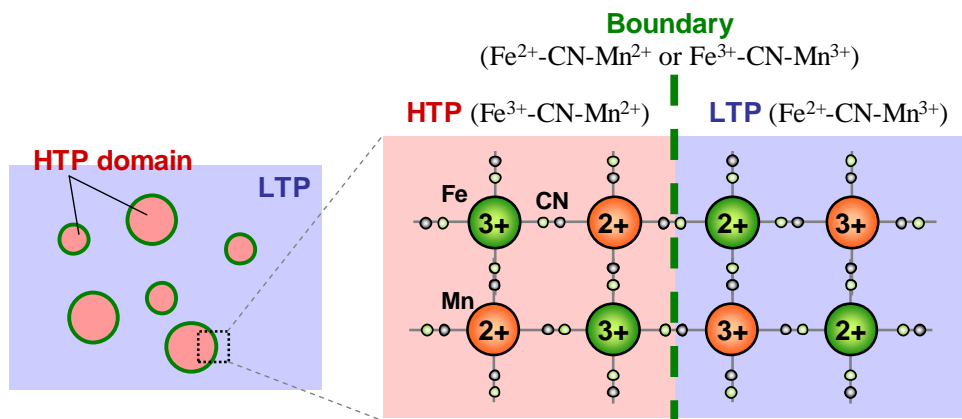
Fig. 3.1: Illustrations showing the probable valence configurations in RbMn[Fe(CN)$_6$]. The left panel shows the HTP domains created in LTP background, and the enlarged view is shown in the right panel.

vibration modes in cyano-complexes are located in 2000-2200 cm^{-1} (about 4.5-5.0 μm in wavelength), and their frequencies are very sensitive to the valence states of the adjacent metal ions. The relations between the frequencies and the valence states have been empirically obtained in hexacyanoferrate (Table. 2.1) [80, 81]; the frequencies for Fe^{2+}-CN-M^{2+}, Fe^{2+}-CN-M^{3+}, Fe^{3+}-CN-M^{2+}, and Fe^{3+}-CN-M^{3+} (M = transition metal) appear in the ranges of 2065-2110, 2090-2140, 2146-2185, and 2180-2200 cm^{-1}, respectively. Hence, we can utilize the vibration spectroscopy, mid-infrared or Raman spectroscopy, as an indicator of the charge-transfer-typed phase transition. Moreover, we can quantify the distribution not only of LTP (Fe^{2+}-CN-Mn^{3+}) and PIHTP[2] (Fe^{3+}-CN-Mn^{2+}) but also of boundary configurations (Fe^{2+}-CN-Mn^{2+} and Fe^{3+}-CN-Mn^{3+}), which exist on the boundary of LTP and PIHTP domains (Fig. 3.1). This indicates that the CN vibration spectroscopy is phase boundary sensitive in studying cyano-complexes, giving us powerful advantages for characterizing their PIPT dynamics including the formation of the embryonic nuclei.
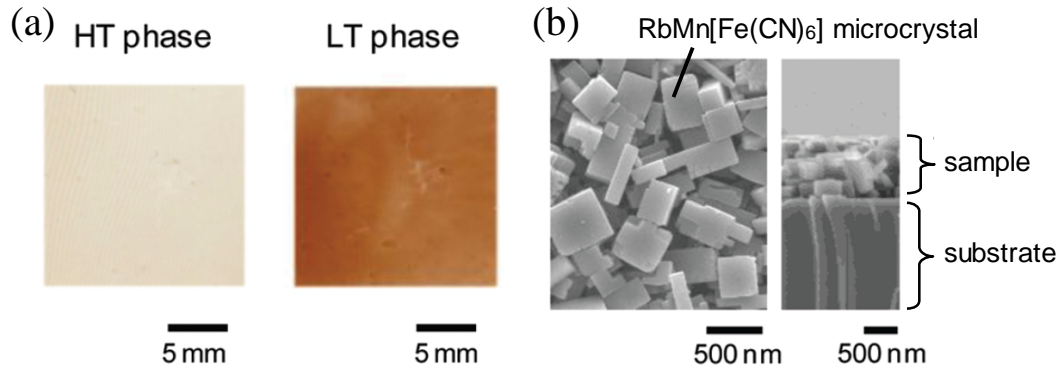
Fig. 3.2: (a) Examples of photographs of a RbMn[Fe(CN)$_6$] film sample (Rb$_{0.97}$Mn[Fe(CN)$_6$]$_{0.99}$·0.3H$_2$O) in HTP (left) and LTP (right) [59]. (b) SEM images of the surface (left) and the cross-section (right) of the film sample [59].

3.2 Experiment

3.2.1 Sample preparation

To date, several types of RbMn[Fe(CN)$_6$] samples can be synthesized: (i) a powder-formed sample [38], (ii) a film where microcrystals are formed in nanoporous Nafion film [94], or (iii) a film composed of microcrystals coated on a substrate [59]. In this study, (iii) the microcrystal-coated film was used as the sample[3]. The film was prepared by spin-coat-like method, whose synthetic procedure was detailed in Ref. [59]. The microcrystals we used had a composition of Rb$_{0.94}$Mn[Fe(CN)$_6$]$_{0.98}$·1.3H$_2$O, and was formed on a sapphire substrate (size: 12×12 mm^2, thickness: 0.4 mm, c-plane). As shown in Fig. 3.2(a), the color of a RbMn[Fe(CN)$_6$] film is light cream color in HTP and is dark brown in LTP. As shown in the SEM images in Fig. 3.2(b), the microcrystals are piled on the substrate. The size of the microcrystals was several hundreds of nanometers, and the thickness was estimated to be about 1 μm. The phase transition temperatures between HTP and LTP in the cooling and warming processes were T$_{1/2↓}$ = 145 K and T$_{1/2↑}$ = 290 K, respectively.

---

[2]PIHTP is the anti-ferromagnetic phase with the same valence states as the HTP arising at low temperatures, which was defined in Sec. 2.2.6.

[3]All the RbMn[Fe(CN)$_6$] film samples measured in this thesis were synthesized by our collaborators H. Tokoro and S. Ohkoshi at the Univ. of Tokyo.
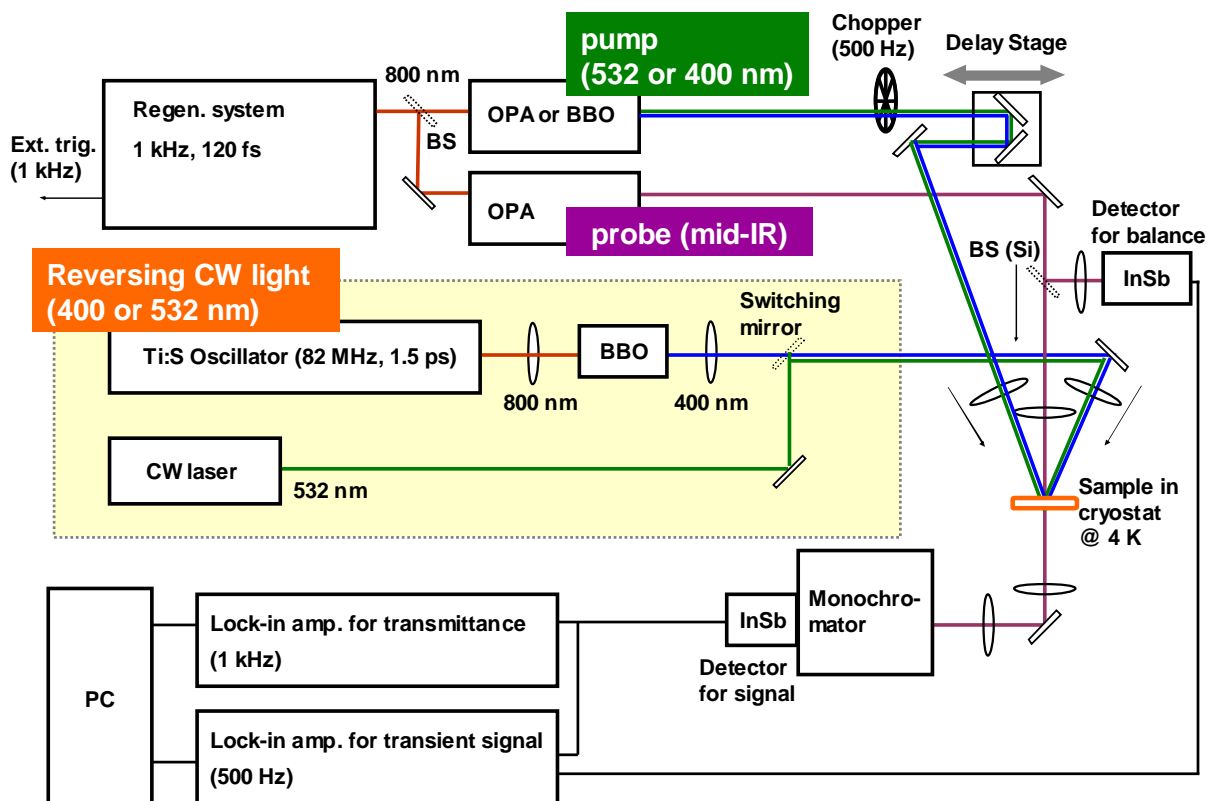
Fig. 3.3: The experimental setup of the time-resolved CN vibration spectroscopy.

3.2.2 Visible-pump mid-infrared-probe transient absorption spectroscopy

We performed visible-pump mid-infrared probe transient absorption spectroscopy (time-resolved CN vibration spectroscopy) to investigate the picosecond charge transfer dynamics in the reversible PIPT, LTP to PIHTP and PIHTP to LTP, in $Rb_{0.94}Mn[Fe(CN)_6]_{0.98}\cdot 1.3H_2O$.

The schematic of the experimental setup is shown in Fig. 3.3. The sample was mounted on a cryostat equipped with CaF_2 windows, and all the measurements were carried out at 4 K. We employed a 1 kHz repetitive regenerative amplifier system (Spectra-Physics, Spitfire) producing 120 fs pulses at 800 nm seeded by a mode-locked Ti:sapphire laser (Spectra-Physics, TSUNAMI 3160C), and the output was divided into pump and probe beams. The pump beam was mechanically chopped at 500 Hz for lock-in detection. In investigating LTP to PIHTP conversion, pump pulses at a wavelength of 532 nm, which resonantly excite the IT band
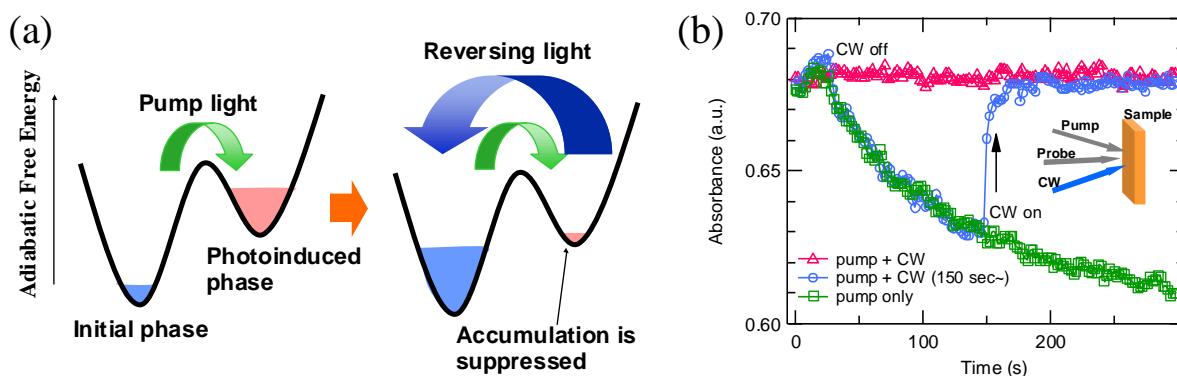
Fig. 3.4: (a) Concept of the suppression of the photoinduced phase accumulation with the reversing light. (b) The evolution of the absorption at 2110 cm^{-1} (LTP peak) by 532-nm pump light irradiation [96]. The decrease of the absorption indicates the accumulation of PIHTP. It is found that the gradual accumulation was suppressed only during the reversing 400-nm CW light was irradiated.

(see Fig. 2.6) inducing the charge transfer from Fe^{2+} to Mn^{3+}, were generated by taking sum frequency of the fundamental beam and the idler beam from an optical parametric amplifier (OPA) (Light Conversion, TOPAS-C) with a nonlinear optical crystal, β-BaB_2O_4 (BBO). On the other hand, to investigate the reverse process, PIHTP to LTP conversion, we excited the LMCT band (see Fig. 2.6) inducing charge transfer from Mn^{3+} to Fe^{2+}. We generated second harmonics of the fundamental wave at 400 nm with a BBO crystal and employed it as pump pulses. The probe pulses in the mid-infrared region monitoring CN stretching vibration modes were generated by taking the difference frequency of signal and idler beams from another OPA system (Light Conversion, TOPAS-C). The probe light transmitted through the sample was monochromatized by a grating monochromator (Nikon, G250) and was detected by an InSb photoconductive detector. The wavenumber resolution in our measurement condition is about 2 cm^{-1}. Two lock-in amplifiers which were synchronized to 1 kHz and 500 Hz, respectively, were used to record the intensity of the transmitted light and the transient absorption change simultaneously. The time resolution of this measurement system is approximately 260 fs, which was estimated by measuring cross-correlation of the pump and probe pulses.

31

3.2.3 Realization of pump-probe measurement in persistent phase transition

In this experiment, the photogenerated phase was persistent after light irradiation. Thus, it is normally difficult to apply pump-probe spectroscopy, because the photogenerated state is accumulated via the repetitive pumping processes. However, we enabled the measurement by introducing an idea, that the initial state for every pump pulse is recovered by simultaneously irradiating with another light inducing the reverse process [95, 96]. The concept is schematically shown in Fig. 3.4(a).

As shown in Fig. 3.3, when we irradiated the sample with the pump beam at a wavelength of 532 nm, a quasi-continuous wave (CW) light at a wavelength of 400 nm was simultaneously directed to the sample. The quasi-CW light was obtained by generating second harmonics of another mode-locked Ti:sapphire oscillator (Spectra-Physics, TSUNAMI 3950C) producing 1.5 ps pulses at a wavelength of 800 nm. Since the repetition rate of 82 MHz is sufficiently high, we regarded it as a quasi-CW light source. On the other hand, when we pumped the sample with the beam at a wavelength of 400 nm, a CW light at a wavelength of 532 nm was simultaneously directed to the sample. The CW light was obtained from a frequency-doubled yttrium aluminum garnet laser pumped by a diode laser.

Figure 3.4(b) shows the evolution of the absorption at 2110 cm^{-1} (LTP peak) by irradiating with 532-nm pump light [96]. The decrease of the absorption indicates the accumulation of PIHTP. It is found that the gradual accumulation was suppressed when 400-nm light is switched on. If the reversing light was not irradiated, the photoinduced phase became dominant within a few minutes. Although the accumulation of the photoinduced phase was not completely removed, in this way we could keep the photoinduced phases at low concentrations for a sufficiently long time required for pump-probe measurement. The transient signal was not affected by the CW light itself, because its fluence in the time scale observed in our experiment (several hundreds of picoseconds) was negligibly small compared to that of the pump light.
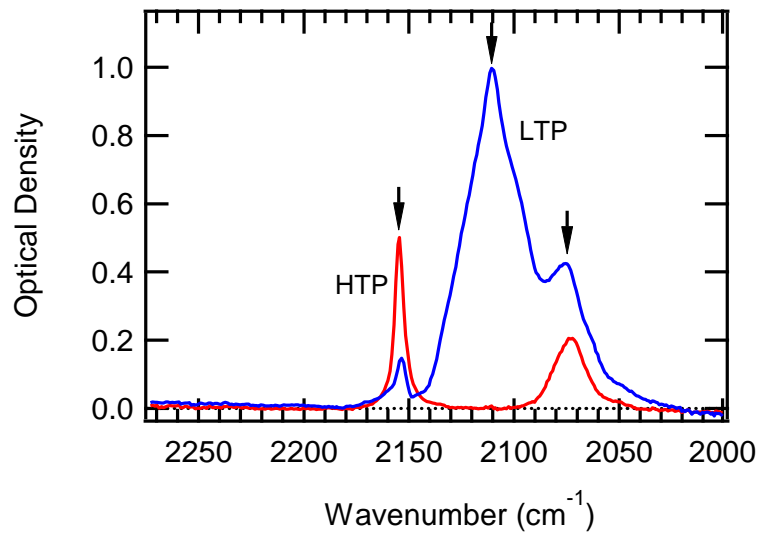
Fig. 3.5: The mid-infrared absorption spectra in the RbMn[Fe(CN)$_6$] film. HTP at room temperature (red) and LTP at 4 K (blue).

3.3 Results and discussions

3.3.1 Static mid-infrared absorption spectrum in RbMn[Fe(CN)$_6$] film

First, we measured the mid-infrared absorption in the sample. In Fig. 3.5, we showed the absorption spectrum of HTP at room temperature (RT) and that of LTP prepared by cooling the sample to 4 K. The assignments of these peaks were based on the empirically obtained relations between CN stretching vibration frequency and the valence states of the adjacent metal ions, which was discussed in Sec. 2.2.4. From this empirical law, the sharp peak at 2154 cm^{-1} shown in Fig. 3.5 was assigned to Fe^{3+}-CN-Mn^{2+} (HTP). The relatively sharp peak at 2074 cm^{-1} in the spectrum of HTP can be assigned to Fe^{2+}-CN-Mn^{2+} of Rb$_2$Mn[Fe(CN)$_6$], which was slightly included as isolated microcrystallines from the synthesis. Upon cooling, the peak at 2154 cm^{-1} corresponding to HTP gradually decreased around the lower side of the hysteresis loop at 145 K, and the large broad peak at 2110 cm^{-1} arose. This peak was assigned to Fe^{2+}-CN-Mn^{3+} (LTP) from the empirical relation. These spectra showed very good correspondence to those obtained in the previous research (Fig. 2.5(b)) [74].

3.3.2 PIPT dynamics from LTP to PIHTP

Next, the transient responses in the PIPT were observed at 4 K. First, we observed the transition dynamics from LTP to PIHTP by the transient mid-infrared absorption measurement with pump pulses at a wavelength of 532 nm (0.4 W cm^{-2}). Quasi-CW light at a wavelength of 400 nm (2 W cm^{-2}) simultaneously irradiates the sample to keep the concentration of the PIHTP at a low level during the measurement.

Assignment of the absorption spectrum under light irradiation

Figure 3.6(a) shows the absorption spectrum at 4 K[4] during the measurement. The experimental data are expressed as black circles. It is found that the spectrum has some differences from the original LTP spectrum in Fig. 3.5. The main changes are the decrease of the peak at 2105 cm^{-1} corresponding to LTP and the increase of the magnitude around 2080 cm^{-1}.

In order to interpret the spectrum in Fig. 3.6(a), we decomposed it into the four components by a least-squares fitting method. The spectrum was well reproduced with the four components. Here we assumed Gaussian functions for the spectral components, because the broadenings of these peaks were ascribed to the randomness of the environment, which is caused by random lattice strains of various magnitudes in various directions. From the comparison with the spectrum in Fig. 3.5, the small peak at 2157 cm^{-1} is ascribed to HTP. The relatively sharp peak at 2074 cm^{-1} is assigned to Fe^{2+}-CN-Mn^{2+} valence configuration of Rb$_2$Mn[Fe(CN)$_6$] as mentioned in the previous section. Since this component is assigned to isolated Rb$_2$Mn[Fe(CN)$_6$] particles and will not contribute to the concerned phase transition process, we call it "extrinsic Fe^{2+}-Mn^{2+}" and neglect it in the discussions hereafter.

Assignment of the broad peak at around 2079 cm^{-1} is not straightforward, because this component is hardly observed in HTP at RT or in fresh LTP generated by cooling as shown in Fig. 3.5. It gradually arises when 532 nm pump pulses and 400 nm CW laser light, which induce the inverse phase transitions, simultaneously irradiate the sample. Since the center wavelength of this peak is located in the typical frequency range corresponding to Fe^{2+}-CN-Mn^{2+} (2065-2110 cm^{-1}), it can be assigned to this valence configuration. Although the low-frequency tail of this band exceeds the typical range, it is also ascribed to

---

[4]The measurement temperature, 4 K, is actually that of the cryostat, and that of the sample itself is expected to be heated to some extent by the incident light. However, the effect of this static temperature increase was neglected in this experiment, because the reversible PIPTs, the main target of this research, was successfully observed indeed.

Fe^{2+}-CN-Mn^{2+}, because only the low valence pair can appear in the low-frequency region. We call this component the "boundary" in the following discussions, because it appears only on the boundary between LTP and PIHTP as mentioned in Sec. 3.1.

It is interpreted that such a large number of the boundary configurations arise because the PIHTP domains are fragmented into small clusters while repeating the innumerable phase switching processes. Once this broad peak due to the boundary is created, it hardly decreases even if we stop the pump pulses keeping irradiation with 400 nm light. We speculate that this fact is explained by the blocking effect whose mechanism has been understood as follows [82]. When $[Fe(CN)_6]^{4-}$ surrounded by six Mn^{2+} ions are congregated to constitute Fe^{2+}-CN-Mn^{2+} clusters, the metal-ion pairs in these clusters become unable to contribute to the charge transfer. Therefore, the number of Fe^{2+}-CN-Mn^{2+} valence pairs does not decrease under irradiation of either 532 nm or 400 nm light. The considerable broadening of this peak is probably caused by random local strain fields which are created on the interface between domains having different lattice constants.

Transient responses in the PIPT from LTP to PIHTP

Figure 3.6(b) shows the transient absorption spectra at various delay times, which were obtained by scanning the monochromator at fixed delay times. Here, the transmitted light intensity was recorded with the lock-in amplifier synchronized to 1 kHz, and the transient change of the intensity was simultaneously recorded with another lock-in amplifier synchronized to 500 Hz. We calculated the changes of the optical density (O.D.) with the outputs obtained from these two lock-in amplifiers. We regarded the spiky structures found in Fig. 3.6(b) as noise and neglected them in the analysis performed later.

Major features found in these spectra are as follows. First, decreasing of the absorption around 2110 cm^{-1} due to LTP was found. Increasing of the absorption was also found in the lower wavenumber range corresponding to Fe^{2+}-CN-Mn^{2+} (boundary). These two main features were as we expected. However, some complicated behaviors could also be found in the spectra. At 0 ps, a plateau appeared in the higher wavenumber range, and a bump structure was found at around 2140 cm^{-1}. By comparing the spectra at 0 ps and 1 ps, we could find a slight blue shift of the dip around 2110 cm^{-1} and a gradual increase around 2090 cm^{-1}.

The complexity was also reflected in the time evolution of normalized transient absorption shown in Fig. 3.7. These curves were recorded by scanning delay times with the
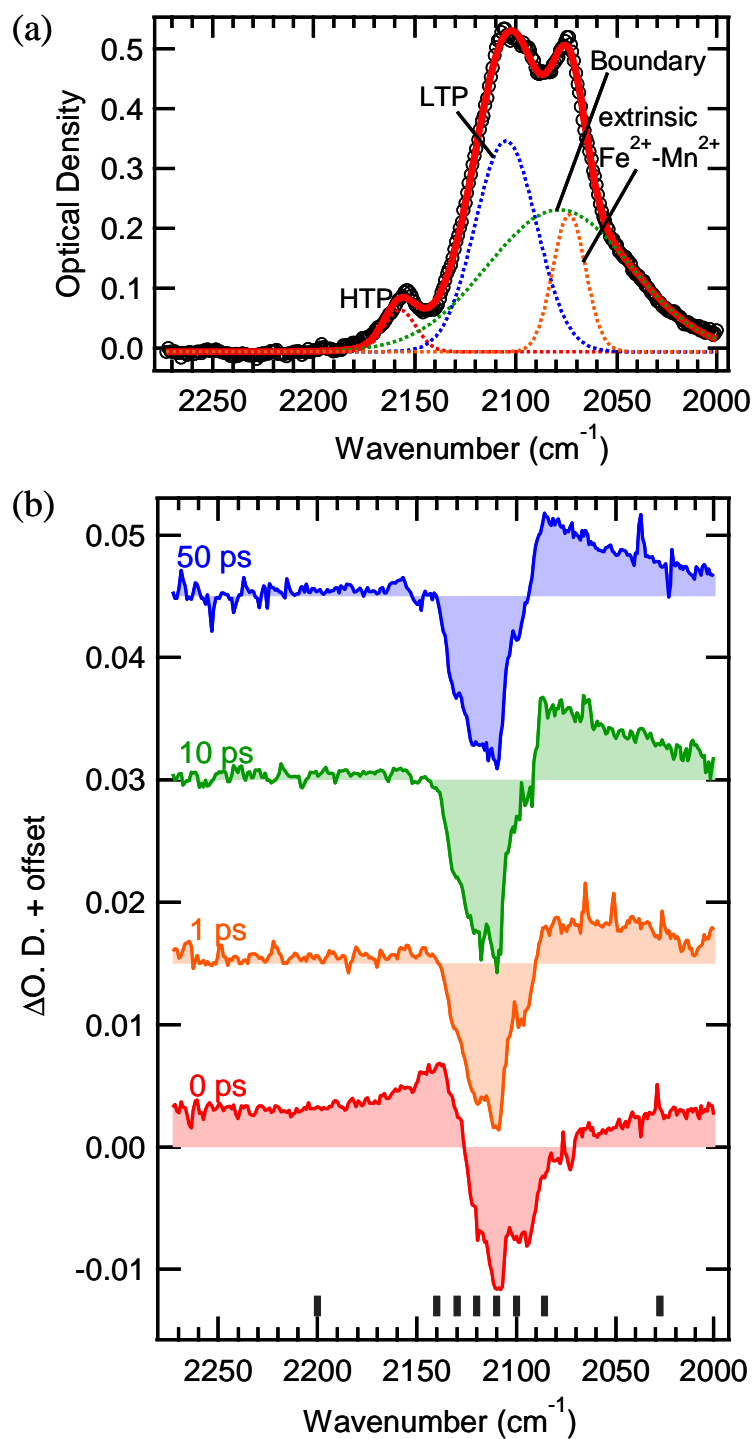
Fig. 3.6: (a) Static absorption spectrum of LTP during the experiment observing the dynamics of the phase transition from LTP to PIHTP (black circle) and the fitting result (red solid line). The decomposed four components, HTP (red), LTP (blue), boundary (green), and extrinsic Fe^{2+}-Mn^{2+} (orange), are also exhibited as dotted lines. (b) Transient absorption spectra at 0, 1, 10, and 50 ps showing the dynamics of the phase transition from LTP to PIHTP. The excitation density of pump pulses and CW light are 0.4 W cm^{-2} and 2 W cm^{-2}, respectively.

36
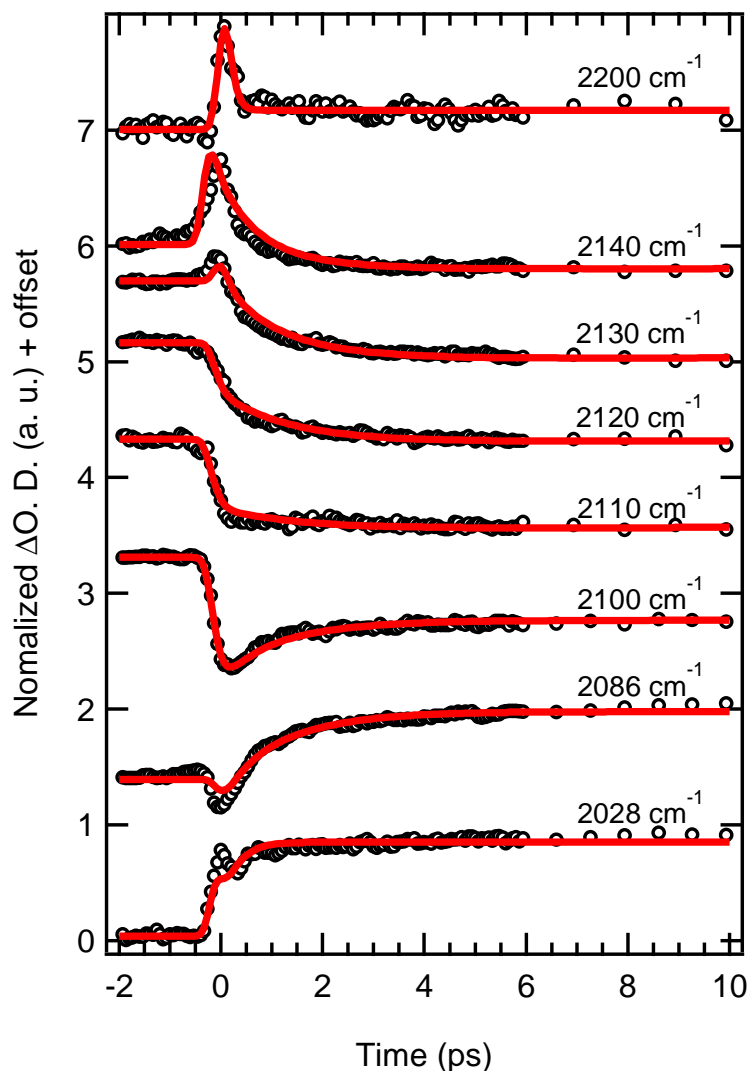
Fig. 3.7: Time evolution curves of normalized transient absorption showing the dynamics of the phase transition from LTP to PIHTP (black circle). The indicated wavenumbers correspond to the black rectangles, where the time evolutions were measured, shown at the bottom of Fig. 3.6(b). The phenomenological fitting results are inserted as red solid lines.

monochromator fixed. These time evolution curves change critically depending on the probe wavenumber. From this fact, these curves seem to be intermingled by several contributions with different rising and relaxation times. To understand the complicated phenomenon, we tried to decompose the spectra in Fig. 3.6(b).
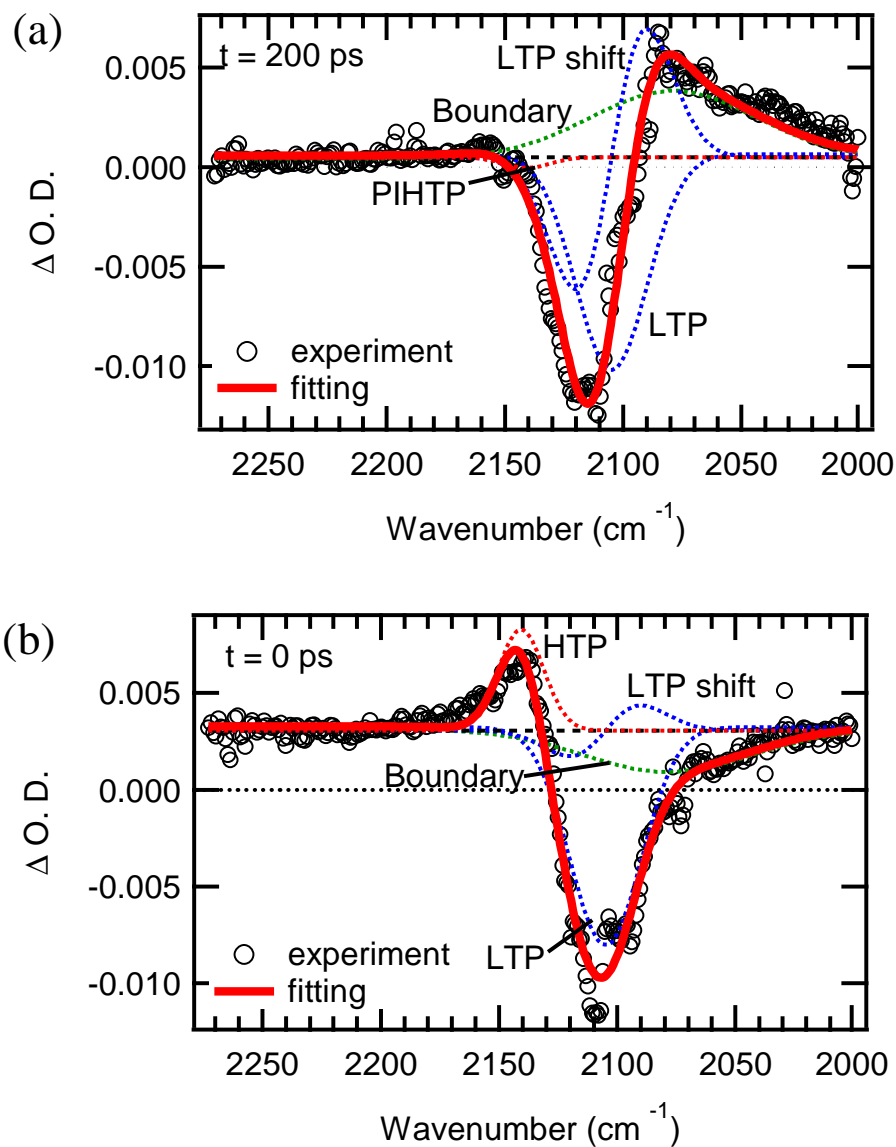
Fig. 3.8: Transient absorption spectra at (a) 200 ps and (b) 0 ps (black circle). The fitting results are inserted as red solid lines, and the decomposed components are exhibited as dotted lines.

Fitting analysis of the transient absorption spectra

To begin with, the transient absorption spectrum at $t = 200$ ps was analyzed as an example of the data obtained in the late delay times. Figure 3.8(a) shows the result of the fitting analysis. We tried to reproduce the spectrum by superposing the following three components[5] defined in

---

[5]Actually, we additionally assumed two components, a Gaussian component corresponding to PIHTP at 2141 cm^{-1} and a flat offset component. However, the contributions of these two components are found to be negligibly
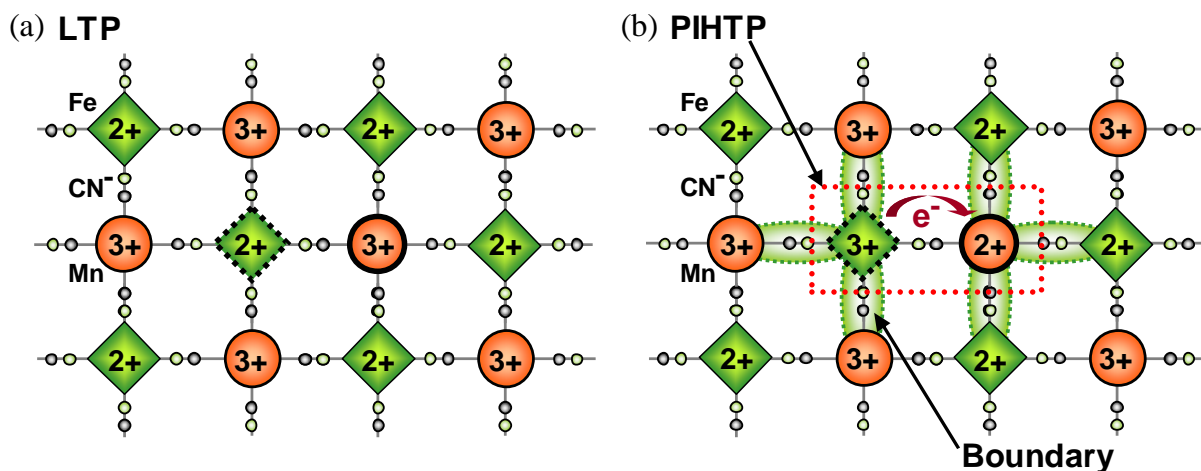
Fig. 3.9: The cross-section of the lattice of $RbMn[Fe(CN)_6]$, where the interstitial Rb^+ ions are omitted for simplification. (a) The distribution of the metal ion's valence numbers in LTP (Fe^{2+}-CN-Mn^{3+}) and (b) that in the situation after one electron is transferred from Fe^{2+} to Mn^{3+}. The charge-transferred site enclosed by the red dotted rectangle is converted to the PIHTP (Fe^{3+}-CN-Mn^{2+}) configuration. At the same time, the CN^- sites masked by green dotted ovals (totally 10 sites from the three-dimensional viewpoint) surrounding the charge-transferred site become the boundary configurations (Fe^{2+}-CN-Mn^{2+} or Fe^{3+}-CN-Mn^{3+}).

Fig. 3.6(a), i.e., the LTP peak at 2105 cm^{-1}, the boundary peak at 2074 cm^{-1}, and the red shift of the LTP peak. Here, the shift of the LTP peak is expressed as the differentiated wave form of the LTP absorption peak. By performing this fitting procedure, the experimental spectrum could be successfully reproduced as expressed by the red solid curve in Fig. 3.8(a)[6]. The large decrease of LTP and the increase of boundary are interpreted as the reduction of LTP and the production of boundary, respectively, resulting from the charge transfer from Fe^{2+} to Mn^{3+}. The third component, the peak shift of the LTP peak, is ascribed to local strains induced by a lattice mismatch, which arises when the cubic-like PIHTP domain is optically generated in the tetragonal background of LTP.

Here, it is interesting to note that the increase of the PIHTP peak is virtually zero against our natural expectation. This can be understood from the following two facts. First, the oscillator strength of the PIHTP peak is much smaller than that of LTP. This indication was given from the absorption spectra shown in Fig. 3.5, because the area of the HTP peak was far smaller

___

small at 200 ps. These components are necessary at $t = 0$ as discussed in the next analysis.

[6]Here, a small splitting around 2115 cm^{-1} is found in the experimental spectrum at 200 ps. Since the crystal structure in LTP is tetragonal, the LTP component may split into several components. However, since all the components observed in this wavenumber range (2090-2140 cm^{-1}) can be assigned to the LTP, we neglected this splitting and treated these peaks as one LTP component in the analysis.

than that of the LTP peak. Second, the number of newly created PIHTPs accompanying a photoinduced charge transfer is far smaller than those of bleached LTPs and generated boundary configurations. As explained in Fig. 3.9, when a charge transfer occurs at one site in LTPs (Fe^{2+}-CN-Mn^{3+}), only one PIHTP (Fe^{3+}-CN-Mn^{2+}) is newly created at this site, while LTP is bleached at the surrounding 11 sites and boundary configurations (Fe^{2+}-CN-Mn^{2+} and Fe^{3+}-CN-Mn^{3+}) are generated at 10 sites (from the three-dimensional viewpoint). In this way, the absence of the PIHTP peak's change can be justified.

Moreover, as for the domain size and its form, the following can be indicated from the spectra in Fig. 3.8(a). In these spectra, the peak area of the two transient changes, the decrease of the LTP peak and the increase of the boundary peak, are roughly of the same order. From this fact, it is suggested that the numbers of the disappeared LTPs and the created boundary configurations are also of the same order, provided the oscillator strengths of these peaks are not so different. In this PIPT, when photons are absorbed at Fe^{2+}-CN-Mn^{3+} pairs, many initial nuclei are expected to be created in the LTP background at random. Then, the averaged domain size would become smaller and/or the domain would have a complicated forms like fjord-like structures. In such cases, the amount of the created boundary configuration becomes larger as in the present study. Such tendency has also been supported from some theoretical studies [1,97]. This point is a clear difference from the case of thermal phase transition where the continuous domain growth is the main process of the phase transition. Hence, our result observing the large amount of boundary creation is expected to correspond to the transient nucleation process in PIPT.

Transient responses of each component

We applied this decomposition procedure also to the transient absorption spectrum at 0 ps. The fitting results are shown in Fig. 3.8(b). The significant difference from the spectrum at 200 ps is the additional positive offset component observed in an extremely wide wavenumber range. This component is reflected in the time evolution curve at 2200 cm^{-1} in Fig. 3.7 as a sharp spike at 0 ps. It is found that both its rising and relaxing times are as fast as the time resolution of the measurement system. In addition, we found that the intensity of this component is rather sensitive to the measurement conditions, such as slight change of the beam's position. From these facts, we speculated that the offset component may be due to some nonlinear optical response such as Kerr-lens effect which is not directly related to the phase transition. Therefore,
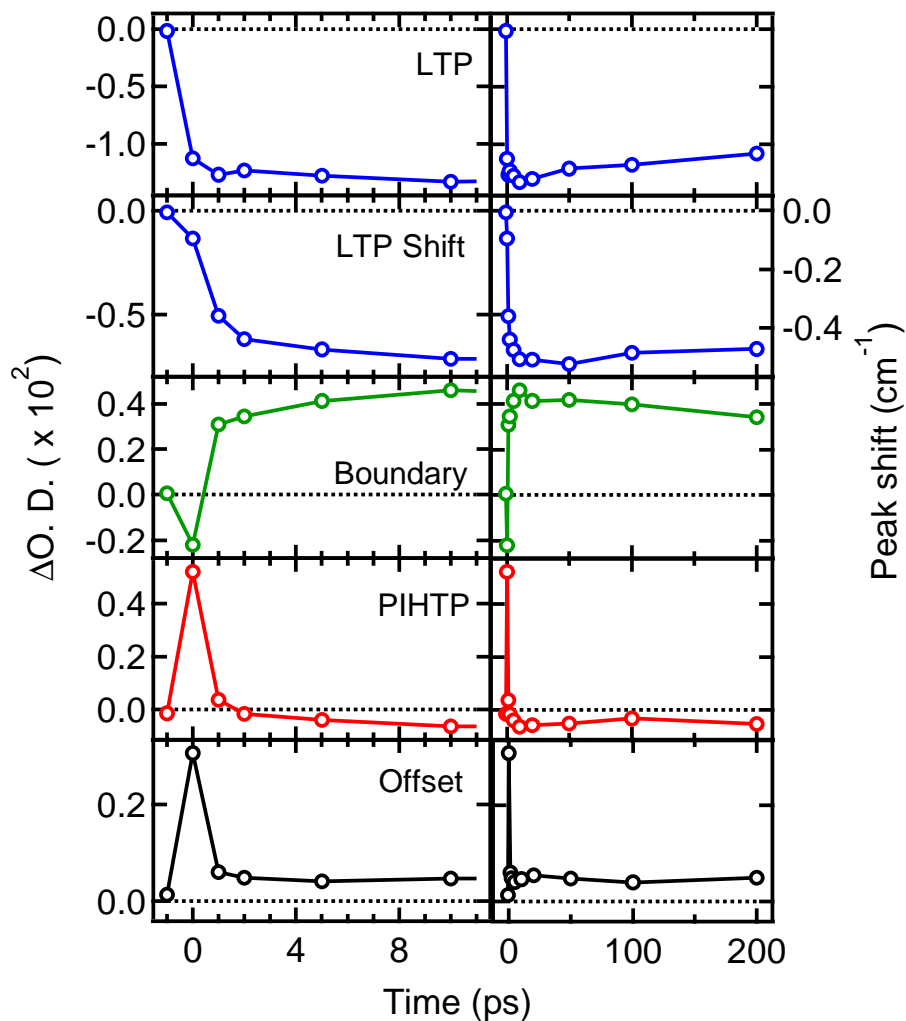
Fig. 3.10: Time evolution curves of the decomposed five components, LTP, the shift of LTP, boundary, PIHTP, and the offset component. The horizontal dotted lines represent zero. The OD values for LTP, boundary, and PIHTP were obtained at the peaks of the Gaussian functions. That for the LTP shift was evaluated at the extremum of the differentiated wave form (2120.5 cm^{-1}). For the plot of LTP shift, the corresponding peak shift is displayed on the right axis.

we treated it as just a flat component, and the following analyses are discussed without this component.

Removing the flat component from the spectrum, the dominant component is the large decrease of the LTP peak at 2105 cm^{-1}. This spectrum at 0 ps seems to have a double-peaked structure around 2105 cm^{-1}, which might correspond to the structure of the LTP peak shown in Fig. 3.6(a). This structure in Fig. 3.6(a) is not clear because the splitting is smaller than the broadening, and several peaks may be overlapping. Here, from the same reason as in the case

of Fig. 3.8(a), we neglected this splitting and regarded it as one LTP component in the analysis. In the spectrum in Fig. 3.8(b), relatively small decreases of the boundary peak and the LTP peak shift component are also observed. In addition, it is necessary to assume a positive peak at 2141 cm^{-1} to reproduce the bump structure in the experimental spectrum. This component is tentatively assigned to instantaneous PIHTP generation, although the center wavenumber is slightly lower than that obtained in the static absorption spectrum. This component may correspond to some intermediate state, which is similar to HTP but has somewhat different lattice relaxation.

We decomposed the transient absorption spectra at other delay times from - 1 to 200 ps in the same way. Figure 3.10 summarizes the time evolution of the decomposed five components, i.e., the LTP peak at 2105 cm^{-1}, the shift of LTP peak, the boundary peak at 2079 cm^{-1}, the HTP peak at 2141 cm^{-1}, and the flat offset component. From this analysis, the overall behavior of time evolutions of each component was revealed. The LTP component is instantaneously bleached after the light excitation. The LTP peak shows a redshift of about 0.52 cm^{-1} taking about 1 ps. The boundary component has an irregular behavior in which the absorption decreases at 0 ps and it turns to an increase after 1 ps. These three changes decay slowly and survive longer than 100 ps. PIHTP and the offset component rise steeply at the time origin and rapidly relax to the initial state within 1 ps.

Table 3.1: Function forms and time constants of the components used in the fitting procedure shown in Fig. 3.7. TR denotes the time resolution of 0.26 ps.

i	Component	$I_i(t)$	τ_r (ps) (rising time)	τ_d (ps) (decay time)
1	LTP	$1 - \exp(-t/\tau_r)$	0.16	$\gg 100$
2	LTP shift	$1 - \exp(-t/\tau_r)$	1.32	$\gg 100$
3	Boundary	$\exp(-t/\tau_d)$	$<$ TR	0.27
		$1 - \exp(-t/\tau_r)$	0.31	$\gg 100$
4	PIHTP	$\exp(-t/\tau_d)$	$<$ TR	0.59
5	Offset	$\exp(-t/\tau_d)$	$<$ TR	0.10 ($<$ TR)

In order to analyze the time evolution at the early stage (<10 ps) of the transition more accurately, we tried to reproduce all the experimental time evolution curves shown in Fig. 3.7 based on these five components. The fitting function is defined as:

$$g(t, \omega) = \int f_{inst}(\tau) \sum_i I_i(t - \tau) C_i(\omega) \, d\tau \quad (i = 1, \ 2... \ 5), \quad (3.1)$$

where $C_i(\omega)$ is the spectral shape of each component deduced by the decomposition procedure mentioned above, $I_i(t)$ denotes the time evolution curve of each component, and $f_{inst}(\tau)$ is the instrumental Gaussian function. The subscripts i indicate the spectrum components. As for the spectral shapes, $C_i(\omega)$, the components of LTP, boundary, and PIHTP ($i = 1, 3$, and 4) are Gaussian functions. The component of the LTP shift ($i = 2$) is the derivative of a Gaussian function, and the offset component ($i = 5$) is a constant independent of wavenumbers. The function forms of $I_i(t)$ are defined as shown in Table 3.1 to reproduce the shape of the time evolution curves in Fig. 3.7. In order to describe the irregular shape of the boundary component ($i = 3$), we assumed a sum of two components: One component instantaneously decreases and rapidly relaxes. The other component slowly rises and stays constant. The fitting results are shown in Fig. 3.7 as red solid curves, and the obtained time constants are summarized in Table 3.1. The fitting curves in Fig. 3.7 have some deviations from the experimental curves (black circles) around 0 ps. This discrepancy is ascribed to the nonlinear optical response which strongly depends on the measurement conditions as mentioned above. Except for this ambiguity near the time origin, the detailed structures of the experimental curves are well reproduced over the measured wavenumber range. Especially, the 1-ps delay lied between LTP and LTP shift components accurately reproduce the slight difference between the waveforms of 2110 and 2120 cm^{-1}. Since the calculated curves are in good agreement with the experimental data, this phenomenological analysis can be justified.

Scenario of the PIPT from LTP to PIHTP

From these analyses, the following PIPT scenario is derived. The main relaxation processes are schematically shown in Fig. 3.11(a)-(c). First, the 532-nm light excites the IT band and induces immediate charge transfer from Fe^{2+} to Mn^{3+}, which is evidenced by a sharp decrease of the LTP band. At the same time, PIHTP is produced at the charge-transferred sites. However, against our natural expectation, almost all the created PIHTP disappears within 1 ps. Furthermore, the boundary configuration temporarily decreases just after excitation at the same

43

(a) **PIHTP** **Boundary**

Just after excitation (< 260 fs: time resolution)

• Optical excitation of IT band

• Charge transfer: $Fe^{2+} \rightarrow Mn^{3+}$

• Creation of PIHTP and Boundary

(In boundary-rich area, the number of boundary decreases associated with the charge transfer)

(b)

~1 ps

• Lattice deformation
(dissolution of Jahn-Teller distortion)

(In boundary-rich area, temporal PIHTP creation and boundary bleaching reverse)

(c)

$\gg$ several 100 ps

• Reverse to initial LTP

Fig. 3.11: Schematic of the main processes in the PIPT dynamics from LTP to PIHTP.

time. Tentatively, the spectral behaviors corresponding to the temporal PIHTP creation and the boundary bleaching are ascribed to the nonlinear effect observed around 0 ps[7]. After this transient response within one picosecond, the boundary configuration increases in accordance with the decrease of LTP configuration till 10 ps and starts to decrease slowly after that. The

---

[7]If these temporal behaviors are not due to the nonlinear effect, the observation may be understood with the following idea. When a charge is transferred from Fe^{2+} to Mn^{3+}, Fe^{2+}-CN-Mn^{2+} pairs around this Fe^{2+} disappear and new Fe^{2+}-CN-Mn^{2+} pairs appear around the Mn^{2+}. If the boundary components, i.e., Fe^{2+}-CN-Mn^{2+} and Fe^{3+}-CN-Mn^{3+} pairs, prevail in the initial state, the number of newly created Fe^{2+}-CN-Mn^{2+} pairs could be smaller than the number of those disappeared, and the net change of boundary component can be negative. In actuality, the number of boundary in the initial state was rather large as expected from the absorption spectrum shown in Fig. 3.6(a). If the transient charge-transferred state created in such a "boundary-rich" area is unstable, the momentary decrease of the boundary and the increase of the PIHTP can be understood.

existence of a slowly rising component indicates that the phase change has some delay from the charge transfer transition itself. The relatively large response of the boundary component indicates that a large number of boundary configurations are created at the charge-transferred site surrounded by the background of the LTP as depicted in Fig. 3.9(b). Lastly, the LTP peak shift has a rising time of approximately 1 ps, which is clearly slower than the charge-transfer process mentioned above. It can be attributed to a delayed local deformation caused by the dissolution of Jahn-Teller distortion. The time constant 1 ps may correspond to the time required for the lattice to deform. All these photoinduced species except for the short-lived PIHTP survive longer than 100 ps.

3.3.3   PIPT dynamics from PIHTP to LTP

Second, in order to observe the dynamics of the PIHTP-to-LTP transition, we performed transient mid-infrared absorption measurement with pump pulses at a wavelength of 400 nm (0.25 W cm^{-2}). The PIHTP was prepared by irradiating the sample in LTP with the CW light at a wavelength of 532 nm (1 W cm^{-2}) at 4 K. Irradiation at this wavelength keeps the LTP at low concentration during the pump-probe measurement.

Assignment of the absorption spectrum under light irradiation

The absorption spectrum of PIHTP during the measurement is shown in Fig. 3.12(a). The spectrum could be reproduced by the four Gaussian functions in the same way mentioned in Sec. 3.3.2. The peaks at 2155, 2099, 2072, and 2074 cm^{-1} were assigned to PIHTP, LTP, boundary, and extrinsic Fe^{2+}-Mn^{2+} of isolated $Rb_2Mn[Fe(CN)_6]$ microcrystals, respectively. The spectral shape is different from that of HTP in Fig. 3.5 in the point that the HTP peak is smaller and the boundary peak appears. The production of a large amount of the boundary component indicates that the blocking effect occurs and that the size of the photocreated domain is small as in the case of LTP-to-PIHTP transition discussed in the previous section. Although a small fraction of the LTP component remains, the transient variation observed here mainly reflects the phase transition from PIHTP to LTP, because the number of PIHTPs is sufficiently larger than that of LTPs. The slight differences of the center wavenumbers of the peaks between PIHTP in Fig. 3.12(a) and LTP in Fig. 3.6(a) are attributed to the strain caused by transformations of the majority crystal structures.
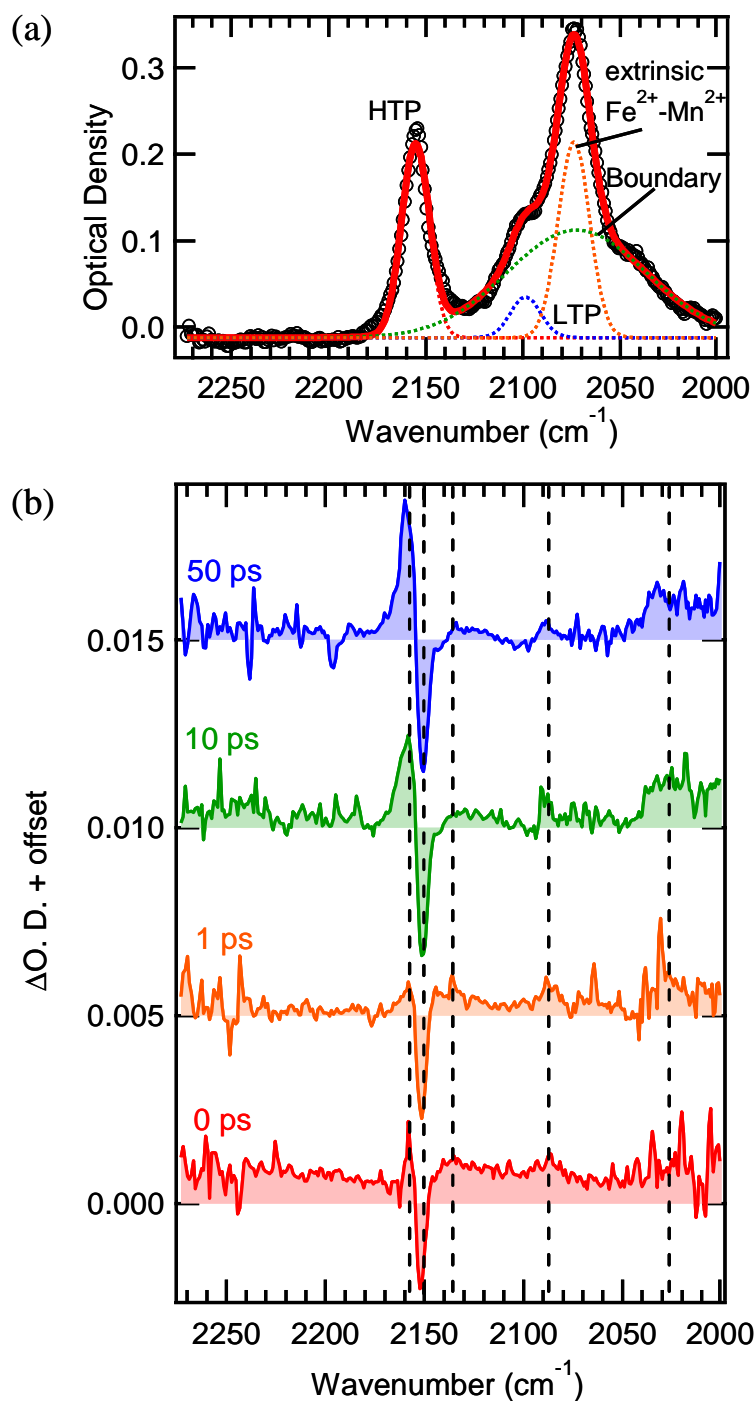
Fig. 3.12: (a) Static absorption spectrum of PIHTP during the experiment observing the dynamics of the phase transition from PIHTP to LTP (black circle) and the fitting result (red solid line). The decomposed four components, HTP (red), LTP (blue), boundary (green), and extrinsic Fe^{2+}-Mn^{2+} (orange), are also exhibited as dotted lines. (b) Transient absorption spectra at 0, 1, 10, and 50 ps showing the dynamics of the phase transition from PIHTP to LTP. The excitation density of pump pulses and CW light are 0.25 W cm^{-2} and 1 W cm^{-2}, respectively.
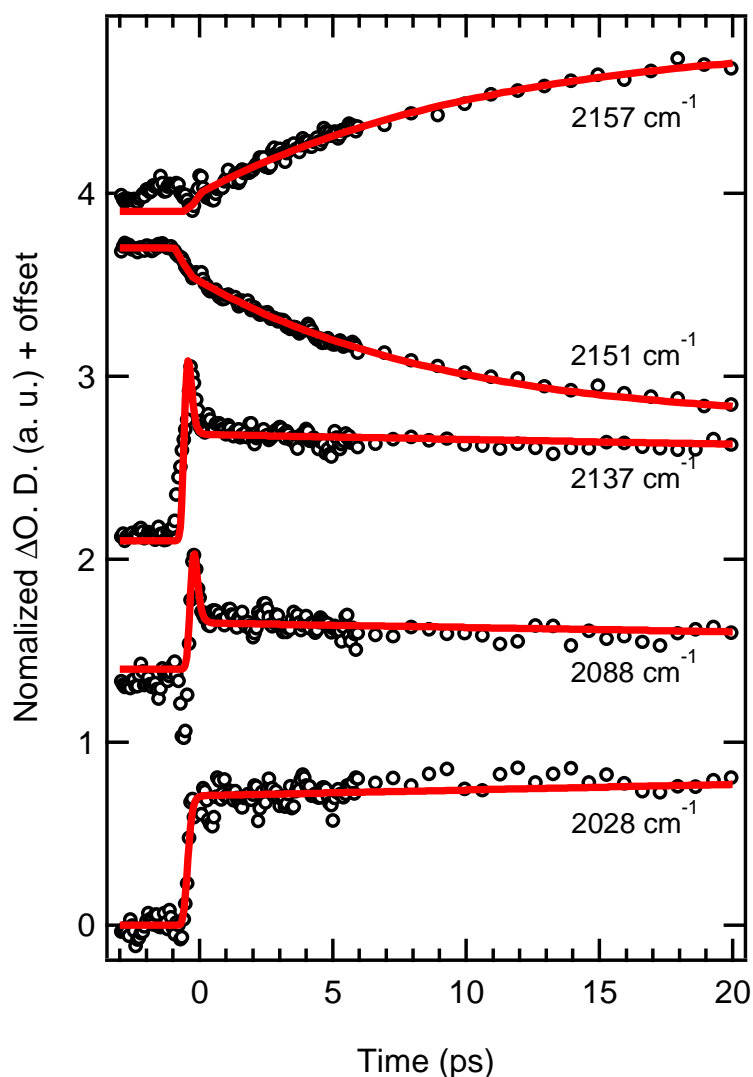
Fig. 3.13: Time evolution curves of normalized transient absorption for the phase transition from PIHTP to LTP at the wavenumbers shown in Fig. 3.12(b) with the vertical dashed lines. The fitting results are inserted as red solid lines.

Transient responses in the PIPT from PIHTP to LTP

Figure 3.12(b) shows transient absorption spectra at various delay times in the transition from PIHTP to LTP. The following two major features are found in these spectra: (i) an intense bipolar signal located around 2155 cm^{-1}, corresponding to the center wavenumber of the PIHTP absorption peak, and (ii) small positive peaks found around 2000-2140 cm^{-1}. Here, we regarded the spiky structures found in these spectra as noise, and they were neglected in the analysis.

47
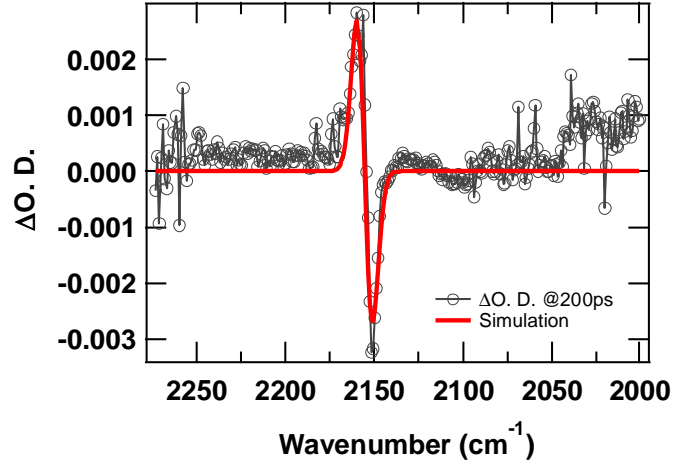
Fig. 3.14: The ΔO.D. spectrum at 200 ps fitted with the derivative of the PIHTP absorption band at 2155 cm^{-1} shown in Fig. 3.12(a).

First, we focus on (i) the intense positive and negative signals around 2155 cm^{-1}. From Fig. 3.14, it is found that the spectral shape around this wavenumber is well fitted with the derivative of the PIHTP absorption band. Therefore, the signal is assigned to a blue shift of the PIHTP peak. In addition, from the evaluations of the ΔO.D. around 2155 cm^{-1}, the value of

Table 3.2: Function forms and time constants of the components used in the fitting procedure shown in Fig. 3.13. The functions of the components at 2137 and 2088 cm^{-1} are superposition of the corresponding two exponential functions. TR denotes the time resolution of 0.26 ps.

Wavenumber	Component	Function	τ_r (ps) (rising time)	τ_d (ps) (decay time)
2157 cm^{-1}	PIHTP blue shift	$1 - \exp(-t/\tau_r)$	8.2	$\gg 100$
2151 cm^{-1}	PIHTP blue shift	$1 - \exp(-t/\tau_r)$	10.5	$\gg 100$
2137 cm^{-1}	LTP or Boundary	$1 - \exp(-t/\tau_r)$	< TR	$\gg 100$
	nonlinear effect	$\exp(-t/\tau_d)$	< TR	0.27
2088 cm^{-1}	LTP or Boundary	$1 - \exp(-t/\tau_r)$	< TR	$\gg 100$
	nonlinear effect	$\exp(-t/\tau_d)$	< TR	0.59
2028 cm^{-1}	Boundary	$1 - \exp(-t/\tau_r)$	< TR	$\gg 100$

48
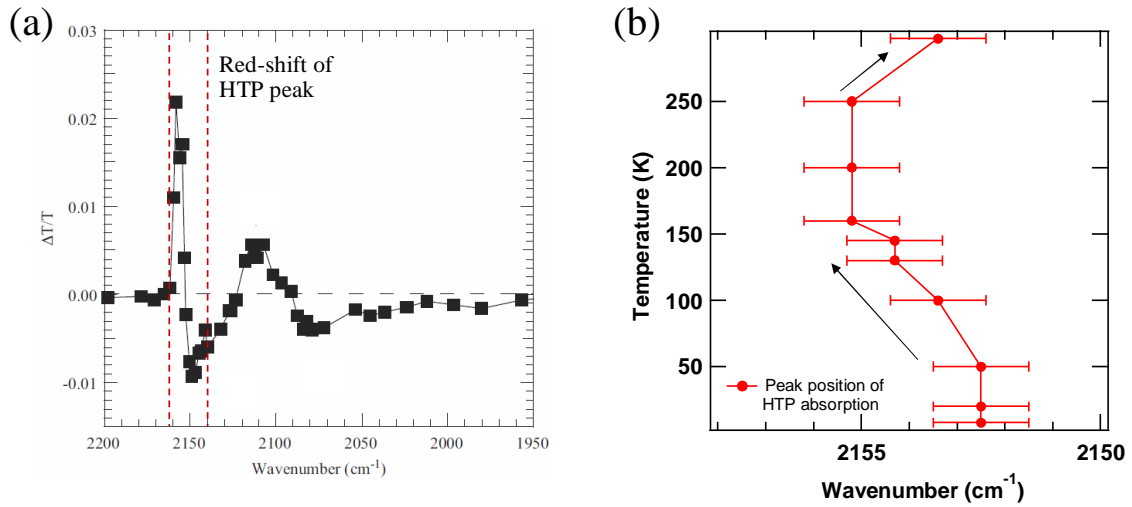
Fig. 3.15: (a) $\Delta T/T$ spectrum in photoinduced HTP-to-PILTP transition at room temperature in RbMn[Fe(CN)$_6$] [88]. Note the direction of the signal in $\Delta T/T$ is inverse to that in ΔO.D. (b) The temperature dependence of the peak position of the PIHTP (or HTP) absorption band.

the blue shift is estimated to be about 0.20 cm^{-1}. Here, as shown in Fig. 3.13, we measured the time evolutions at the five wavenumbers shown in Fig. 3.12(b) with the vertical dashed lines. Their time constants were extracted by fitting the curves with the suitable functions summarized in Table. 3.2. As it is found from this analysis, the time evolutions at 2157 and 2151cm^{-1} corresponding to the positive and negative components due to the blue shift, respectively, gradually change with rising time constants of about 10 ps. These signals last longer than 100 ps. Since the response time of ~10 ps is a typical value widely found in PIPTs [7, 98], we attributed the shift to local lattice deformation caused by laser-induced local heating.

This assignment can be further supported from the direction of the peak shift. In a similar research investigating the transition dynamics from HTP to PILTP (Photoinduced LTP) at room temperature [88], the HTP peak was shifted in the inverse direction (red shift) as shown in Fig. 3.15(a) (Here, note the direction of the signal in $\Delta T/T$ is inverse to that in ΔO.D.). This observation can be explained by the temperature dependence of the peak frequency shown in Fig. 3.15(b); upon heating the sample, the peak frequency gradually increases till around 160 K (blue shift), and then it turns to decrease above around 250 K (red shift).

Second, (ii) we discuss the broad positive signals seen around 2000-2140 cm^{-1} in Fig. 3.12(b). A broad spectral component is found at around 2028 cm^{-1} particularly in the spectra at 10 ps and 50 ps. It can be assigned to production of the boundary configurations, because in

49
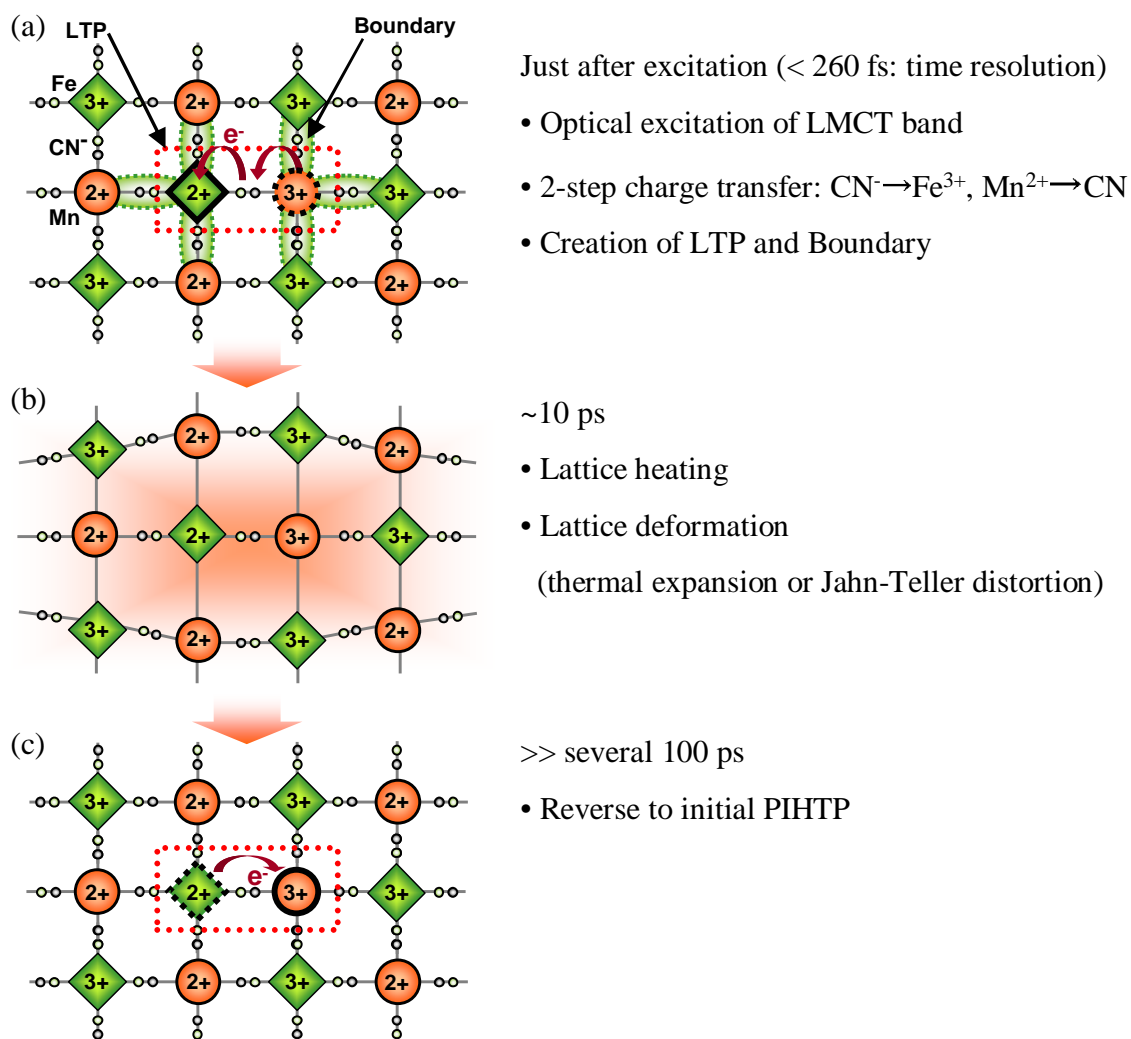
Fig. 3.16: Schematic of the dynamics in the PIPT from PIHTP to LTP.

this low-frequency region the only possible combination of the valence numbers is the lowest valence pair Fe^{2+}-CN-Mn^{2+}. From Fig. 3.13, it is found that the component rises within the time resolution and survives longer than 100 ps. This means that the instantaneous charge transfer from Mn^{2+} to Fe^{3+} induces the boundary configuration at the same time, which persists longer than 100 ps.

In addition, two small positive signals at 2137 and 2088 cm^{-1} are also found in Fig. 3.12(b). These two components are tentatively ascribed to productions of LTP and/or boundary from the empirical law shown in Table. 2.1, although the resonance wavenumbers are slightly different. The reasons for these wavenumber deviations are explained as follows. In the phase transition from HTP to LTP, such deviations of about 10 cm^{-1} are commonly observed [82]. It has

been shown that the wavenumber shifts are caused by local strains due to a lattice mismatch when the tetragonal LTP domain is optically generated in the background of nearly cubic PIHTP. The time evolution curves at 2137 and 2088 cm^{-1} shown in Fig. 3.13 were reproduced by the following two components. One is the spike-shaped curve with a time width of the pump duration. This component is tentatively assigned to some nonlinear effect mentioned in the previous section, and is not related to the phase transition. The essential component is another one, which has a step-like response and survives longer than 100 ps. It corresponds to instantaneous creations of LTP and/or boundary configurations caused by the photoinduced charge transfer from Mn^{2+} to Fe^{3+}. The origin of this step-like component is probably the same as the signal observed around 2028 cm^{-1}.

Scenario of the PIPT from PIHTP to LTP

From these analyses, the scenario of the transition from PIHTP to LTP is summarized as shown in 3.16(a)-(c). When 400-nm light irradiates the sample, charges on Mn^{2+} sites are transferred to Fe^{3+} in a very short time (within the time resolution of 260 fs) in spite of the two-step charge-transfer processes. At the same time, LTP and boundary configurations are generated and survive longer than 100 ps. PIHTP configuration probably decreases at the same time, though it was not observed due to the small oscillator strength. In addition, the system is locally heated within approximately 20 ps, and local lattice deformation arises.

3.4   Summary

The transient PIPT dynamics in $RbMn[Fe(CN)_6]$ at low temperature, which is initiated by photoinduced charge transfer, was investigated by visible-pump mid-infrared-probe spectroscopy monitoring CN vibration modes.

The transient behaviors of the CN vibration spectra associated with these PIPTs were understood in terms of the phenomenological model. In the transition from LTP to PIHTP induced by the charge transfer from Fe^{2+} to Mn^{3+}, LTP is reduced within the time resolution of 260 fs. After 1 ps, the boundary configuration increases in accordance with the further decrease of the LTP configuration. The local lattice deformation by the dissolution of the Jahn-Teller distortion takes about 1 ps. The boundary and LTP decay slowly and survive longer than 100 ps. In other words, they are metastable and not persistent. In the transition from PIHTP to

LTP, LTP and the boundary configuration are transiently created within the time resolution and show also slow decay. The local heating and the propagation of lattice distortion takes about 20 ps. Here, it is noteworthy that the significant generation of the boundary was observed in both directions of these phase transitions. This suggests that relatively small domains and/or low-dimensional fjord-like domains are created at the early stage of the transition. In other words, the boundary-sensitive ultrafast spectroscopy successfully probed the transient formation of the embryonic nuclei.

In addition, in this experiment, we successfully observed the dynamics of the permanent PIPTs by avoiding the accumulation of the photo-induced phase as explained in Sec. 3.2.3. This method, using the reversing CW light, can be applied to other materials which show persistent phase change, provided the phase can be reversed by irradiating at different wavelengths.

Chapter 4

Time-resolved Faraday Rotation Spectroscopy

In $RbMn[Fe(CN)_6]$, the electronic, structural, and magnetic changes are mixed in the PIPT processes as shown in Fig. 2.3. Therefore, in order to reveal the PIPT mechanism, their dynamics should be observed separately . Particularly, the magnetic dynamics of the PIPT in cyano-complexes has not been studied to date. In this chapter, we investigate the magnetic response accompanying the charge transfer PIPT in $RbMn[Fe(CN)_6]$ by time-resolved Faraday rotation spectroscopy. By comparing the results with those obtained from the time-resolved absorption spectroscopy, the electronic, structural, and magnetic dynamics in this PIPT are discussed.

4.1   Faraday rotation spectroscopy

Ultrafast magnetic response in solids has been a very attractive research field in solid state physics [99]. In order to observe the magnetic dynamics, magneto-optic effects are generally used, such as Faraday effect, Kerr effect, Cotton-Mouton effect, or magnetic circular dichroism (MCD). In our experiment, the magnetic dynamics in $RbMn[Fe(CN)_6]$ was probed with Faraday effect, because the sample was a transparent film as mentioned later. Faraday effect is a phenomenon that the polarization plane of the transmitted light rotates linearly proportional to the magnetization M in the material. The Faraday rotation angle θ_F has been
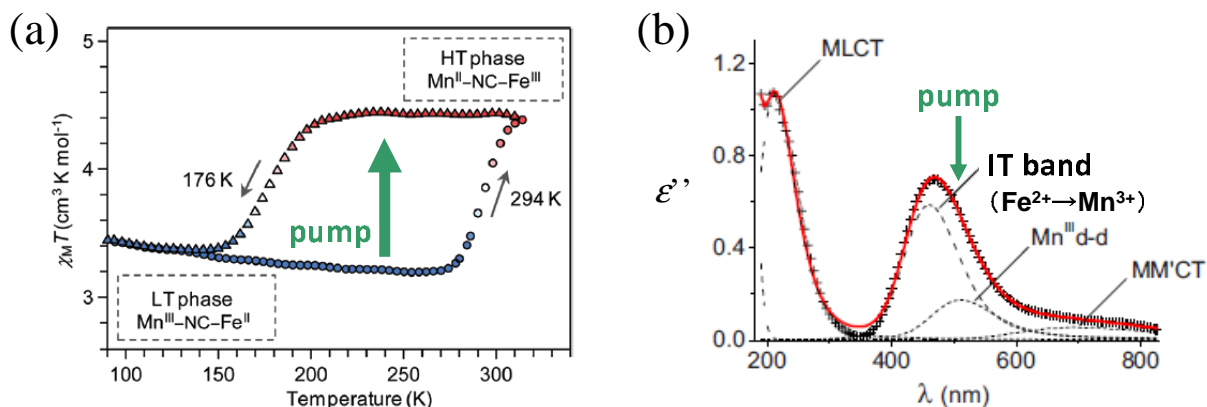
Fig. 4.1: (a) The thermal hysteresis of the magnetic susceptibility in RbMn[Fe(CN)$_6$] [59] and (b) the imaginary part of the dielectric constant in the LTP [83, 84]. The pump conditions in the transient Faraday rotation spectroscopy are shown here.

phenomenologically expressed as:

$$\theta_F = VlH, \tag{4.1}$$

where V is the Verde constant intrinsic to the materials, l is the thickness of the material, and H is the magnetic field parallel to the direction of the transmitted light. With this relation, we can quantify the magnetic response in the sample by measuring the transient rotational change of the polarization angle $\Delta\theta_F$.

4.2 Experiment

4.2.1 Purpose of transient Faraday rotation measurement

As it was explained in Sec. 2.2.6, RbMn[Fe(CN)$_6$] shows the PIPT from LTP [Fe^{2+}(S=0)-CN-Mn^{3+}(S=2)] to HTP [Fe^{3+}(S=1/2)-CN-Mn^{2+}(S=5/2)] near the thermal hysteresis loop by optical excitation with 532-nm light. In this process, since the total spin angular momentum S varies from 2 to 3, the magnetic susceptibility increases about 50 %. Since HTP and LTP are paramagnetic at this temperature, under appropriate external magnetic field, θ_F proportional to the magnetization M (or total spin angular momentum S) is expected to be observed. In order to investigate the magnetic dynamics of this PIPT, the transient change of θ_F is investigated by pump-probe measurement at various temperatures around the hysteresis loop.

54

4.2.2 Sample preparation

In this experiment, we used a film sample, where RbMn[Fe(CN)$_6$] microcrystals were coated on a sapphire substrate. This film is very similar to that used in the CN vibration spectroscopy described in Chapter 3. The composition was Rb$_{0.94}$Mn[Fe(CN)$_6$]$_{0.98}$ ·1.3H$_2$O. The transition temperatures between HTP and LTP were $T_{1/2\downarrow}$ = 168 K and $T_{1/2\uparrow}$ = 302 K in the cooling and warming processes, respectively. The thickness of the sample was about 1 μm.

This film was mounted on a cryostat. The sample was once cooled down to sufficiently low temperature (about 100 K), and subsequently warmed up above 150 K. In this way, the HTP at room temperature was transferred to LTP. The prepared LTP corresponds to the lower side of the hysteresis in Fig. 4.1(a).

4.2.3 Time-resolved Faraday rotation measurement system

In order to measure the ultrafast magnetic response in the sample, we applied a visible-pump visible-probe Faraday rotation measurement system. The experimental setup is shown in Fig. 4.2(a). Here, a femtosecond regenerative amplifier system pumped by a mode-locked Ti:sapphire laser was used as a light source (wavelength: 800 nm, repetition rate: 1 kHz, pulse duration: 120 fs). The output was separated into pump and probe beams, and each beam was inserted into the two optical parametric amplifiers (OPAs) to convert their wavelengths. The wavelength of the pump light was converted into 550 nm to excite the IT band in the LT phase, inducing the charge transfer from Fe^{2+} to Mn^{3+} and the PIPT from LTP to HTP. This wavelength was fixed during the experiment. On the other hand, the wavelength of the probe light monitoring the Faraday rotation was set to around 420 nm. The transmitted probe light was divided into two beams with horizontal and vertical polarizations by the polarization beam splitter (PBS), and their intensities were detected by the two Si photodetectors. By analyzing the difference of these signals obtained from these two detectors ($I^{hor.} - I^{ver.}$), we can obtain the polarization rotation angle.

The RbMn[Fe(CN)$_6$] film mounted on a cryostat was put between the two Nd permanent magnets, and the external magnetic field of 3800 Oe was applied to the sample during the experiment. Since the magnetization M in RbMn[Fe(CN)$_6$] is saturated by applying about 2000-Oe magnetic field [38], the 3800-Oe magnetic filed was high enough to saturate it. By applying the external magnetic field in the inverse directions and by taking difference of these results, the signals except for the magnetic response were canceled, and only the magnetic

(a) Transient Faraday rotation measurement

Polarizer (45° from the ground)   Sample in a cryostat

Probe $\lambda/2$ plate   PBS

OPA

Ti: S
Regen.
800 nm
1 kHz
120 fs

OPA

$I^{hor.}$ *analyse*

$I^{ver.}$

Pump   Chopper (500Hz)   Delay stage   **H**   Permanent Magnet (reversible)   Si photodetector
($H \sim 3800$ Oe)

(b) Transient absorption measurement

Si photodetector   *analyse*   Sample in a cryostat

$I^{ref.}$ Si photodetector

Probe $I^{sig.}$ *analyse*

OPA

Ti: S
Regen.
800 nm
1 kHz
120 fs

OPA

Pump   Chopper (500Hz)   Delay stage
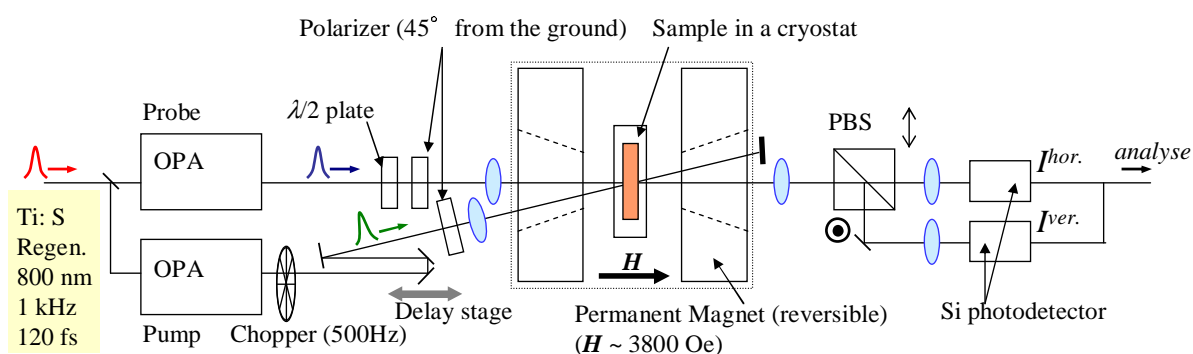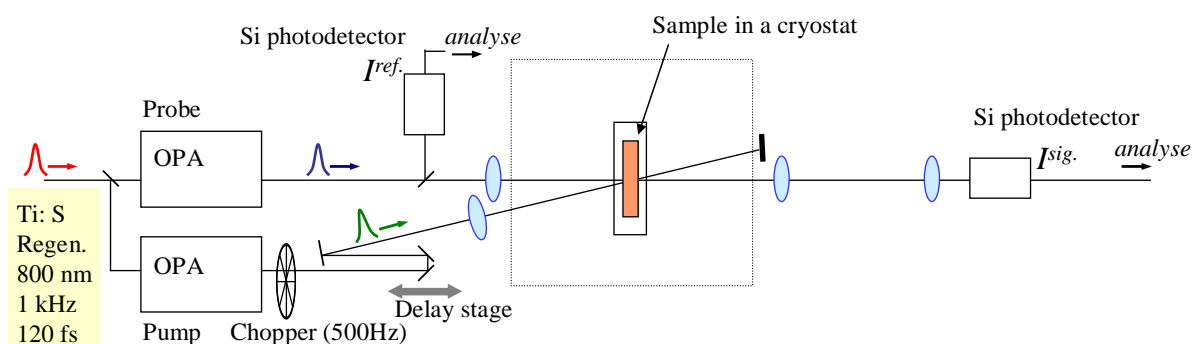
Fig. 4.2: (a) Schematic of the experimental setup of the transient Faraday rotation measurement and (b) that of transient absorption measurement. Here, OPA is optical parametric amplifier, and PBS is polarization beam splitter.

response was obtained.

Additionally, in this system, not only the Faraday rotation, we could also measure the transient absorption with the nearly same experimental setup as shown in Fig. 4.2(b). This experiment corresponds to the transient measurement of the sum of $I^{hor.}$ and $I^{ver.}$ in Fig. 4.2(a) ($I^{sig.} = I^{hor.} + I^{ver.}$). The detector for $I^{ref.}$ was used for balance detection to improve the experimental accuracy. The probe light was fixed at 420 nm, and we monitored the transmittance change $\Delta T/T$ of the LMCT band in the HTP.
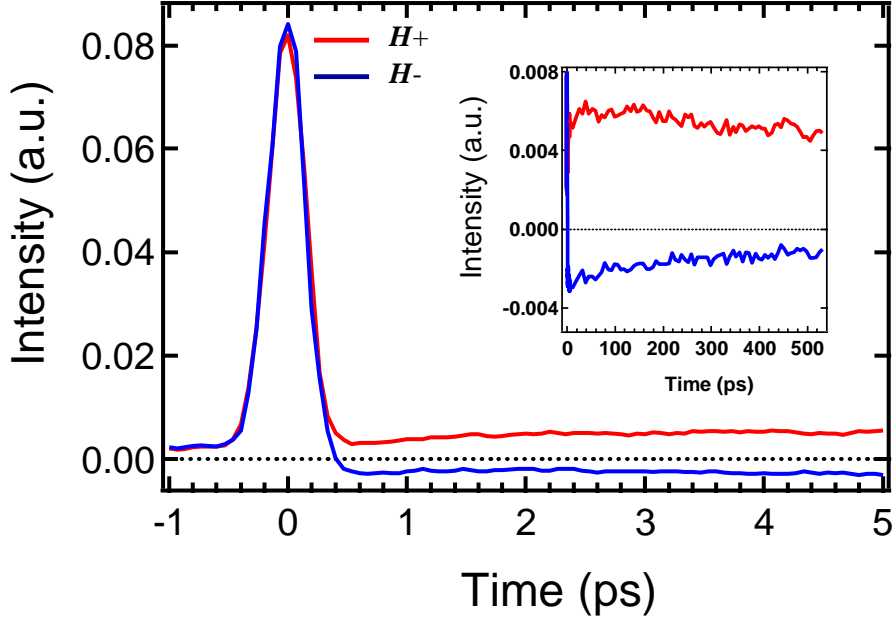
Fig. 4.3: Time evolution curves of the difference intensity between the two detectors ($I^{hor.} - I^{ver.}$) obtained in the pump-probe Faraday rotation measurement. The red ($H+$) and blue ($H-$) curves represent the transient responses obtained when the external magnetic field H was applied in the inverse directions. The inset shows the long scan till about 500 ps.

4.3 Results and discussions

4.3.1 Procedure of data analysis

To begin with, we briefly explain the procedure of the data analysis leading to the transient Faraday rotation. Figure 4.3 shows the typical time evolution curves of the difference intensity between the two detectors ($I^{hor.} - I^{ver.}$) obtained in the pump-probe Faraday rotation measurement. The red ($H+$) and blue ($H-$) curves represent the transient responses obtained when the external magnetic field H was applied in the inverse directions.

Here, the most important feature is the difference between these two curves found after ~0.4 ps, because this difference corresponds to the magnetic response. By taking the difference of these curves, we obtain the time evolution of the transient Faraday rotation.

Around 0 ps, the large positive spikes are also found in both of the curves. This component changed in the same direction when the external magnetic field H was applied in the inverse directions, indicating that its origin is not magnetic responses; this component is attributed to the signal of the transient absorption originated from the sapphire substrate. Therefore, we
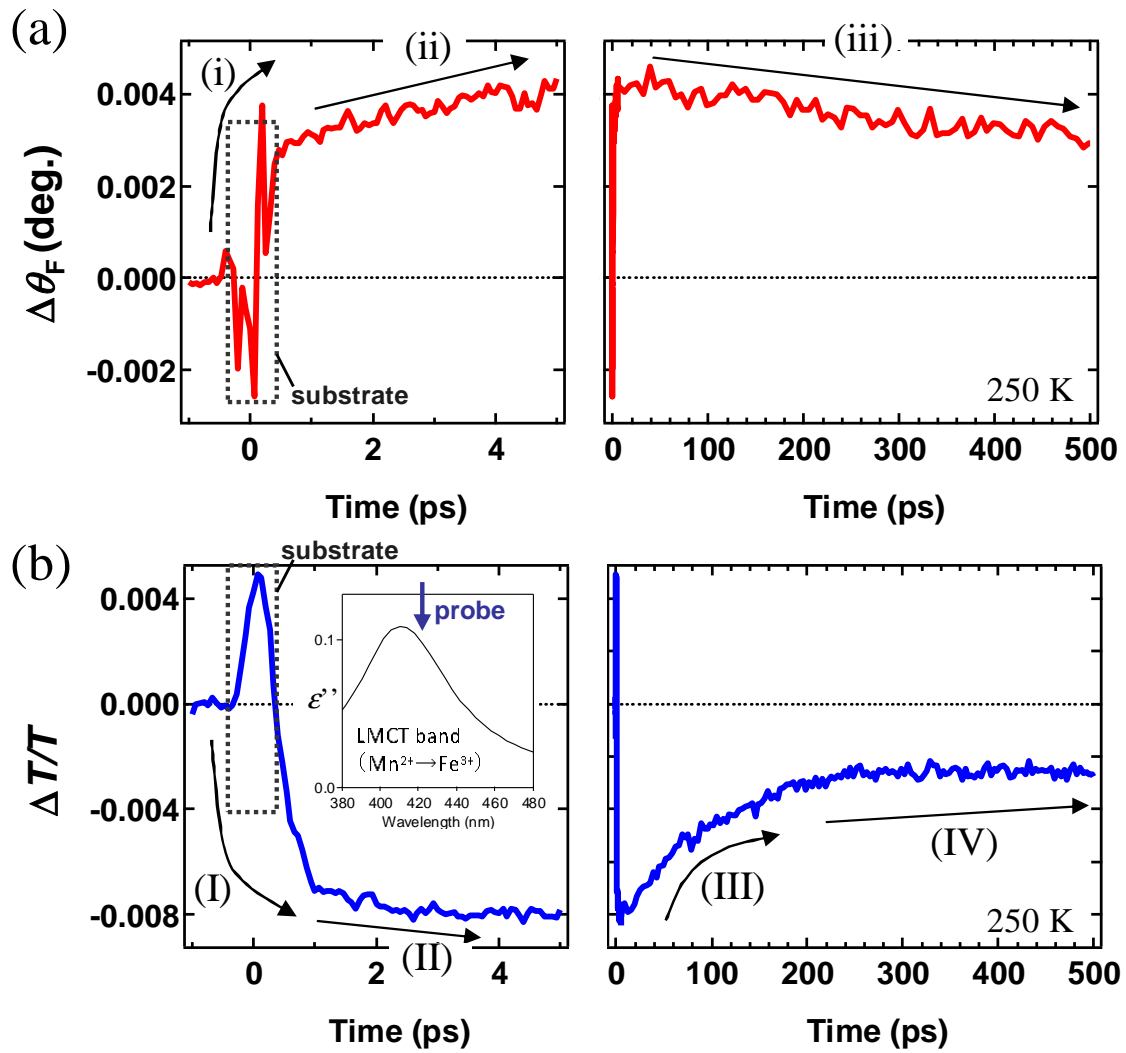
Fig. 4.4: Time evolution curves of (a) transient Faraday rotation $\Delta\theta_F$ and (b) transient absorption $\Delta T/T$ in the PIPT from LTP to HTP measured at 250 K. The Roman indices correspond to the relaxation processes in the PIPT. The sample was pumped by 550-nm pulses (3.5 mJ cm^{-2} pulse^{-1}) and probed by 420-nm pulses. The inset shows the absorption spectrum of the LMCT band in the HTP monitored by the probe light. The signals surrounded by the dotted lines around 0 ps in (a) and (b) are ascribed to the nonlinear response of the sapphire substrate.

neglect this component from the following analysis.

4.3.2 Time evolution of transient Faraday rotation and transient absorption

Figure 4.4(a) shows the time evolution of the transient Faraday rotation $\Delta\theta_F$ calculated from Fig. 4.3. This curve was found to be composed of the three main components: (i) fast rising component within several hundreds of femtoseconds (about the resolution), (ii) gradually rising component taking several picoseconds, and (iii) slow decay component taking more than nanoseconds. Here, we neglected the disturbance of the waveform around 0 ps due to the transient absorption of the sapphire substrate. This disturbance limited the time resolution of the system around 0 ps, involving the characterization of the process (i).

In Fig. 4.4(b), we also show the time evolution of the transient absorption $\Delta T/T$ measured with the setup shown in Fig. 4.2(b). Here, the measurement condition was the same as in the case of the transient Faraday rotation $\Delta\theta_F$. From Fig. 4.4(b), it is found that this curves are composed of the four main components: (I) fast rising component within about 1 ps (decrease of $\Delta T/T$), (II) gradually rising component taking several picoseconds, (III) fast and exponential decay component taking ~90 ps, and (IV) slow decay component taking more than nanoseconds. Here, the positive spike found around 0 ps was neglected, because this component was originated from the sapphire substrate as mentioned above.

When we compare Figs. 4.4(a) and 4.4(b), there can be found several similar time responses. On the other hand, (III) the fast decay component observed in $\Delta T/T$ was not found in $\Delta\theta_F$, which was the clear difference between these two curves.

In the following discussions, the dependences on temperature and excitation fluence are investigated in order to understand the origins of these components.

4.3.3 Temperature dependence

First, we investigated the temperature dependence of $\Delta\theta_F$ till ~10 ps in the warming process at the temperatures around the hysteresis. Figure 4.5(a) shows the time evolutions of $\Delta\theta_F$ at the temperatures from 150 to 340 K. Herein, it is found that the $\Delta\theta_F$ monotonically decreases as the temperature increases, and it disappears at 340 K. When we plot the $\Delta\theta_F$ at 10 ps (circle) against temperature as shown in Fig. 4.5(b), it is found that the $\Delta\theta_F$ steeply decreases around the phase transition temperature of 302 K.

In Fig. 4.5(b), $|\Delta T/T|$ at 10 ps (triangle) observed at various temperatures is also plotted
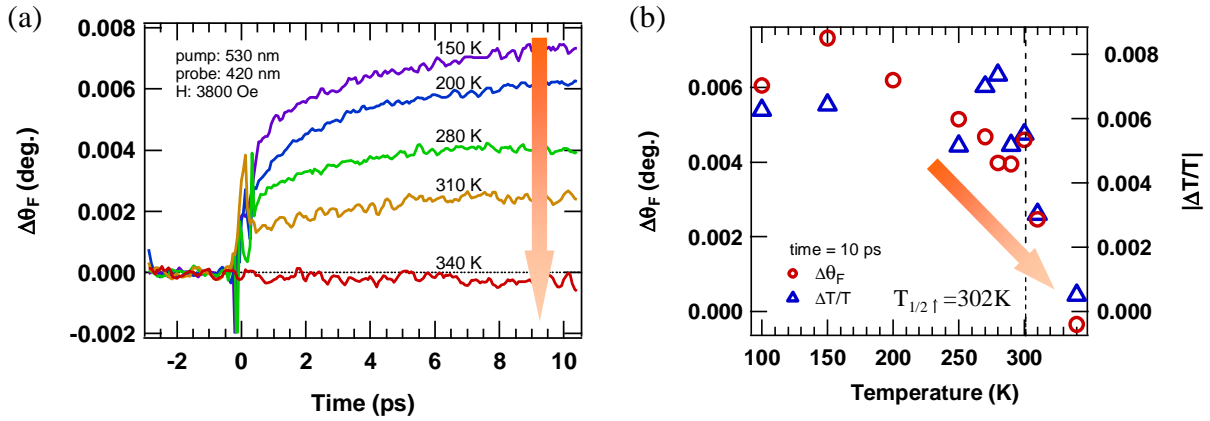
Fig. 4.5: (a) Temperature dependence of $\Delta\theta_F$ till ~10 ps in the warming process at the temperatures around the hysteresis (150-340 K). (b) Temperature dependences of $\Delta\theta_F$ and $\Delta T/T$ measured at 10 ps. The vertical broken line denotes the phase transition temperature of 302 K in the warming process (LTP → HTP).
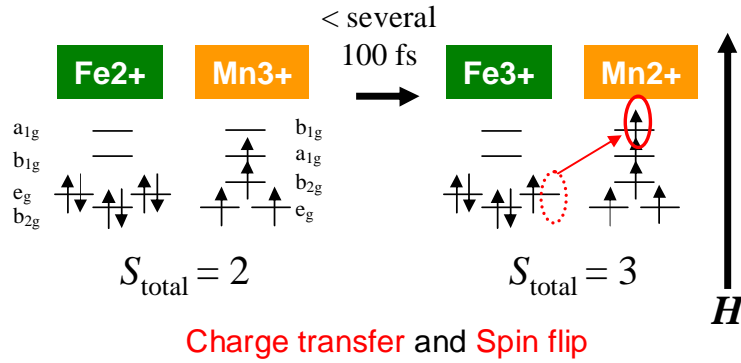
Fig. 4.6: Schematic illustration of the PIPT process within several hundreds of femtoseconds. In this process, the charge is transferred from Fe^{2+} to Mn^{3+}, and the spin state changes at the same time. H denotes the external magnetic field.

(blue triangles). Here, the $|\Delta T/T|$ also decreases around the phase transition temperature of 302 K. As shown in the inset of Fig. 4.4(b), the $|\Delta T/T|$ monitored the amount of transient creation of Fe^{3+}-CN-Mn^{2+} pairs (HTP). Therefore, the decrease of $|\Delta T/T|$ can be naturally assigned to the temperature-induced change of the initial state around 302 K from LTP to HTP. In other words, the charge transfer from Fe^{2+} to Mn^{3+} does not occur above 302 K, because the Fe^{2+}-CN-Mn^{3+} configuration (LTP) does not exist. Then, transient response $|\Delta T/T|$ triggered by the charge transfer is not observed above 302 K.

The $\Delta\theta_F$ has the very similar temperature dependence to that of $|\Delta T/T|$ as shown in Fig. 4.5(b), indicating that the decrease of $\Delta\theta_F$ is also originated from the charge transfer

from Fe^{2+} to Mn^{3+}. Therefore, the magnetic response observed by Faraday rotation is surely assigned to the paramagnetic response. That is, the $\Delta\theta_F$ monitored the increase of paramagnetic magnetization M due to the increase of the total spin angular moment S from 2 to 3 in PIPT from LTP to HTP.

Based on these assignments, the early stage of the PIPT shown in Fig. 4.4 can be interpreted as follows. The interpretation is schematically summarized in Fig. 4.6. First, in the PIPT process, it can be assumed that the charge transfer from Fe^{2+} to Mn^{3+} occurs almost instantaneously. This is the natural assumption, because the charge transfer band (IT band) shown in Fig. 4.1(b) was excited. Within several hundreds of femtoseconds, the $\Delta\theta_F$ steeply increased in the process (i) as shown in Fig. 4.4(a). This fact can be interpreted that the spin state quickly changes under the strong external magnetic field, and the paramagnetic magnetization M (or the total spin angular momentum S) increases[1]. Here, it is notable that the spin orientation follows quickly the charge transfer process within about the system resolution.

On the other hand, the $\Delta T/T$ steeply decreased in the process (I) as shown in Fig. 4.4(b). This transient decrease of the $\Delta T/T$ is basically assigned to the immediate charge transfer from Fe^{2+} to Mn^{3+} as discussed above. However, by looking carefully, this response seems to have the delay about 1 ps, suggesting some delayed component is slightly overlapped to the component originated from the charge transfer. This delayed response is tentatively attributed to the local lattice deformation around the photoexcited sites caused by the dissolution of the Jahn-Teller distortion, which was discussed in Sec. 3.3.2.

4.3.4 Excitation density dependence

Next, we investigated the excitation density dependences of $\Delta\theta_F$ and $\Delta T/T$. The temperature was fixed at 250 K in this experiment.

The excitation power dependence of $\Delta\theta_F$ is shown in Fig. 4.7(a), and the intensity at 4 ps is plotted in Fig. 4.7(b). From these data, it is found that the $\Delta\theta_F$ increases linearly to the excitation power. This observation indicates that the transient increase of the magnetization M is linear to the amount of the optically transferred charges, which is naturally expected.

---

[1]In general, $\Delta\theta_F$ depends not only on the change of M but also on the dielectric responses (the change of the refractive index n and the extinction coefficient κ). Therefore, the effect of such a dielectric response may be overlapped to the $\Delta\theta_F$ curve shown in Fig. 4.4(a). However, in this experiment, the 90-ps decay component (III) observed in $\Delta T/T$ was not found in $\Delta\theta_F$, though the sample has absorption at the probe wavelength. This fact indicates that the dielectric responses have less contribution to the $\Delta\theta_F$ compared to the magnetic response, meaning the fast 1-ps $\Delta\theta_F$ response is attributed to the change of the M.
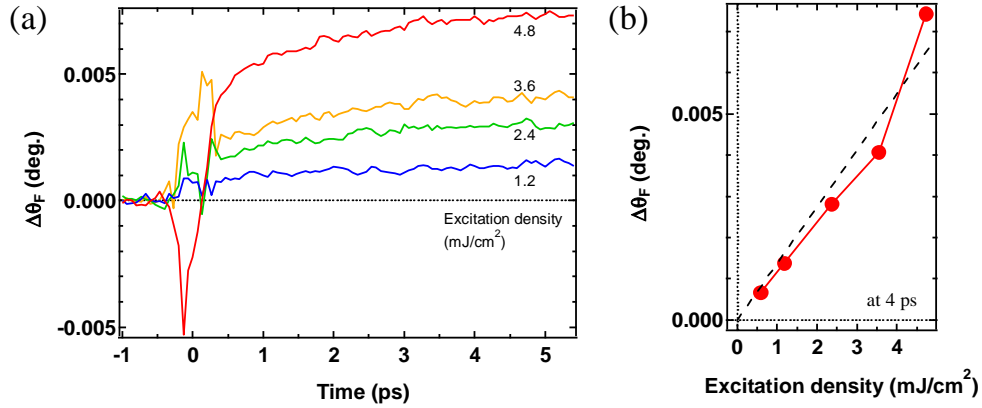
Fig. 4.7: (a) The excitation power dependence of $\Delta\theta_F$ till 5 ps and (b) the plot of the $\Delta\theta_F$ intensity at 4 ps. The dashed line inserted in (b) is eye-guide to show the linearity.
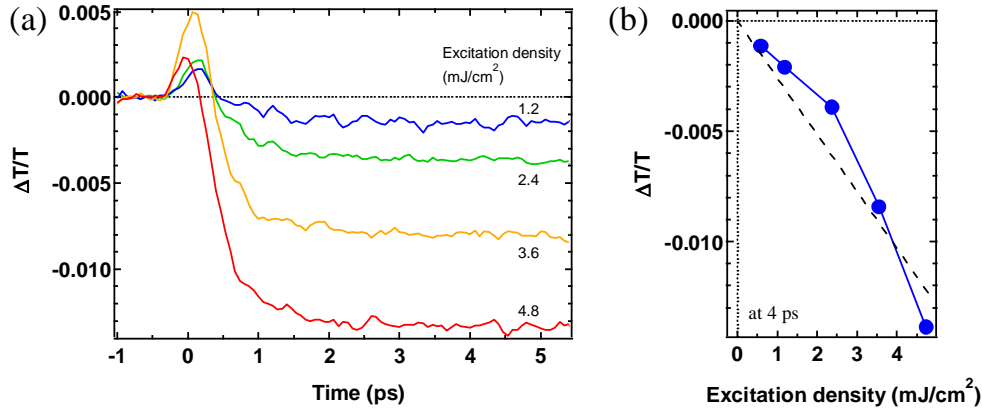
Fig. 4.8: (a) The excitation power dependence of $\Delta T/T$ till 5 ps and (b) the plot of the $\Delta T/T$ intensity at 4 ps. The dashed line inserted in (b) is eye-guide to show the linearity.

Next, the excitation power dependence of $\Delta T/T$ till 5 ps is shown in Fig. 4.8(a), and its intensity at 4 ps is shown in Fig. 4.8(b). Here, it is found that $\Delta T/T$ in this time range changes roughly linear to the excitation power[2], which is the same tendency as in the case of $\Delta\theta_F$ shown in Fig. 4.7. This observation reflects the amount of photoinduced charge transfer itself, which is quite a natural result.

In addition, the excitation power dependence of $\Delta T/T$ in long time range (till 500 ps) is also studied as shown in Fig. 4.9(a). Its intensity at 400 ps, where the 90-ps decay shown in Fig. 4.4(b) (process (III)) is almost relaxed, is plotted in Fig. 4.9(b). Here, in contrast to the early

---

[2]Strictly, the $\Delta T/T$ plot at 4 ps shown in Fig. 4.8(b) was not have a complete linear dependence. However, evident threshold behavior does not observed there, and its nonlinearity seems to be smaller compared to that observed at 500 ps shown in Fig. 4.9(b).
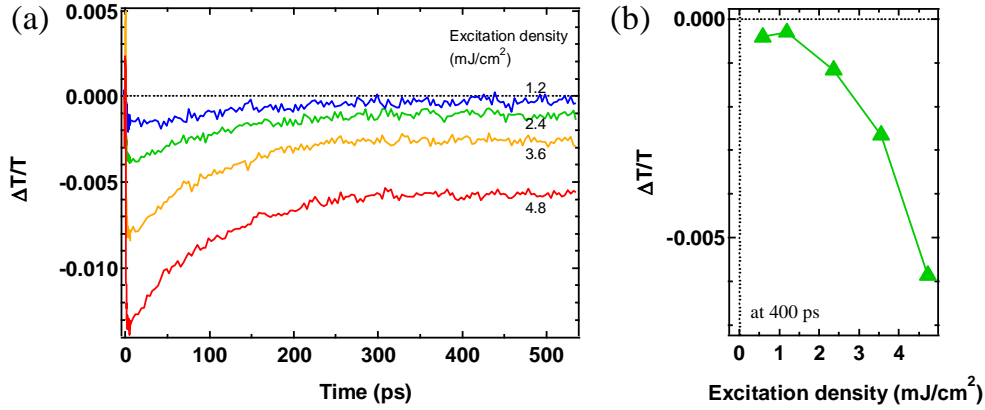
Fig. 4.9: (a) The excitation power dependence of $\Delta T/T$ till 500 ps and (b) the plot of the $\Delta T/T$ intensity at 400 ps.
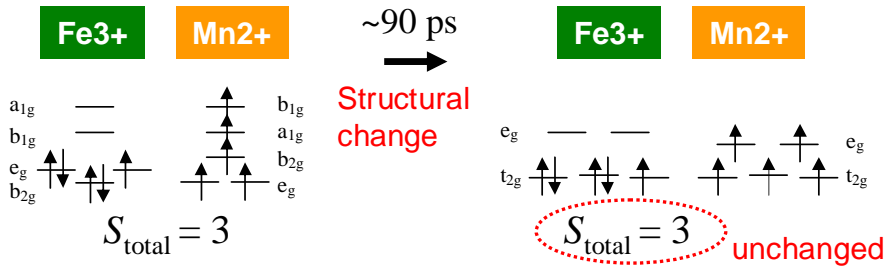
Fig. 4.10: Schematic illustration of the PIPT process around 90 ps. In this process, the structural change occurs from tetragonal to cubic, whereas the total spin angular momentum S is constant.

stages of the PIPT shown in Fig. 4.7(b) and Fig. 4.8(b), the $\Delta T/T$ at 400 ps shows a nonlinear dependence (or a threshold behavior). This suggests that the 90-ps decay component includes some nonlinear process. As a plausible assignment, we interpreted this 90-ps decay component as aggregation of charge transferred sites accompanied by a local lattice deformation. Such a domain creation (or formation of stabilized clusters) process should generally show some nonlinear behavior to the excitation power. When the lattice deformation (from tetragonal to cubic in this case) occurs, the electron distribution is modulated as illustrated in Fig. 4.10. Then, since the absorption spectrum changes at the same time, $\Delta T/T$ change is observed.

Such a decay component with a time constant of several 10 ps was previously reported in Co-Fe cyano-complexes by Kamioka *et al.* [92] as introduced in Sec. 2.3.2. They assigned this process as the formation of self-trapped charge transfer pair accompanied by a local lattice deformation. We speculate that the 90-ps decay observed in our experiment is the similar
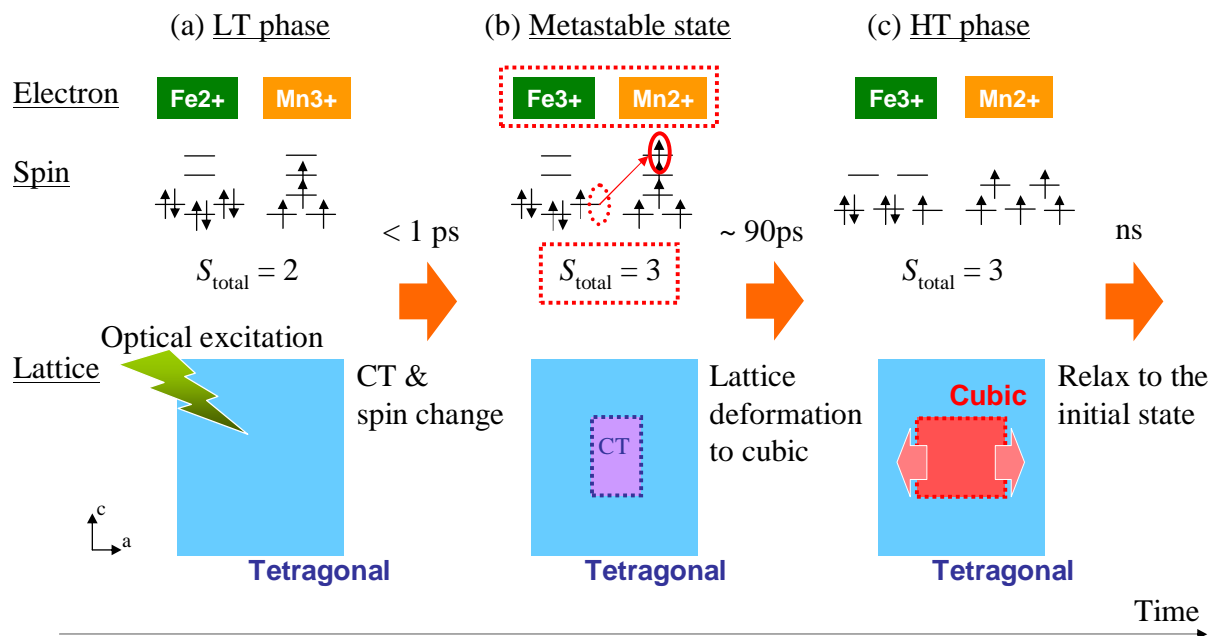
Fig. 4.11: Summary of the interpretation of the PIPT dynamics from LTP to HTP.

phenomenon and that such a relaxation process is common in cyano-complexes.

Here, it is noticeable that the 90-ps decay component found in $\Delta T/T$ was hardly observed in $\Delta \theta_F$ as shown in Fig. 4.4(a). This fact can be consistently understood as illustrated in Fig. 4.10. When the lattice deforms, since the optical transition energy is modulated, the $\Delta T/T$ will change indeed. However, if the crystal field does not change so greatly, the spin state in Fe^{3+} (Mn^{2+}) will be kept in low (high) spin state. Then, the total spin angular momentum S is constant during the lattice deformation, and the $\Delta \theta_F$ does not change. This result indicates that the dynamics of spin system was separately characterized from that of the lattice system, whereas the spin dynamics is strongly coupled to the electronic (or valence state) dynamics.

4.3.5 Scenario of the PIPT

Based on these analyses, the interpretation of the PIPT dynamics is summarized, and the PIPT model is proposed as shown in Fig. 4.11.

- Process (i): < several 100 fs
  When LTP is irradiated with 550-nm pulses exciting IT band (Fig. 4.11(a)), charges are instantaneously transferred from Fe^{2+} to Mn^{3+}. Following this change, a metastable electronic state is created (Fig. 4.11(b)). Here, the total spin angular momentum S_{total}

changes from 2 to 3 within several 100 fs, and the paramagnetic magnetization M increases. This magnetic change is observed as the transient Faraday rotation $\Delta\theta_F$.

- Process (I): $< \sim 1$ ps

  The lattice locally deforms around the charge-transferred sites due to the dissolution of the Jahn-Teller distortion. However, the tetragonal lattice is expected to be almost frozen at this stage, because the structural change is not so extensive (Fig. 4.11(b)).

- Processes (ii) and (II): $<$ several ps

  The origin of the gradual rising components taking several picoseconds shown in Figs. 4.4(a) and (b) is not so clear. However, it could be ascribed to some cooperative charge transfer which occurs after light irradiation.

- Process (III): $< \sim 90$ ps

  Local lattice deformation occurs around the optically excited area due to the aggregation of the charge-transferred sites within about 90 ps. When the structure changes from tetragonal to cubic (Fig. 4.11(c)), the electronic distribution will be changed among the sub-levels split by the crystal field. On the other hand, the total spin angular momentum is constant with this structural deformation probably because the low (high) spin state in Fe^{3+} (Mn^{2+}) is conserved. Therefore, this relaxation process can be observed in $\Delta T/T$, but not in $\Delta\theta_F$.

- Processes (iii) and (IV): $>$ ns

  The excited HTP domain reverses to the initial LTP taking a time longer than several ns.

4.4   Summary

In this chapter, we investigated the ultrafast magnetic response in $RbMn[Fe(CN)_6]$ by Faraday rotation spectroscopy. By comparing the results with those obtained from the transient absorption spectroscopy, we interpreted the PIPT dynamics including the magnetic response.

From the temperature dependence, it is found that the Faraday response reflects the change of paramagnetic magnetization triggered by the charge transfer. From the power dependence, it is also found that the Faraday rotation reflects the amount of the transferred charge, indicating the strong correlation between spin and electronic states.

We interpreted the PIPT dynamics as follows, and the PIPT model was proposed. After 550-nm light irradiation, the instantaneous charge transfer from Fe^{2+} to Mn^{3+} occurs. In almost the same time scale (< several 100 fs) the fast spin-flip process occurs. Within ~1 ps, the local small deformation occurs around the charge-transferred sites. Subsequently, some cooperative charge transfer occurs taking several picoseconds. In the relaxation process, the lattice slowly deforms taking about 90 ps due to the aggregation of the charge-transferred sites. Here, since the spin state does not change in this process, this decay component is absent in the Faraday response, while it can be observed in the transient absorption. The excited state relaxes to the initial LTP taking longer than nanoseconds.

From this experiment, it is suggested that the electronic, structural, and spin dynamics in the picosecond region in $RbMn[Fe(CN)_6]$ were separately characterized. It is noticeable that the paramagnetic spin system follows the instantaneous changes in the electronic system, while the lattice system slowly relaxes taking about 90 ps. Since the spin state probed by the Faraday effect is decoupled from the lattice relaxation, the Faraday effect is expected to be more appropriate for detecting the charge transferred states compared to transient optical absorption in this case.

Part II

nano-granular Ti$_3$O$_5$

Chapter 5

Background: Ti$_3$O$_5$

Nano-granular trititanium pentaoxide (Ti$_3$O$_5$) shows the photoreversible semiconductor-metal phase transition at room temperature. Since the details of the PIPT behavior and its mechanism remain unclear, researches on this material have been demanded. In this chapter, the previous researches and the properties on Ti$_3$O$_5$ are summarized, which will be the basic knowledge to understand the results described in the following chapters. The objective of this research is described at the end of this chapter.

5.1   Phase transitions in titanium oxides

Titanium oxides have been widely used as photocatalysts or solar cells. Since the element Ti is non-toxic and economical, titanium oxides have been highly expected for their sustainability as functional materials. Furthermore, this family of materials is fascinating, because they exhibit various types of phase transitions or optical responses depending on their stoichiometric ratios, e.g., TiO$_2$ [100], Ti$_2$O$_3$ [101, 102], or Ti$_4$O$_7$ [103–105]. Especially, Ti$_n$O$_{2n-1}$ ($n \geq 4$), having a structure called Magnéli phase, is well known for showing interesting metal-nonmetal phase transitions, which results from complicated interactions between their *3d* electrons and their shear structures [113]. Here, we particularly focus on Ti$_3$O$_5$, which also shows similar metal-nonmetal phase transitions, though it does not have Magnéli structures.

69
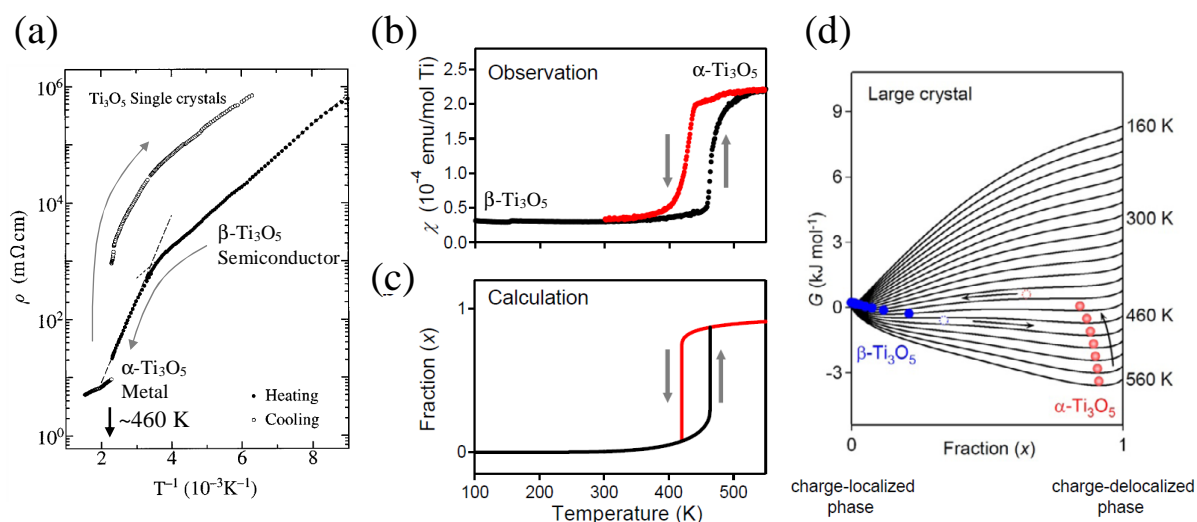
Fig. 5.1: (a) Conductivity dependence on temperature in large Ti_3O_5 crystal [114]. (b) Experimental results and (c) calculation of magnetic susceptibility dependence on temperature, and (d) calculated potential curves at various temperatures [106]. These calculations were obtained by Slichter-Drickamer mean-field model [76].

5.2 Properties of Ti_3O_5

The properties of Ti_3O_5 are summarized below. This material has been well known to show the temperature-induced metal-semiconductor phase transition (α and β phases), whose details are described in Sec. 5.2.1-5.2.2. In 2010, nano-granular Ti_3O_5 was newly synthesized by Ohkoshi group [106]. The following studies revealed the novel characteristics in this nanoparticle. First, a metallic phase (λ phase) exists at room temperature. Second, the λ phase is optically switched reversibly to the β phase, meaning photoinduced metal-semiconductor phase switching. The properties of nano-granular Ti_3O_5 are summarized in Sec. 5.2.3-5.2.5.

5.2.1 Temperature induced phase transition between α- and β-Ti_3O_5

Ti_3O_5 in a macroscopic crystal form shows the temperature-induced metal-semiconductor phase transition [106, 107, 113–116]. The temperature dependence of the conductivity in Ti_3O_5 is shown in Fig. 5.1(a). The conductivity changes two orders of magnitudes around 460 K in both heating and cooling processes, indicating the occurrence of metal-nonmetal phase transition. The metallic phase (α phase) is stable at higher temperatures, while the semiconductor phase (β phase) is stable at lower temperatures, including room temperature.

70

Figure 5.1(b) shows the magnetic susceptibility changes accompanied by the phase transition. This curve has the clear hysteresis of approximately 40 K width, indicating this phase transition is the first-order. The mechanism of this phase transition can be thermodynamically explained by Slichter-Drickamer mean-field model (SD model) [76, 106], as in the case for RbMn[Fe(CN)$_6$] in Chapter 2. In the SD model, the Gibbs free energy G is defined as:

$$G = x\Delta H + \gamma x(1 - x) + T[R[x\ln x + (1 - x)\ln(1 - x)] - x\Delta S], \tag{5.1}$$

where G is the Gibbs free energy, x is the fraction of metallic α phase, ΔH is the transition enthalpy, γ is the interaction constant, R is the gas constant (= 8.31 m^2 kg s^{-2} K^{-1} mol^{-1}), and ΔS is the transition entropy. By substituting the appropriate parameters evaluated from the thermodynamical experiments [106], ΔH = 13.3 kJ mol^{-1}, γ = 9.3 kJ mol^{-1}, and ΔS = 29.4 J K^{-1} mol^{-1}, the potential curves at various temperatures were calculated as shown in Fig. 5.1(d). At 520 K, α phase is the true ground state and is stable. Upon cooling, the potential shape continuously deforms. At 420 K, the energy barrier annihilates, and the α phase transfers to β phase. Inversely upon heating from there, the β phase is kept till 460 K due to the energy barrier, and it transfers to α phase when the sample is further heated. This model well reproduces the thermal hysteresis in the first-order phase transition as shown in Fig. 5.1(c).

5.2.2 Properties of α- and β-Ti$_3$O$_5$

The physical properties of bulk Ti$_3$O$_5$ have been studied in electrical, thermodynamic, and crystallographic investigations [106, 107, 113–121]. The structural information was deduced from the x-ray diffraction (XRD) measurement and the Rietvelt analysis (a typical technique analyzing the crystal structures) [106]; the crystal structures of the α and β phases are orthorhombic (*Cmcm*) and monoclinic (*C2/m*), respectively. The lattice constant along the c axis for the α phase is about 5% larger than that for the β phase, which originates from bi-polaron formation mentioned later. The detailed structural parameters are summarized with their conductive properties in Table 5.1.

The crystal structure in β phase is shown in Fig. 5.2(a). It comprises of TiO$_6$ octahedra connected with shared edges and corners. There are three nonequivalent Ti ions in an unit cell. The valence states for the three Ti ions can be empirically estimated from the distance between Ti-O ions, which can be evaluated from the Rietvelt analysis [118]. From this relation, the
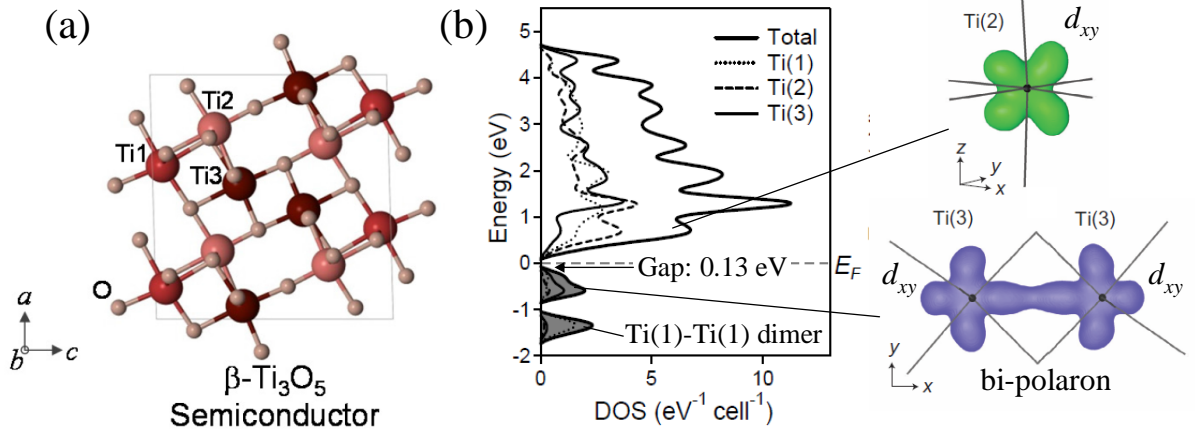
Fig. 5.2: (a) Crystal structure and (b) density of states of β-Ti$_3$O$_5$ [106]. The orbitals drawn in the right side constitute the corresponding energy bands.

valence states in α phase were estimated to be nearly Ti$^{10/3+}$-Ti$^{10/3+}$-Ti$^{10/3+}$, meaning this phase is carrier-delocalized metallic state indeed. On the other hand, in β phase, the valence states were estimated to be close to Ti^{3+}-Ti$^{11/3+}$-Ti$^{10/3+}$. This means that the β phase has a charge ordering and the carriers are localized, resulting in semiconductor-like dc conductivity ($\sigma = \sim3 \times 10^{-2}$ S cm^{-1}).

The density of states in semiconductor β phase was obtained by the first principle calculation as shown in Fig. 5.2(b) [106]. The energy bands near the Fermi energy E_F consist of $3d$ orbitals of the Ti ions. The t_{2g} orbitals are split by Coulomb interactions between neighboring Ti ions (Mott-Hubbard-typed semiconductor), and the band gap is about 0.13 eV.

Table 5.1: The physical properties in α-, β-, and λ-Ti$_3$O$_5$ [106, 107]

Phase	Conductivity	Symmetry	Lattice parameters				
			a(Å)	b(Å)	c(Å)	V(Å^3)	β(°)
α	Metal	Orthorhombic (*Cmcm*)	9.86	3.80	10.0	375	90.0
β	Semiconductor (band gap: 0.13 eV)	Monoclinic (*C2/m*)	9.75	3.80	9.45	350	91.6
λ	Metal	Monoclinic (*C2/m*)	9.84	3.79	9.97	372	91.3

72
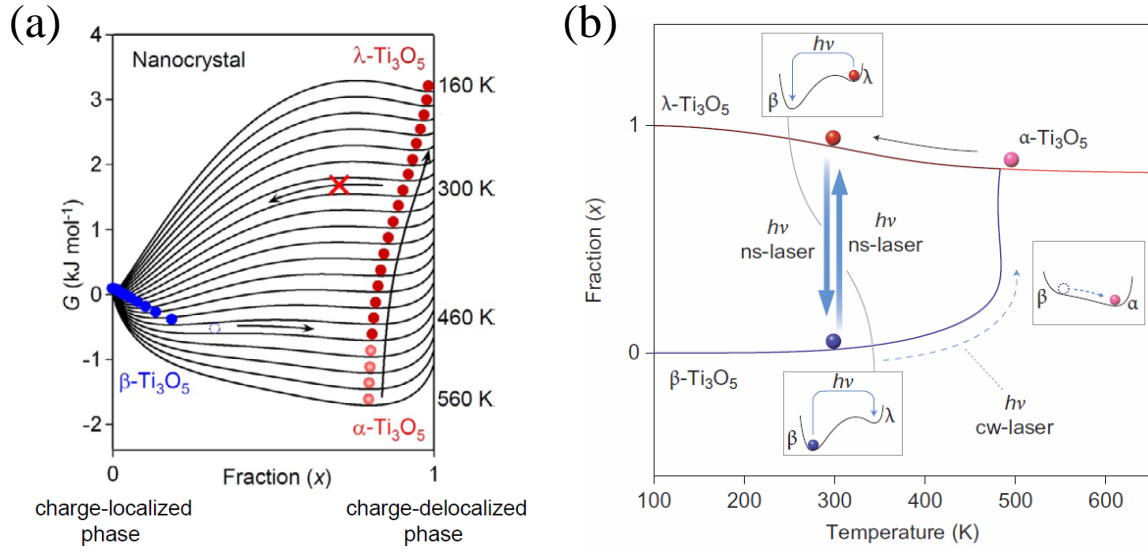
Fig. 5.3: (a) Free energy curves obtained by Slichter-Drickamer model and (b) the schematic of the phase transitions in nano-granular Ti_3O_5 [106]. The second-order thermal phase transition occurs between α and λ phases. The reversible phase switching is induced by optical pulse excitation between λ (metastable state) and β (ground state) phases. When the photo-created β phase is heated by irradiating with a CW laser, it is transferred to λ phase through α phase.

The valence band is formed by bi-polaron of Ti(3)-Ti(3) σ-bonding at -0.60 eV and Ti(1)-Ti(1) dimer at -1.35 eV. The conduction band near E_F is mainly formed by d_{xy} orbital of Ti(2) located at 0.71 eV.

5.2.3   Nanoscale effects on stabilization of λ-Ti_3O_5

In nano-granular Ti_3O_5, metallic λ phase can exist at room temperature. Although this phase cannot exist in macroscopic crystals, it is thermodynamically stable due to nanoscale size effects. This stabilization mechanism can be qualitatively explained by the contribution from the surface (or interface) energy [106–108]. The Gibbs free energy G per unit volume is generally decomposed as:

$$G/V = G_B/V_m + 6G_S/d, \qquad (5.2)$$

where G_B is the bulk energy (chemical potential of a particle), V_m is the molar volume, d is the diameter of nanoparticles, and G_S is the surface energy per unit area [109]. At low temperatures, the semiconductor β phase is stable, indicating $G_B^{metal} > G_B^{semiconductor}$. In order to understand the experimental facts, the surface energy should satisfy the relation,
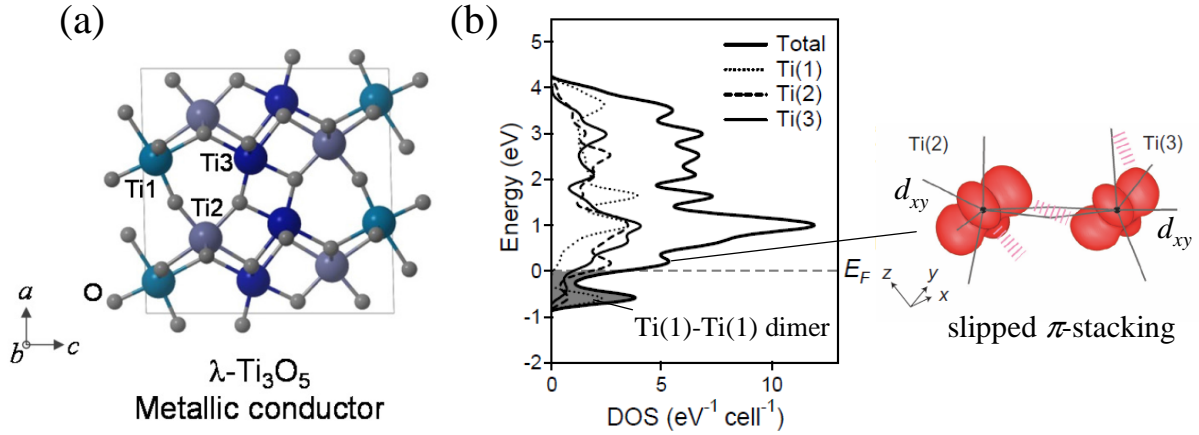
Fig. 5.4: (a) Crystal structure and (b) density of states of λ-Ti$_3$O$_5$ [106]. The orbitals shown in the right side constitute the corresponding energy bands.

$G_S^{metal} < G_S^{semiconductor}$. If this condition is satisfied, the metallic phase arises when the diameter d becomes smaller than a critical size. In this material, it can be explained that when the diameter reaches on the order of nm, the metallic phase becomes stable.

Calculated by the SD model as in the case in Sec. 5.2.1, the free energy curves were obtained at various temperatures as shown in Fig. 5.3(a). At 560 K, the metallic α phase is stable. Upon cooling, the potential curve gradually deforms. Since the free energy of the metallic phase decreases due to the nanoscopic effect, the metallic phase stably exists at low temperatures due to the energy barrier. The α phase transfers to the λ phase at 460 K. This is the second-order phase transition; the schematic of the phase transition (the phase fraction vs. Temperature) is shown in Fig. 5.3(b).

5.2.4 Properties of λ-Ti$_3$O$_5$

The properties of λ phase have been investigated by various kinds of methods [106–108, 110–112]. The crystal structure of λ phase is shown in Fig. 5.4(a). The λ phase has a monoclinic structure and belongs to the space group $C2/m$, which is the same space group as that of the β phase. However, it differs in that the lattice constant along the c axis for the λ phase is about 5% larger than that for the β phase. In the λ phase, every inequivalent Ti ion has a valence state close to Ti$^{10/3+}$ and the amplitude of the charge-density fluctuation is smaller than that in the β phase, resulting in a carrier-delocalized system, which is very similar in the case of α phase. Consequently, the λ phase is a metal state indeed. Nevertheless, the dc conductivity
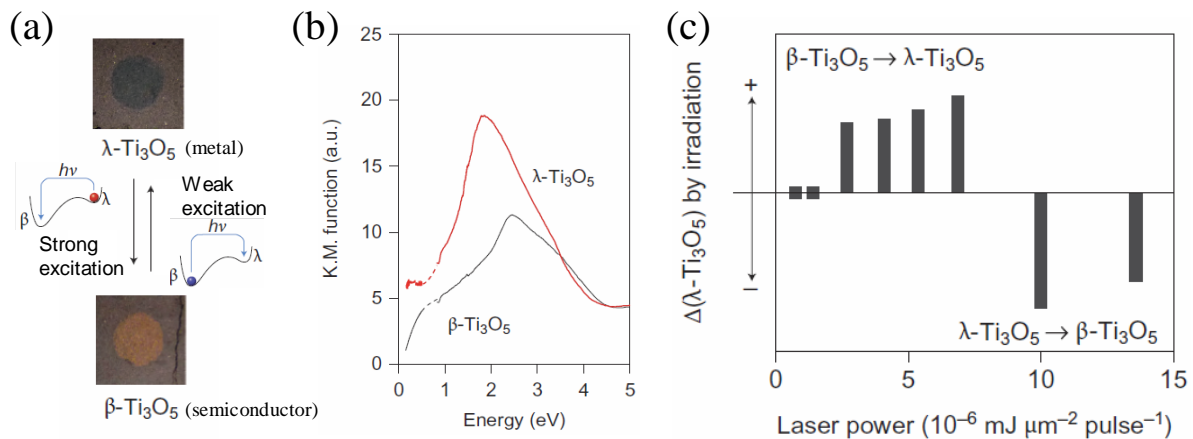
Fig. 5.5: (a) The schematic of the photoinduced switching between λ and β phases in nano-granular Ti$_3$O$_5$ [106]. (b) Optical absorption spectra of λ (red) and β phase (black). K.M. is Kubelka-Munk transformation [106,122], which roughly corresponds to the absorption spectrum of light-diffusing sample. (c) Excitation power dependence of λ phase fraction [106].

σ of λ-Ti$_3$O$_5$ nanocrystal was measured to be 30 S cm^{-1} at room temperature [106]; this low conductivity indicates λ-Ti$_3$O$_5$ is a bad metal. These electronic property and lattice constants of the λ phase are similar to those of the metallic α phase, while the crystal symmetry is equal to that of the β phase. These properties are summarized in Table. 5.1 with those in α and β phases.

The density of states in λ phase was calculated as shown in Fig. 5.4(b). As in the case of β phase in Fig. 5.2(b), the energy bands near the Fermi energy E_F consist of 3d orbitals in Ti ions. The valence band is composed of Ti(1)-Ti(1) dimer located at -0.58 eV. The conduction band close to E_F is mainly formed by the slipped π-stacking (like a zigzag chain) between the d_{xy} orbitals on Ti(2) and Ti(3). The metallic conduction in λ phase is caused by this π-stacking.

5.2.5 Photoinduced metal-semiconductor phase switching in nano-granular Ti$_3$O$_5$

The metallic λ phase and the semiconductor β phase can be reversibly switched by optical excitation as shown in Figs. 5.5(a) and 5.3(b) [106]. The optically-created phase configurations were confirmed by the XRD measurements. This was the first demonstration of a photoreversible oxide at room temperature, and has recently attracted considerable attention because of its applicability to optical data storage. Accompanied by these phase transitions, the
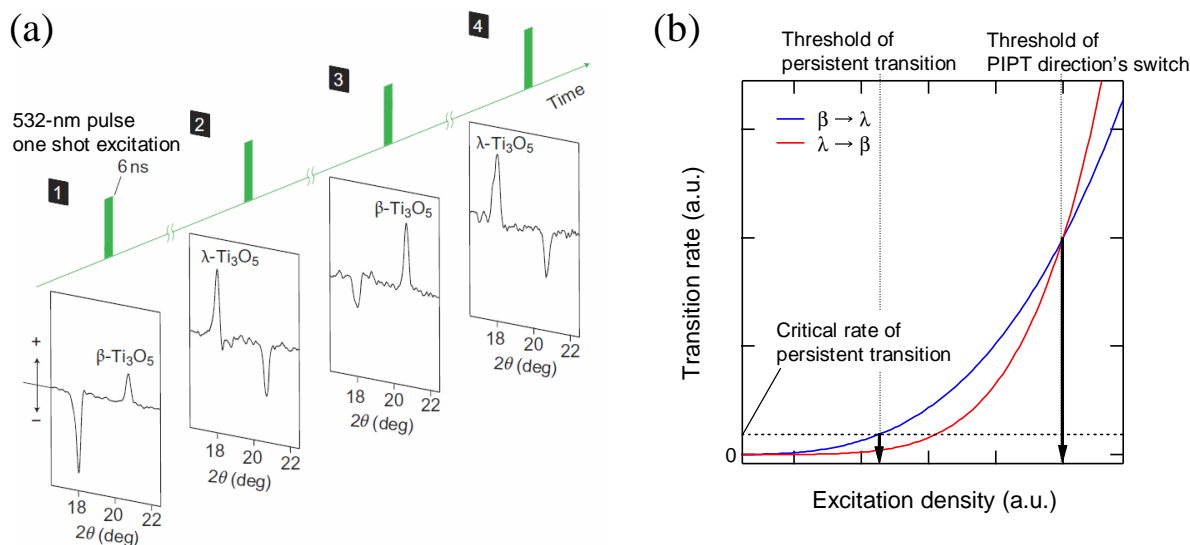
Fig. 5.6: (a) The difference XRD patterns obtained after irradiating with the green pulses (532 nm, 6 ns), showing the shot by shot phase switching between λ and β phases [106]. (b) Schematic image of the PIPT direction's switching by adjusting the excitation fluence. See the text for explanation.

color of the irradiated area changes between black (λ phase) and brown (β phase) as shown in Fig. 5.5(a). Figure 5.5(b) shows the absorption spectra (Kubelka-Munk function) of λ (red) and β phases (black). The spectrum of λ phase has large metallic absorption over ultraviolet and infrared wavelengths. On the other hand, the spectrum of β phase has smaller absorption in the visible range than that of λ phase, resulting in the brown color. In addition, from the spectrum of β phase, the optical band gap was estimated to be 0.13 eV, supporting the assignment of the β phase as a semiconductor.

This switching phenomenon was thermodynamically interpreted as a PIPT between the truly stable β phase and the metastable λ phase, which is a trapped state at a local energy minimum as shown in Fig. 5.3(a). The photo-created β phase at room temperature can be transferred to α phase by heating as shown in Fig. 5.3(b).

This photoinduced phase transition has the further unique characteristic that the direction of the transition can be controlled by simply adjusting the excitation fluence at a constant wavelength. The excitation density dependence are reported as shown in Fig. 5.5(c). In this experiment, one shot of 6-ns and 532-nm green pulses was used as the excitation light source, and mixture of λ- and β-Ti$_3$O$_5$ (2:1) was used as the sample. When the irradiation fluence passes the threshold located at 2.7×10^{-6} mJ μm^{-2}, the β phase is transferred to the λ phase.

Furthermore, when the λ phase is irradiated at a fluence several times larger than this threshold (at around 6.9×10^{-6} mJ μm^{-2}), the λ phase reverts to the β phase.

Furthermore, when the laser power was set close to the threshold of the PIPT from β to λ phases (7×10^{-6} mJ μm^{-2}), the phase was optically switched back and forth shot by shot, which was confirmed by the XRD measurement as shown in Fig. 5.6(a). From these experimental results, it is speculated that the transition rates from β to λ phases and λ to β phases are competing as shown in Fig. 5.6(b). In increasing the excitation fluence, when the transition rate from β to λ phases exceed the first threshold for the persistent transition, the PIPT from β to λ phases occurs. As the fluence is further increased, the transition rate from λ to β phases increases steeply and becomes higher than that of the inverse process at the second threshold, and then the PIPT direction switches.

This photoinduced phase switching was induced also by irradiation at wavelengths of 355 or 1064 nm [106]. Hence, the trigger of these PIPTs were attributed to the excitation of the broad $3d$-$3d$ transition in Ti ions. The PIPT from λ to β phases was expected to be non-thermal process, because the direction of this transition corresponds to the high temperature to low temperature phases. On the other hand, the PIPT from β to λ phases could be induced not only by the ns pulse excitation, but also by continuous wave (CW) light irradiation (410 nm, 8×10^{-3} mW μm^{-2}) [106] as shown in Fig. 5.3(b). Since the sample surface was highly heated by the CW light irradiation, photo-thermal effect may contribute to the transition. However, the thermal and non-thermal contributions cannot be distinguished from such measurements in long time scales. Therefore, ultrafast spectroscopy is required to reveal it.

5.3   Objective of this research

In nano-granular Ti_3O_5, basic physical properties have not been obtained sufficiently, because this material was developed very recently. Since this material shows metal-semiconductor transitions, information on conductivity is important; THz conductivity is especially important, because the conductivity in nanoparticles is well characterized in the THz frequency range. Then, our first objective of this research is to investigate the THz optical conductivity in nano-granular Ti_3O_5 (Chapter 6).

In addition, the fluence-dependent reversible photoinduced phase switching is interesting in this material. However, its detailed mechanism remains unclear. In order to understand such

complicated phenomena, their relaxation dynamics following the optical stimulation has to be studied. Based on the background, our second objective is to investigate the PIPT through time-resolved measurements including ultrafast time scale, and to understand its mechanism by characterizing the relaxation processes (Chapter 7).

Chapter 6

THz Optical Conductivity Measurement

In this chapter, the THz optical conductivity in nano-granular Ti_3O_5 is investigated by THz time domain spectroscopy (THz-TDS). This information is important because Ti_3O_5 shows metal-semiconductor transition, and because the conductivity characteristics in nanoparticles are well reflected in the THz frequency range. In order to understand its conductive characteristics, the obtained THz optical conductivity is analyzed by the Drude-Smith model, which is an extended Drude model characterizing conductivity in nanoparticles.

6.1   THz time domain spectroscopy

A terahertz (THz) wave is the electromagnetic wave having a frequency between 100 GHz $\sim$ 10 THz (30 μm $\sim$ 3 mm in wavelength), which is located at the middle of the light and radio wave frequencies. Since there are a number of molecular oscillations (or phonons) inherent to the materials, we can use the THz spectroscopy to identify the molecular species and their structural states [123, 124]. Moreover, THz waves are sensitive to free electrons (Drude electrons), indicating that THz spectroscopy is useful to characterize conductive materials or metal-nonmetal phase transitions [125]. In our research, this advantage was utilized to study the conductivity properties of nano-granular Ti_3O_5.

THz time domain spectroscopy (THz-TDS) is one of the most excellent methods to measure the optical responses in the THz frequency range. Since this method employs a femtosecond pulse laser, extremely high brightness overwhelming the thermal radiation at room temperature can be achieved. Therefore, thermal noise can be neglected, and very high signal to noise
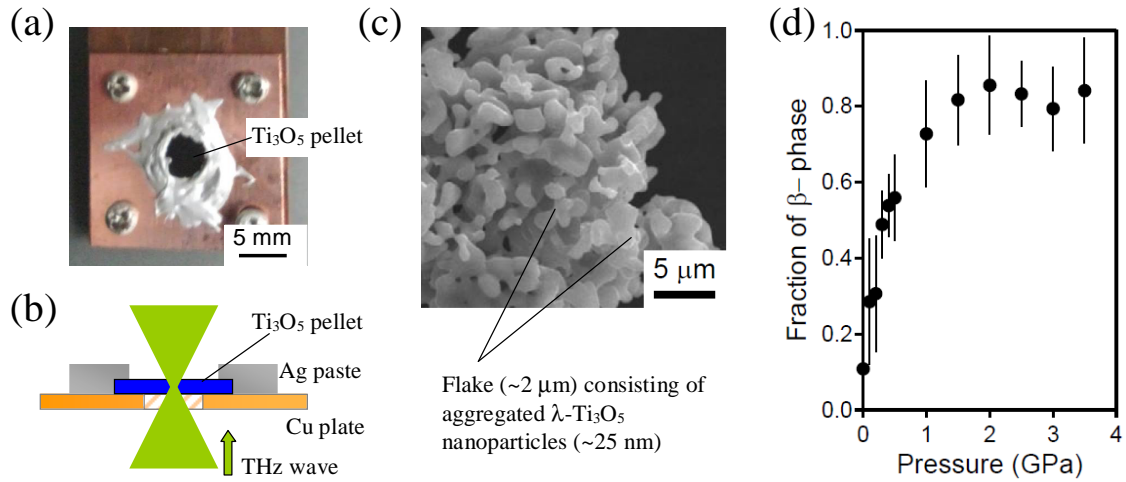
Fig. 6.1: (a) A pellet sample consisting of λ-Ti$_3$O$_5$ nanoparticles adhered on a copper plate. (b) The cross section of the mounted Ti$_3$O$_5$ pellet sample. (c) SEM image of flake-typed λ-Ti$_3$O$_5$ nanoparticles [106]. (d) The converted β phase fraction dependence on the applied pressure [106].

ratio can be achieved. Furthermore, time-resolved experiment is possible by pump-probe measurement. In THz-TDS, the THz waveform transmitted (or reflected) through the material is measured. The optical constants of the sample, such as dielectric constant ϵ, refractive index n, and optical conductivity σ, are deduced from the Fourier transformation spectrum of the transmitted (or reflected) THz waveform. The obtained data contains information not only about the amplitude but also about the phase. Thus, the real and imaginary parts of the optical constants can be obtained simultaneously without Kramers-Kronig transformation. These are the most prominent advantages in THz-TDS.

6.2 Experiment

The sample preparation processes and the experimental setup of THz-TDS are given below.

6.2.1 Sample preparation

Synthesis of nano-granular λ-Ti$_3$O$_5$

Nano-granular Ti$_3$O$_5$ has been synthesized as two types of forms [106–108]: (i) λ-Ti$_3$O$_5$ nanoparticles in SiO$_2$ matrix by using a combination of reverse-micelle and sol-gel techniques,

and (ii) flake-formed λ-Ti_3O_5 nanoparticles by calcinating anatase TiO_2 under hydrogen atmosphere at 1200 °C. Here, (ii) the flake-formed λ-Ti_3O_5 nanoparticles were used in our experiment[1]. The flake (2 ± 0.5 μm) consisting of aggregated λ-Ti_3O_5 nanoparticles (25 ± 15 nm) as shown in the SEM (Scanning Electron Microscope) image in Fig. 6.1(c).

Preparation of pellet samples

λ-Ti_3O_5 pellet sample was prepared by pressing the flake-formed λ-Ti_3O_5 nanoparticles. The compressing pressure was set at 0.2 GPa, and was applied to the sample in a very short time, because λ phase is rapidly transferred to β phase by applying pressure higher than ~0.3 GPa as shown in Fig. 6.1(d). The configuration of the pellet was confirmed by x-ray diffraction (XRD) measurement; though β-Ti_3O_5 phase was included approximately 20 %, the λ phase was dominant in the pellet. The dimensions of the pellet was 5 mm in diameter and 140 μm in thickness, and its filling ratio was estimated to be ~0.4 by evaluating its density.

β-Ti_3O_5 pellet sample was also prepared as follows. By applying sufficiently high pressure to flake-type λ-Ti_3O_5 nanoparticles, they were converted to β-Ti_3O_5. The almost complete conversion to β phase was confirmed by examining XRD pattern. The β-Ti_3O_5 nanoparticles were pressed at 0.2 GPa, and a pellet was prepared. The pellet was 5 mm in diameter and 170 μm in thickness, and its filling ratio was estimated to be ~0.4.

These pellets were adhered on a 1-mm thick copper plate having a 3-mm hole with conductive silver paste as shown in Figs. 6.1(a) and 6.1(b). This sample unit was mounted on a cryostat, and its transmission spectrum was measured by the THz-TDS system.

6.2.2   Experimental setup of THz-TDS

For the THz-TDS measurement, a typical experimental system using THz antennas was employed. The experimental setup is shown in Fig. 6.2(a). The mode-locked Ti:sapphire laser was employed as a light source, producing 12-fs pulses at 800 nm with a repetition rate of 75 MHz. The output was divided into pump and probe pulses by the beamsplitter. The pump pulses were focused on the THz emitter, which is a photoconductive dipole antenna fabricated on a low-temperature-grown GaAs with a Si hemispherical lens. 20-V rectangular ac electric field was applied to the gap of the antenna with a frequency of 50 kHz by the function generator.

---

[1]All the nano-granular Ti_3O_5 samples measured in this thesis were synthesized by our collaborators H. Tokoro and S. Ohkoshi at the Univ. of Tokyo.
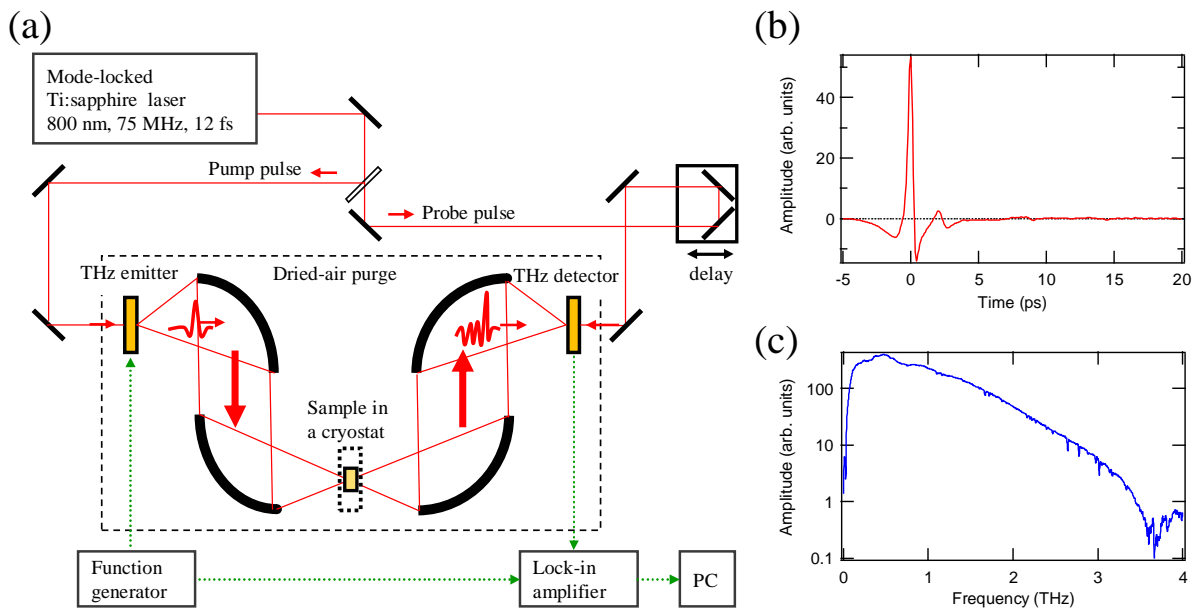
Fig. 6.2: (a) Schematic of the experimental setup of THz-TDS. See the text for explanation. (b) THz waveform without any sample. (c) THz spectrum obtained by applying Fourier transformation to the THz waveform shown in (b).

The photo-generated carriers in the emitter were driven by the external electric field, and THz wave was emitted in accordance with the derivative of the time-dependent current. The area where THz wave was propagating was purged by dried air in order to prevent absorption due to water molecules. The emitted THz wave was focused on the sample in the cryostat by the off-axis parabolic mirrors. The transmitted THz wave was focused on another photoconductive dipole antenna which works as a THz detector. By focusing the probe pulses on the same spot from behind, the electric field intensity of the THz wave was measured by lock-in detection method. The THz waveform was measured by changing the time delay of the probe pulses. The optical properties of the sample were obtained by taking the ratio of the measured THz waveforms with and without the sample.

Figure 6.2(b) shows the THz waveform obtained without any sample. It has a duration of about 1 ps, and is nearly mono-cycle THz pulse. The THz spectrum was obtained as shown in Fig. 6.2(c) by applying Fourier transformation to the THz waveform. High signal to noise (S/N) ratio was achieved in 0.2 ~ 2.0 THz; hereafter, the THz conductivity was evaluated in this frequency range.
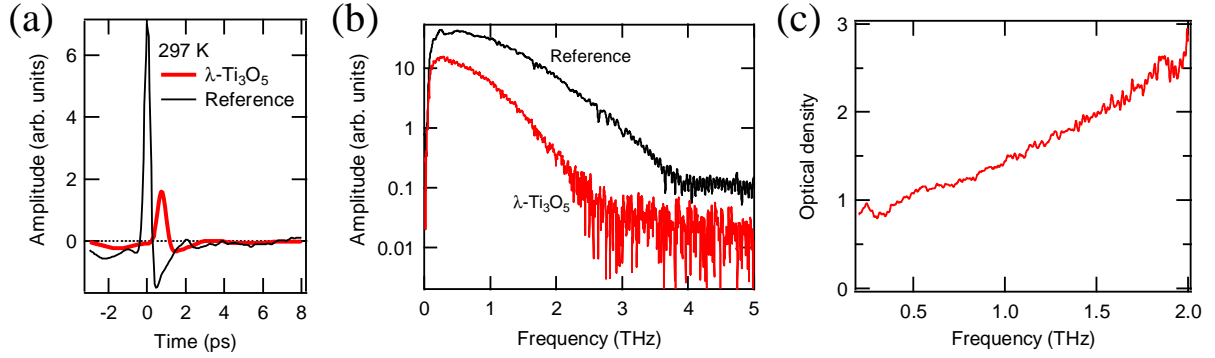
Fig. 6.3: (a) THz waveform with (red) and without (black) λ-Ti$_3$O$_5$ pellet. (b) THz spectra obtained by applying Fourier transformation to the THz waveform in (a). (c) Optical density of the λ-Ti$_3$O$_5$ pellet deduced from the spectra in (b).

6.3   Results and discussions

6.3.1   THz conductivity in λ-Ti$_3$O$_5$ at room temperature

Calculation of optical conductivity spectrum

Figure 6.3(a) shows the THz waveform transmitted through the λ-Ti$_3$O$_5$ pellet. The peak position was delayed for about 1 ps due to the refractive index of the sample, and the peak intensity decreased due to absorption and reflection loss at the sample. By applying Fourier transformation, the amplitude spectrum of the THz wave was obtained as shown in Fig. 6.3(b). From these spectra, the optical density spectrum was also obtained as shown in Fig. 6.3(c). The optical density increased monotonically with frequency.

From Fourier transformation of a THz waveform, not only amplitude spectrum $|\tilde{E}(\omega)|$ but also phase spectrum $\phi(\omega)$ can be obtained. Thus, the complex transmittance $\tilde{t}(\omega)$ can be obtained from the THz waveforms measured with and without the sample [126]. $\tilde{t}(\omega)$ is given by:

$$\tilde{t}(\omega) = \frac{\tilde{E}^{sam}}{\tilde{E}^{ref}} = \frac{|\tilde{E}^{sam}|}{|\tilde{E}^{ref}|} \exp[i(\phi^{sam} - \phi^{ref})], \tag{6.1}$$

where the superscript "sam" and "ref" means the signal with and without the sample respectively, and ω is the angular frequency. Assuming a thin sample, an expression for $\tilde{t}(\omega)$ including multi-reflection effect is given by:

$$\tilde{t}(\omega) = \tilde{t}_{in} \cdot \tilde{t}_{out} \cdot \exp\left(i\frac{(\tilde{n}-1)d}{c}\omega\right) \cdot \sum_j \left[\tilde{r}_{out} \cdot \exp\left(i\frac{\tilde{n}d}{c}\omega\right)\right]^{2j}, \tag{6.2}$$

83
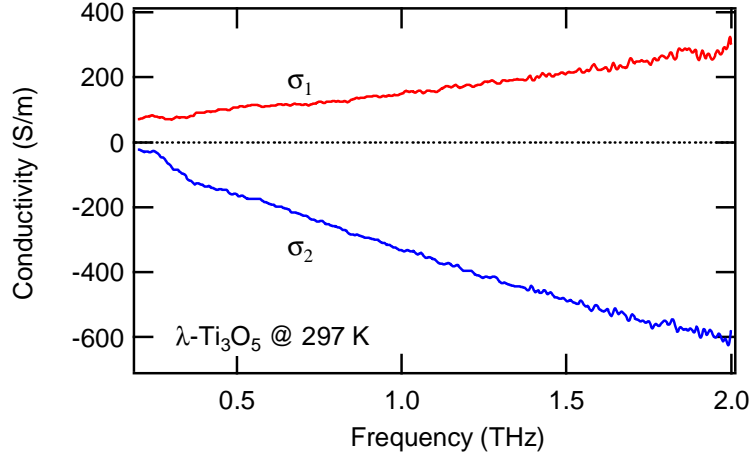
Fig. 6.4: THz optical conductivity spectrum deduced from the THz waveforms in Fig. 6.3(a).

where j is the number of times of multireflection ($j \geq 0$), $\tilde{n}(\omega) = n + i\kappa$ is the complex refractive index of the sample, d is the thickness of the sample, and c is the light speed. Here,

$$\tilde{t}_{in} = \frac{2}{\tilde{n} + 1}, \quad \tilde{t}_{out} = \frac{2\tilde{n}}{\tilde{n} + 1}, \quad \tilde{r}_{out} = \frac{\tilde{n} - 1}{\tilde{n} + 1}, \tag{6.3}$$

where the t (or r) with subscripts "in" and "out" denotes the complex transmittance $\tilde{t}$ (or complex reflectance $\tilde{r}$) when the electromagnetic wave goes "into" and "out of" the sample, respectively. Assuming infinity times reflection, Eq. 6.2 is rewritten as:

$$\tilde{t}(\omega) = \frac{4\tilde{n}}{(\tilde{n} + 1)^2} \exp\left(i\frac{(\tilde{n} - 1)d}{c}\omega\right)\left[1 - \left(\frac{\tilde{n} - 1}{\tilde{n} + 1}\right)^2 \exp\left(i\frac{2\tilde{n}d}{c}\omega\right)\right]^{-1}. \tag{6.4}$$

From these relations, the complex refractive index spectrum $\tilde{n}(\omega)$ can be self-consistently deduced. Complex refractive index $\tilde{n}$, complex dielectric constant $\tilde{\epsilon} = \epsilon_0(\epsilon_1 + i\epsilon_2)$, and complex optical conductivity $\tilde{\sigma} = \sigma_1 + i\sigma_2$ are connected with the following relations:

$$\epsilon_1 + i\epsilon_2 = n^2 - \kappa^2 + i(2n\kappa), \tag{6.5}$$

$$\sigma_1 + i\sigma_2 = \omega\epsilon_0[\epsilon_2 + i(1 - \epsilon_1)], \tag{6.6}$$

where ϵ_0 is the vacuum dielectric constant. By using these relations, the complex optical conductivity spectrum $\tilde{\sigma}(\omega)$ can be derived from the results of THz-TDS.

THz conductivity in λ-Ti$_3$O$_5$ at room temperature

Figure 6.4 shows the THz optical conductivity σ in λ-Ti$_3$O$_5$ at room temperature, which was deduced from the THz waveforms given in Fig. 6.3(a) through Eqs. (6.1)-(6.6). In the
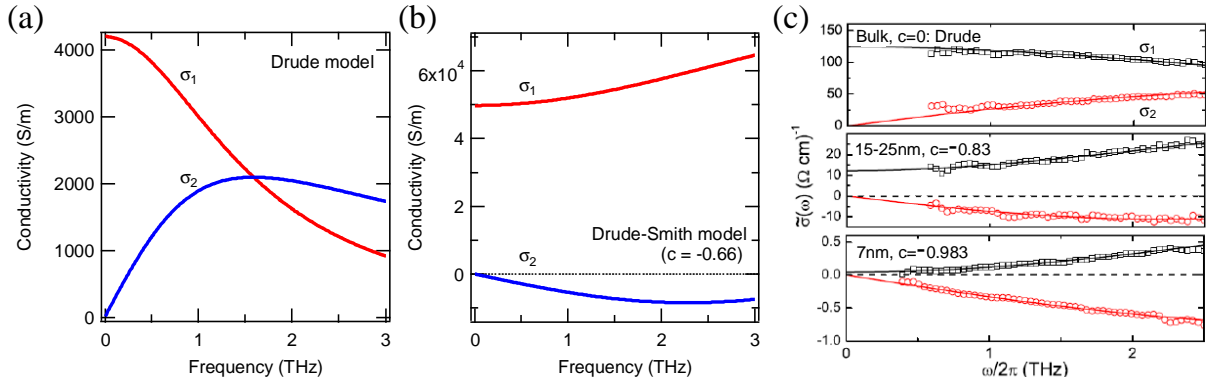
Fig. 6.5: (a) THz conductivity spectra calculated with the Drude model applying typical parameters in n-typed GaAs ($n = 1.0 \times 10^{23}$ m^{-3}, $\tau = 100$ fs, $m^* = 0.067\ m_e$ [128]). (b) Those calculated with the Drude-Smith model using typical parameters in VO$_2$ ($n = 5.2 \times 10^{26}$ m^{-3}, $\tau_{DS} = 20$ fs, $m^* = 2\ m_e$, $c = -0.66$ [131]). (c) The experimental THz conductivity spectra in bulk Si (top panel), Si particles of 15-25 nm in diameter (center panel), and 7-nm Si particles (lower panel) [129]. These spectra were fitted by the Drude and Drude-Smith models.

frequency range 0.2 ~ 2.0 THz, the real part σ_1 increased monotonically with the frequency. The value of the conductivity was approximately 150 S m^{-1} at 1.0 THz. On the other hand, the imaginary part had a negative value and decreased with the frequency. The value at 1.0 THz was estimated to be about -330 S m^{-1}.

6.3.2 Analysis with the Drude-Smith model

The conductivity spectra shown in Fig. 6.4 are very different from those expected from the Drude model, which predicts increase of σ_1 and positive σ_2 at low frequency limit. As we will see in this section, the spectra resemble those predicted from the Drude-Smith model [127], which has been often observed in nanomaterials.

In this section, we initially review the conduction models proposed in the previous studies (Drude and Drude-Smith models). Then, we perform a fitting analysis for the obtained THz conductive spectra in nano-granular Ti$_3$O$_5$ with the Drude-Smith model.

Brief introduction to the Drude model

In general, the conductivity due to free electrons has been understood by some macroscopic conduction models [128][2]. The Drude model has been one of the most simplest and widely used conduction models, where carriers randomly collide with each other and lose their momenta with a rate of $\Gamma = 1/\tau$. Then, the response function $j(t)$ (or time-dependent current) is given by:

$$j(t)/j(0) = \exp(-t/\tau). \tag{6.7}$$

Taking Fourier transformation of $j(t)$, the optical conductivity $\tilde{\sigma}(\omega)$ in the Drude model is given by:

$$\tilde{\sigma}(\omega) = \int_0^\infty j(t) \exp(i\omega t) dt, \tag{6.8}$$

$$= \frac{nq^2}{m^*} \frac{\tau}{1 - i\omega\tau}, \tag{6.9}$$

where n is the electron density, q is the elementary charge, and m^* is the effective mass.

The typical conductivity spectra in n-typed GaAs ($n = 1.0 \times 10^{23}$ m^{-3}, $\tau = 100$ fs, $m^* = 0.067\, m_e$ [128]) are calculated with the Drude model as shown in Fig. 6.5(a). Here, both of real (σ_1) and imaginary (σ_2) parts have positive values. The σ_1 has a finite value at $\omega = 0$ and decreases monotonically with the frequency. One the other hand, The σ_2 is zero at $\omega = 0$ and has a maximum at $\omega = 1/\tau$. As an experimental example, the THz conductivity spectra in Si are shown in Fig. 6.5(c) [129]. The top panel in Fig. 6.5(c) shows the conductivity in bulk Si, which was well reproduced by the Drude model indeed.

Introduction to the Drude-Smith model

When the dimension of the material is reduced to nanoscopic scale, their conductive behavior drastically changes. As shown in the lower two panels of Fig. 6.5(c), when the size of the crystal became smaller than a few 10 nm, the spectrum drastically changes from that of the Drude model. In σ_1, its slope turns from negative to positive and its magnitude decreased, meaning decreased conductivity. In σ_2, its slope turns to negative and its value turns to negative. Similar conductive behaviors have been often observed in a variety of conductive nanomaterials [129–137].

---

[2]A review on conductivities in bulk and nanomaterial has been given by Hughes *et al.* [128]. Please refer to this article for more detail.

scatter

Grain boundary

reflect

e⁻

Conductive carriers lose their momentum with the probability of $1-|c_n|$
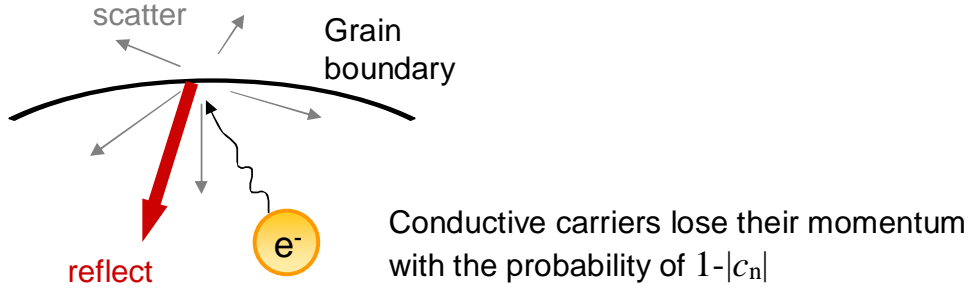
Fig. 6.6: Schematic image of the Drude-Smith conduction model. The conductive carriers after experiencing n times of collisions (for example, with the grain boundary) lose their momenta by being scattered isotropically with the probability of $1 - |c_n|$.

In order to understand such conductivity in conduction phenomena characteristic in nanomaterials, the Drude-Smith model has been well known as one of the most useful models [127]. This is an extended Drude model, where the reflection of carriers at the domain boundary is taken into account. In the Drude-Smith model, the carriers are assumed to experience collisions which obey the Poisson distribution; the probability $p_n(0, t)$ of n events in the time interval $(0, t)$ is given by:

$$p_n(0, t) = (t/\tau)^n \exp(-t/\tau)/n!. \tag{6.10}$$

From this relation, the response function $j_{DS}(t)$ is given by:

$$j_{DS}(t)/j_{DS}(0) = \exp(-t/\tau)\left[1 + \sum_{n=1}^{\infty} c_n(t/\tau)^n/n!\right], \tag{6.11}$$

and accordingly the conductivity is given by:

$$\tilde{\sigma}_{DS}(\omega) = \frac{nq^2\tau_{DS}/m^*}{1 - i\omega\tau_{DS}}\left[1 + \sum_{n=1}^{\infty} \frac{c_n}{(1 - i\omega\tau_{DS})^n}\right]. \tag{6.12}$$

Here, c_n ($0 \geq c \geq -1$) represents the anisotropy of the nth scattering process. In other words, the carriers after experiencing n times of collisions lose their momenta by being scattered isotropically with the probability of $1 - |c_n|$ as shown in Fig. 6.6. Eq. (6.12) is the general formula of the Drude-Smith conductivity.

In analyzing the THz conductivity spectra in nanomaterials by using this model, an approximation $c_n|_{n\geq2} = 0$ is adopted, meaning that only the first collision is taken into account. Then, the conductivity is given by:

$$\tilde{\sigma}_{DS}(\omega) = \frac{nq^2\tau_{DS}/m^*}{1 - i\omega\tau_{DS}}\left(1 + \frac{c}{1 - i\omega\tau_{DS}}\right), \tag{6.13}$$

where c_1 is rewritten by c. This is the most often used Drude-Smith formula in practice. There are three free parameters in this model: electron density $n/(m^*/m_e)$, the Drude-Smith time constant τ_{DS}, and a c parameter. Here, $n/(m^*/m_e)$ only varies the spectral magnitude. Thus, the parameters characterizing the spectral shapes are the residual two parameters, τ_{DS} and c.

The typical Drude-Smith conductivity spectra in nano-granular VO_2 ($n = 5.2 \times 10^{26}$ m^{-3}, $\tau_{DS} = 20$ fs, $m^* = 2\, m_e$, $c = -0.66$ [131]) are calculated as shown in Fig. 6.5(b). These spectra indeed reflect the features generally observed in the conductivity in nanomaterials mentioned above. In the lower two panels of Fig. 6.5(c), the spectra are well reproduced with the Drude-Smith model.

Actually, the Drude-Smith model is somewhat phenomenological and there are some criticisms for it. However, it is the fact that it has successfully reproduced the conductive characteristics in a variety of nanomaterials [129–137]. An interpretation for the physical meaning of this model has been given by Němec *et al.* [138], although it is still somewhat controversial [139]. They calculated the carrier dynamics in a nanocrystal by a Monte-Carlo simulation, and showed the relations between the parameters used in the Drude-Smith model (τ_{DS} and c) and physically meaningful parameters. From this simulation, it is indicated that τ_{DS} well follows the Matthiessen's rule:

$$\frac{1}{\tau_{DS}} = \frac{1}{\tau_b} + \frac{1}{d/2v}, \tag{6.14}$$

where τ_b is the scattering rate in the bulk particle, v is the velocity of the carrier, and d is the diameter of the particle; $d/2v$ corresponds to the averaged time which carriers take to reach the particle surface. This relation means that $1/\tau_{DS}$ can be regarded as the sum of the scattering rates in the particle and at its surface. In addition, as for the c parameter, the following relation was empirically given by:

$$c = p_r \left(1 + \frac{1}{10} \cdot \frac{d/2v}{\tau}\right)^{-1}, \tag{6.15}$$

where p_r denotes the probability of the carriers' backscattering at the particle surface. The factor of 10 in Eq. (6.15) was obtained from the Monte-Carlo simulation. Here, the most noticeable point is that c strongly relates to the carrier reflection at the boundary, indicating c represents the strength of carrier localization. When c is closer to -1, the carriers are more strongly trapped in the nanoparticles, and vise versa. When c is 0, Eq. (6.13) is identical to the formula of the ordinary Drude model, Eq. (6.9).
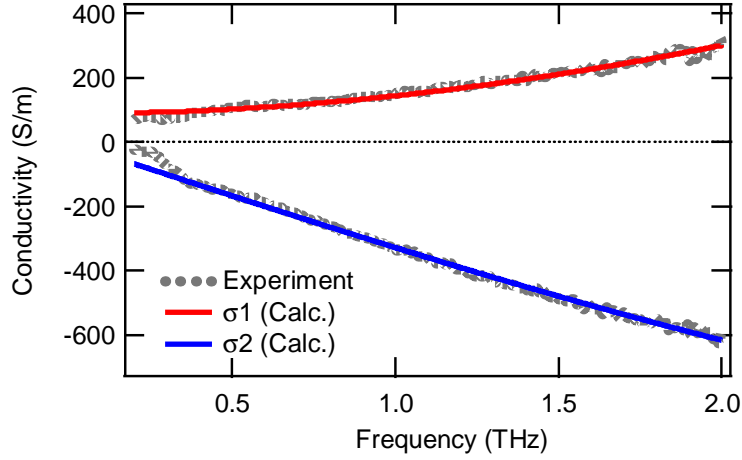
Fig. 6.7: Fitting analysis of THz optical conductivity spectrum. The solid lines, real part σ_1 (red) and imaginary part σ_2 (blue) of optical conductivity, were calculated with the Drude-Smith model. They were compared with the experimental results shown in Fig. 6.4 (gray dots).

Fitting analysis of THz conductivity in λ-Ti$_3$O$_5$ with the Drude-Smith model

The THz conductivity spectra of the nano-granular λ-Ti$_3$O$_5$ at room temperature shown in Fig. 6.4 was fitted by the Drude-Smith model. Figure 6.7 shows the result of the fitting analysis, wherein these spectra were successfully reproduced with high accuracy. From this analysis, the three fitting parameters were obtained: $n/(m^*/m_e) = 1.1 \times 10^{25}$ m^{-3}, $\tau_{DS} = 13$ fs, and $c = $ -0.979.

As for $n/(m^*/m_e)$, the effective mass m^* of λ-Ti$_3$O$_5$ has not been reported yet. However, m^* of α-Ti$_3$O$_5$ was given to be approximately $20m_e$ by Keys et $al.$ [140]. Since α-Ti$_3$O$_5$ has the similar electronic configurations as λ-Ti$_3$O$_5$, here we assumed that the m^* of λ-Ti$_3$O$_5$ has the similar value to that of α-Ti$_3$O$_5$. Then, if the assumed m^* and the filling ratio of ~0.4 are taken into account, n in the λ-Ti$_3$O$_5$ can be estimated to be 5.5×10^{26} m^{-3}. This amount was two orders of magnitude smaller than that observed in typical metals.

As for the obtained c parameter, its value of -0.979 was rather close to -1. This fact indicates that the carriers were very strongly localized in the nanoparticles. The conductivity in λ-Ti$_3$O$_5$ is relatively low compared with typical metals. One of the reasons of this low conductivity can be attributed to the strong carrier localization confirmed from the present THz measurement. Since the λ phase can exist only in the form of nanopariticles, this conductivity characteristic is essential in λ-Ti$_3$O$_5$.
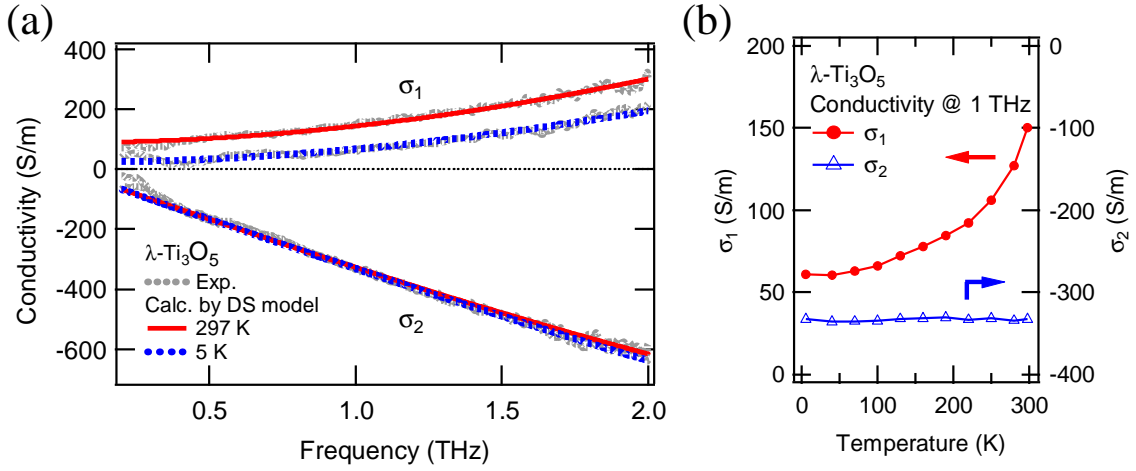
Fig. 6.8: (a) THz conductivity spectra at 297 and 5 K. The experimental results (gray broken line) are fitted by the Drude-Smith model (red solid line: 297 K, blue broken line: 5 K). (b) Temperature dependences of σ_1 and σ_2 at 1.0 THz.
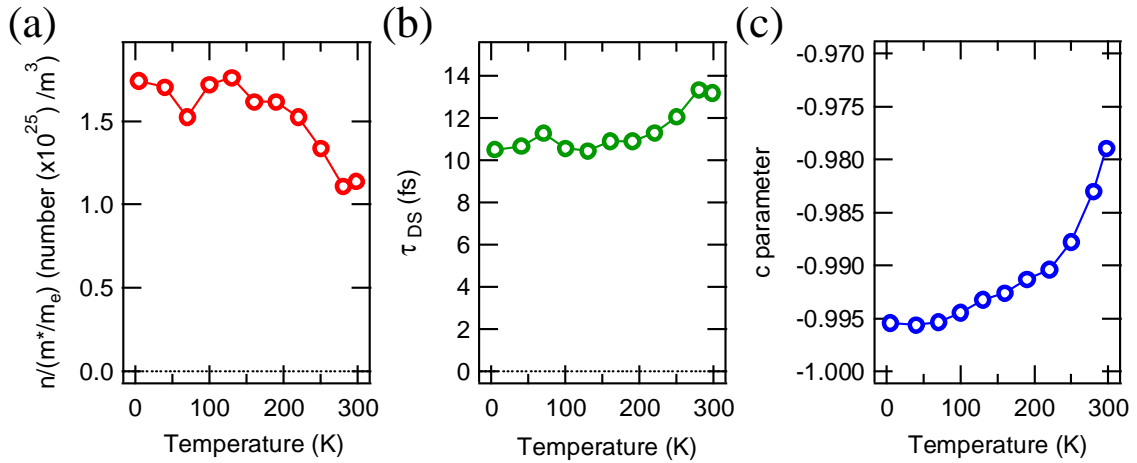
Fig. 6.9: The temperature dependences of the parameters obtained from the Drude-Smith fitting analysis: (a) electron density $n/(m^*/m_e)$, (b) τ_{DS}, and (c) c.

6.3.3 Temperature dependence of THz conductivity in λ-Ti$_3$O$_5$

The temperature dependence of the THz conductivity in λ-Ti$_3$O$_5$ was also investigated. Figure 6.8(a) shows the THz conductivity spectra at 297 and 5 K, and Fig. 6.8(b) shows the temperature dependences of σ_1 and σ_2 at 1.0 THz. From these results, it is found that the σ_1 decreased exponentially upon cooling, while σ_2 was nearly constant. From 297 to 5 K, the σ_1 decreased by about 60 %, which indicates the insulating of the sample at low temperatures.

By fitting with the Drude-Smith model, all the temperature-dependent spectra were well

reproduced. The fitting results at 297 and 5 K are shown in Fig. 6.8(a). The temperature dependences of the fitting parameters were obtained from this analysis. Figure 6.9 shows (a) the electron density $n/(m^*/m_e)$, (b) τ_{DS}, and (c) c, respectively.

The most notable change here is the decrease of the c parameter upon cooling in Fig. 6.9(c), because it can be assigned to the main factor to lower the σ_1. As it was described above, the c is deeply related to the reflection rate at the surface of the nanocrystal. Therefore, the reason for the decrease of the conductivity at low temperatures can be assigned to the enhanced carrier localization in the nanocrystals. It is indicated that this phenomenon corresponds to the suppression of the hopping conductivity between nanoparicles within the individual particles.

The τ_{DS} became slightly faster from 13 to 10 fs by cooling as found in Fig. 6.9(b). As described above, τ_{DS} is expressed as Eq. (6.14). In general, τ_b becomes longer at low temperatures because phonon scattering is suppressed. Therefore, the shorter τ_{DS} at low temperatures observed in Fig. 6.9(b) can be attributed to the increase of the collision rate to the domain boundary.

In Fig. 6.9(a), upon cooling, the electron density increased by about 50 %. However, such phenomenon cannot be normally expected, and it is rather expected to be nearly constant against temperature, because λ-Ti$_3$O$_5$ is in the metallic phase. This peculiarity is tentatively attributed to the artifact due to the c parameter too close to -1. When c approaches toward -1, the fitting result of the electron density n starts to diverge, and the first-order approximation of the Drude-Smith model assumed in Eq. (6.13) can be getting failed[3]. As explained in Sec. 6.3.2, the c close to -1 corresponds to the high backscattering probability of the carriers at the domain boundary. Therefore, this fail of the first-order approximation indicates that the assumption that the carriers lost their momenta after the first backscattering event gets failed because of the high reflectivity. For getting more precise description in such a strongly carrier-localized material, the conduction model should be improved to include the effect of the c_n in higher orders, meaning the multi-reflection of the carriers at the domain boundary. This point is the future problem of this research.

To summarize, from the analysis discussed above, the noticeable insights have been obtained that the carrier localization plays an important role in the THz conductivity in λ-Ti$_3$O$_5$, and that the localization is enhanced at low temperatures, resulting in the decrease of the

---

[3]Here, it should be noted that the quantitative accuracy of the fitting parameters in the lower temperatures cannot be ensured because of the failure of the first-order approximation, however, the qualitative result is probably correct that the strong carrier localization dominates the THz conductivity in λ-Ti$_3$O$_5$ nanoparticles.
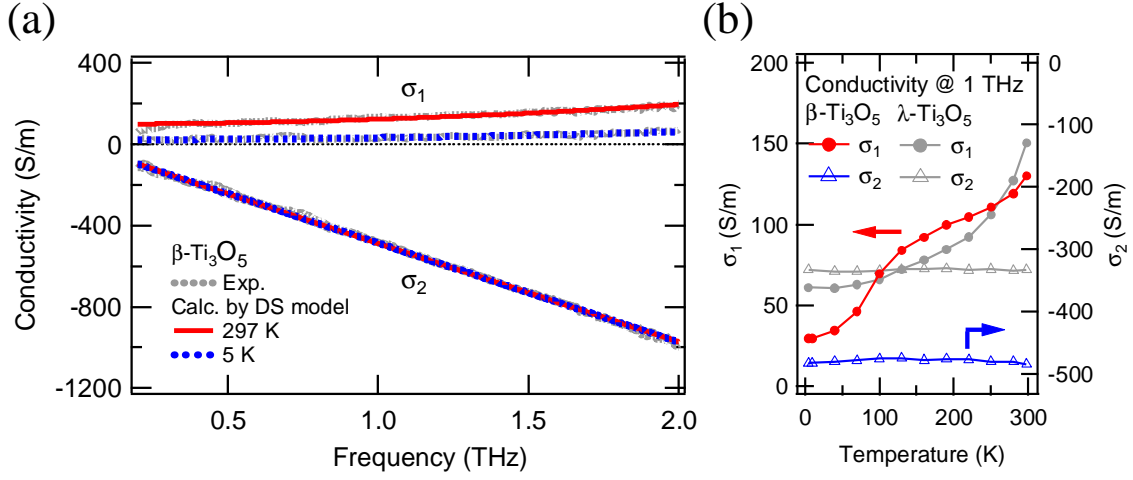
Fig. 6.10: (a) THz conductivity spectra at 297 and 5 K in β-Ti$_3$O$_5$. The experimental results (gray broken line) are fitted by the Drude-Smith model (red solid line: 297 K, blue broken line: 5 K). (b) Temperature dependences of σ_1 (red) and σ_2 (blue) at 1.0 THz. Those of λ-Ti$_3$O$_5$ shown in Fig. 6.8(b) are replotted with light-gray points for comparison.

conductivity. These physical pictures should be qualitatively correct. However, the conduction model should be improved for performing more precise characterization.

6.3.4   THz conductivity in β-Ti$_3$O$_5$

Temperature dependence of THz conductivity in β-Ti$_3$O$_5$

The THz conductivity in β-Ti$_3$O$_5$ was investigated as well as in λ-Ti$_3$O$_5$. Figure 6.10(a) shows the optical conductivity spectra of β-Ti$_3$O$_5$ at 297 and 5 K obtained by the same procedure as in the case of λ-Ti$_3$O$_5$. In the spectra, the σ_1 was positive and had the positive slope against the frequency, while the σ_2 was negative and had the steep negative slope. When the sample was cooled down, the σ_1 decreased, while the σ_2 was nearly constant. These features are similar to those in the conductivity spectra of λ-Ti$_3$O$_5$ shown in Fig. 6.8.

In Fig. 6.10(b), the temperature dependences of the σ_1 and σ_2 at 1.0 THz in β-Ti$_3$O$_5$ are plotted, and those obtained in λ-Ti$_3$O$_5$ are replotted behind them for comparison (Hereafter σ_i in β- (λ-) Ti$_3$O$_5$ is called as σ_i^β (σ_i^λ) for simplicity). First, as for σ_1, the σ_1^β at 297 K was 130 S m^{-1}, which was lower than the σ_1^λ of 150 S m^{-1}[4]. The σ_1^β gradually decreased by

---

[4]σ_1^β and σ_1^λ were estimated in the same order, though β phase is semiconductor and λ phase is metal. It is probably because the hopping conduction between shallow impurity levels dominates in β at high temperatures, and because the effective mass in β phase is smaller than that in λ phase ($m_\beta^* = 4.4\ m_e$ and $m_\lambda^* = 20\ m_e$ [140]).

92
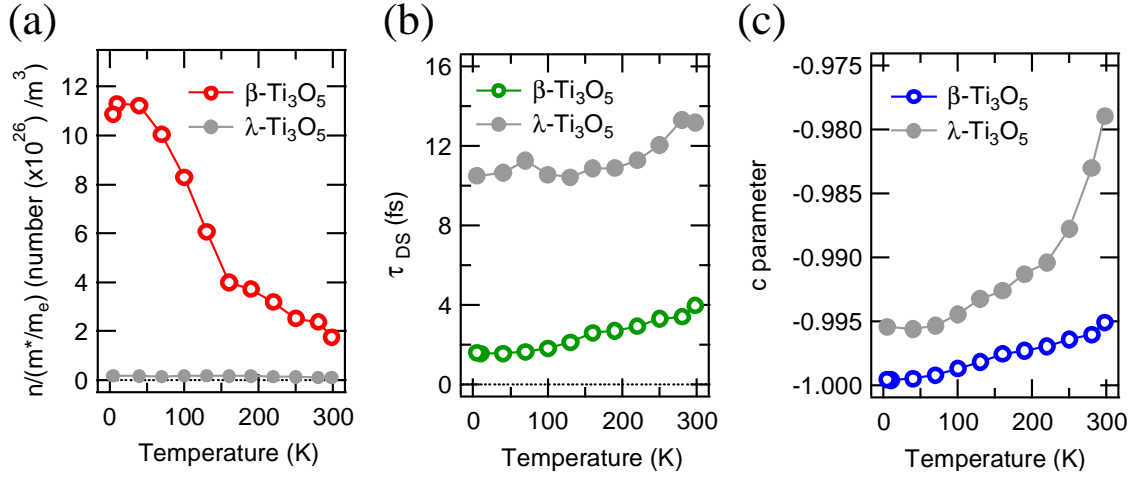
Fig. 6.11: The temperature dependences of the fitting parameters obtained in β-Ti_3O_5: (a) electron density $n/(m^*/m_e)$, (b) τ_{DS}, and (c) c parameter. The parameters of λ-Ti_3O_5 shown in Figs. 6.9(a)-(c) are replotted with the light-gray points for comparison.

cooling from 300 K. This insulating behavior is ascribed to carrier localization as it will be described later. Around 100 K, σ_1^β steeply further decreased. This steep conductivity decrease in the semiconductor β phase is probably assigned to the suppression of the thermally activated hopping conduction between shallow impurity levels. At 5 K, σ_1^β was 30 S m^{-1} and was about a half of σ_1^λ of 60 S m^{-1}. Second, as for σ_2, σ_2^β did not show any temperature dependence as indicated from the spectrum in Fig. 6.10(a). The value of σ_2^β was -490 S m^{-1} at 297 K and was lower than that of σ_2^λ of -330 S m^{-1}.

Analysis of THz conductivity in β-Ti_3O_5 with the Drude-Smith model

The THz conductivity spectra in β-Ti_3O_5 were fitted with the Drude-Smith model as in the case of λ-Ti_3O_5. The fitting results at 297 and 5 K are shown in Fig. 6.10(a). All the temperature-dependent spectra of β-Ti_3O_5 were successfully fitted by this model. Figures 6.11(a)-(c) show the estimated fitting parameters, (a) electron density $n/(m^*/m_e)$, (b) the Drude-Smith time constant τ_{DS}, and (c) c parameter.

At 297 K, the parameters were evaluated as follows, $n/(m^*/m_e)$: 1.8×10^{26} m^{-3}, τ_{DS}: 4 fs, c parameter: -0.995. Here, the value of c was closer to -1 than that in λ-Ti_3O_5 of -0.979, indicating that the stronger carrier localization occurs in β-Ti_3O_5 than in λ-Ti_3O_5. In addition, the τ_{DS} of 4 fs was faster than that in λ-Ti_3O_5 of 13 fs, indicating the backscattering of carriers at the particle surface rather contributes to the conductivity in β-Ti_3O_5 more than in λ-Ti_3O_5.

Upon cooling, the values of c and τ_{DS} monotonically decreased to -0.999 and 2 fs, respectively, indicating that by cooling the sample, the carriers are more strongly localized in nanoparticles, just like in the case of λ-Ti$_3$O$_5$. These indications involving the carrier localization are the most noticeable results obtained from this Drude-Smith fitting analysis.

As for the electron density, unfortunately, only unreasonable results could be obtained with this analysis . The effective mass in β-Ti$_3$O$_5$ was given to be $m^* = 4.4\ m_e$ by Keys $et\ al.$ [140]. Thus, if the m^* and the filling ratio of $\sim$0.4 are taken into account, n in the β-Ti$_3$O$_5$ is estimated to be 2.0×10^{27} m^{-3}. This value is far larger than that of 5.5×10^{26} m^{-3} in the metallic λ phase, which is not natural. Moreover, against our expectation, n increased upon cooling, which is explicitly unphysical. We speculate that this peculiar divergence of n is attributed to the c parameter too close to -1, which is the same reason as that for the fail that the n in λ-Ti$_3$O$_5$ at low temperatures could not be accurately characterized in Sec. 6.3.3. Thus, for more quantitative characterization including the precise estimation of the electron density, the conduction model should be improved to include the contribution of the multi-reflection of the carriers at the domain boundary.

6.4   Summary

In conclusion, the THz optical conductivity in nano-granular Ti$_3$O$_5$ was measured by THz-TDS and analyzed with the Drude-Smith model. The THz conductivity spectra in both of λ and β phases were successfully obtained at various temperatures from 297 to 5 K. The temperature dependences of the conductivity in λ and β phases are different from each other, and had metallic and semiconductor-like characteristics, respectively. Since the spectral shapes reflected the conductive characteristics often observed in nanomaterials, these spectra were analyzed with the Drude-Smith model where carrier backscattering at the grain boundary is taken into account. By this fitting analysis, all the obtained spectra were well reproduced, and the fitting parameters were evaluated: for example at 297 K in λ-Ti$_3$O$_5$, electron density $n = 5.5 \times 10^{26}$ m^{-3}, the Drude-Smith time constant $\tau_{DS} = 13$ fs, and c parameter = -0.979, and in β-Ti$_3$O$_5$, $n = 2.0 \times 10^{27}$ m^{-3}, $\tau_{DS} = 4$ fs, c = -0.995.

From the discussion about c and τ_{DS}, it was indicated that the carrier localization in nanocrystals plays an important role in the THz conductivity of nano-granular Ti$_3$O$_5$. The conductivity in λ-Ti$_3$O$_5$ is relatively low compared with typical metals; one of the reasons of

this low conductivity was attributed to the strong carrier localization. The evaluated localization was stronger in β-Ti_3O_5 than in λ-Ti_3O_5. In addition, it was found that the carrier localization is enhanced (or hopping conduction is suppressed) by cooling, resulting in the decrease of the conductivity (insulating).

On the other hand, the electron density n could not be precisely characterized; it was estimated to be unphysical value. The reason was attributed to the failure of the first-order approximation in the Drude-Smith model occurred when c becomes too close to -1. Thus, for more quantitative characterization, the conduction model should be improved; for example, c_n in the higher orders (multi-reflection of the carriers at the domain boundary) should be involved. This is a future problem of this research.

Chapter 7

Time-resolved Diffuse Reflection Spectroscopy

In this chapter, the PIPT dynamics in nano-granular Ti_3O_5 is discussed[1]. First, the dynamics of the semiconductor-to-metal transition (β-Ti_3O_5 $\rightarrow$ λ-Ti_3O_5) was characterized in detail. With time-resolved diffuse reflection spectroscopy conducted over a wide range of time scales, from femtoseconds to microseconds, the entire transient behavior was investigated. In addition, the inverse process (λ-Ti_3O_5 $\rightarrow$ β-Ti_3O_5) was investigated with the same experimental setup.

7.1   Diffuse reflection spectroscopy

In order to observe the PIPT dynamics in nano-granular Ti_3O_5, diffuse reflection spectroscopy was used in this experiment. When nanoparticles are irradiated with light, the incident light is reflected in various directions due to the inhomogeneity of the form of the particles. Herein, a part of the diffused light experiences transmission through the particles, and its intensity is attenuated. Therefore, the diffuse reflection spectrum is very similar to the transmission spectrum; the absorption peaks are observed at the same wavelength in both spectra.

Actually, these spectra differ at the point that the intensity of relatively weak absorption peaks are observed higher in the diffuse reflection spectrum. In order to compare these spectra

---

[1]The main results discussed in this chapter are summarized in our research paper, Ref. [141].

quantitatively, the Kubelka-Munk transformation has been often used [122]:

$$f_{K.M.}(R) = \frac{(1-R)^2}{2R},\qquad(7.1)$$

where, $f_{K.M.}$ is the Kubelka-Munk formula, and R is the diffuse reflectance (DR). With this formula, the DR spectrum obtained in experiments can be transformed to f which is regarded as the absorption spectrum.

7.2 Experiments

7.2.1 Sample preparation

We prepared a pellet of β-Ti_3O_5 with diameter 6 mm and thickness ~1 mm. The β-Ti_3O_5 powder was prepared via a pressure-induced phase transition from λ-Ti_3O_5 flakes consisting of aggregated nanoparticles (25 ± 15 nm), synthesized by sintering anatase-TiO_2 particles in a hydrogen atmosphere [106]. The pellets' conversion to β-Ti_3O_5 was confirmed by examining the X-ray diffraction pattern. The preparation processes of this β-Ti_3O_5 pellet are the same as those mentioned in Sec. 6.2.1.

In studying the PIPT from β to λ phases, this β-Ti_3O_5 pellet was used as it was. On the other hand, in studying the inverse process (λ to β phases), the initial state was prepared by light irradiation as will be detailed in Sec. 7.3.3.

7.2.2 Setup of time-resolved DR spectroscopy

In order to investigate the PIPT dynamics, we performed two types of time-resolved diffuse reflection measurements with visible light. First, to observe the dynamics between 100 fs and 1 ns, we applied a femtosecond pump-probe measurement, whose setup is shown in Fig. 7.1(a). As a light source, we employed a 1 kHz regenerative amplifier (Spectra-Physics, Spitfire) seeded by a mode-locked Ti:sapphire laser (Spectra-Physics, TSUNAMI 3160C) producing 120 fs pulses at 800 nm. The output was separated into pump and probe light by a beam splitter. Pump pulses at 800 nm wavelength, which excite d-d transitions in titanium ions [106], were focused on the sample with a spot diameter of 300 μm. The wavelength of the probe pulses was converted by an optical parametric amplifier (Light Conversion, TOPAS-C), and these pulses

98
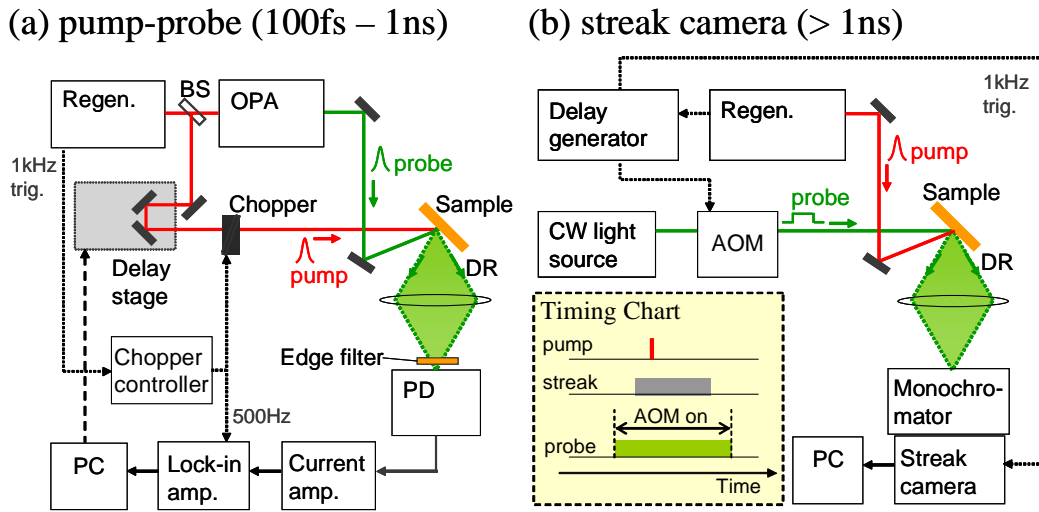
Fig. 7.1: Schematics of the experimental apparatus, (a) femtosecond pump-probe measurements (100 fs-1 ns) and (b) long duration measurement (>1 ns) with a streak camera. The inset shows a timing chart for the experiment. Regen.: Ti:sapphire regenerative amplifier system, OPA: optical parametric amplifier, BS: beam splitter, DR: diffuse reflection light, PD: Si photodetector, PC: personal computer, and AOM: acoustic optic modulator.

were focused on the sample with a spot diameter of 70 μm. Diffuse reflection of the probe light from the sample was collected by a photo-detector and recorded by a lock-in detection system.

Second, a streak camera (Hamamatsu Photonics, C5680), operated with a time resolution of about 0.7 ns, was employed to observe the dynamics longer than 1 ns, as shown in Fig. 7.1(b). The same femtosecond light source at 800 nm was used for pump pulses. As a probe, several semiconductor laser diodes emitting continuous waves were used depending on the probe wavelength. To avoid thermal damage to the sample, the probe light was switched on only in a short time window by an acoustic optic modulator (AOM) that was synchronized with the pump pulses.

The static diffuse reflection spectra were detected by a liquid-nitrogen-cooled charge-coupled device equipped with a monochromator, using a white halogen lamp as a light source. The reference spectrum was obtained with a white pellet consisting of $BaSO_4$ powder. All the above experiments were performed at room temperature.
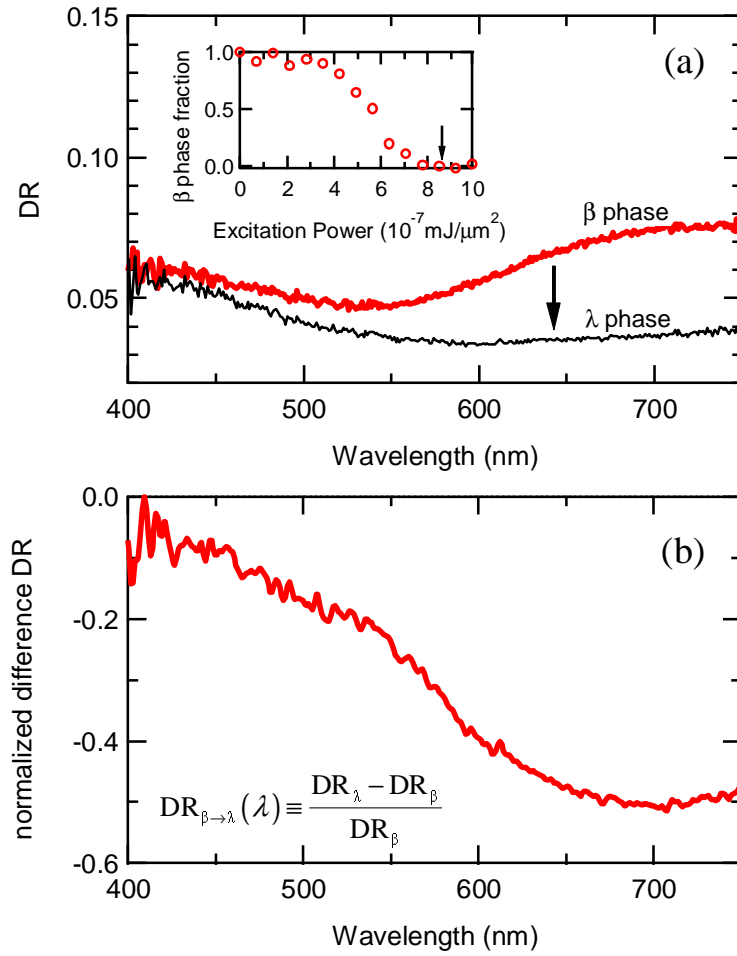
Fig. 7.2: (a) Diffuse reflectance (DR) spectra of β phase (red thick curve) and λ phase (black thin curve). The λ phase was created after irradiation with 5000 pulses (800 nm, 120 fs, 500 Hz, 8.5×10^{-7} mJ μm^{-2}); the power of these pulses is indicated by the arrow in the inset. The inset shows the fraction of the surviving β phase versus the excitation density per pulse, which suggests the threshold behavior of the persistent phase transition. The fraction was evaluated from the intensity at 633 nm of the spectrum. (b) The difference in DR spectrum between the β phase and the λ phase, which is normalized by the DR spectrum of the β phase.

7.3 Results and discussions

7.3.1 Static diffuse reflectance spectra

In Fig. 7.2(a), the diffuse reflectance (DR) spectrum of the initial β phase is shown as a thick red curve. The DR spectrum of the λ phase, which is created from the β phase after pumping with 5000 shots of 8.5×10^{-7} mJ μm^{-2} pulses, is also shown in Fig. 7.2(a) as a thin black

(a) Experimental data

(b) Reference data
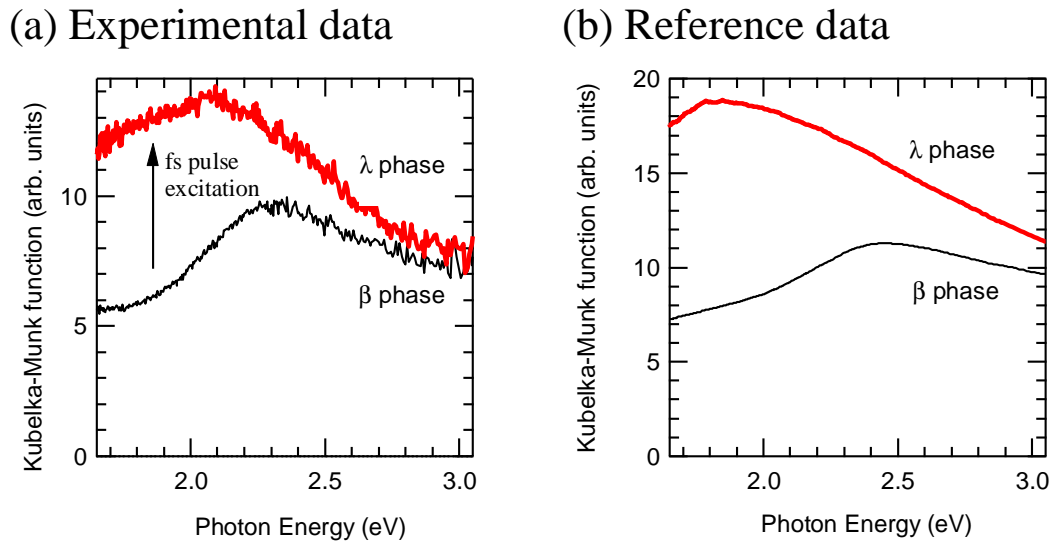
Fig. 7.3: (a) The absorption spectra (Kubelka-Munk function) converted from the diffuse reflectance spectra shown in Fig. 7.2(a). (b) The Kubelka-Munk spectra cited from Fig. 3b in Ohkoshi *et al.* [106]. For comparison, the horizontal axis of the graph is rescaled from the original.

curve. The absorption spectra (Kubelka-Munk function) of the β and λ phases converted from these DR spectra through Eq. (7.1) are shown in Fig. 7.3(a). These spectra qualitatively agree with those in Fig. 7.3(b) cited from Ohkoshi *et al.* [106]. We therefore confirm that the state generated by the femtosecond pulses is the λ phase. Because of the permanent phase transition, the color of the irradiated surface changes from brown to black. Since DR is basically similar to transmittance as mentioned in Sec. 7.1, the decrease in the DR in Fig. 7.2(a) corresponds to an increase in absorbance.

Figure 7.2(b) shows the difference in the DR spectrum between the β and λ phases, which is normalized by the DR spectrum of the β phase. Hereafter, we call the difference in the DR spectrum in Fig. 7.2(b) as " $DR_{\beta \to \lambda}$ " for simplicity ($DR_{\beta \to \lambda}(\lambda) = \frac{DR_\lambda - DR_\beta}{DR_\beta}$). From this figure, we see the spectral tendency that the decrease of DR associated with the phase transition is larger at wavelengths longer than about 550 nm. In other words, the increase in absorbance at the longer wavelengths is an indication of the phase transition from β to λ phase.

The inset in Fig. 7.2(a) shows the excitation fluence dependence of the β phase fraction after 5000-shots pumping[2]. The fraction was estimated from the DR at 633 nm. This plot shows a

---

[2]We confirmed that the conversion yield quickly saturates after around 500-shots pumping, and the yield obtained by 500 and 5000 shots differs only by about 10 %. Since the yield evaluated at 5000 shots is surely regarded as a saturated value, we adopted this excitation condition in making this plot.

clear threshold in the fluence per pulse, rather than the total deposited energy. Furthermore, we confirmed that the saturated value of the phase fraction is determined by the maximum fluence which the sample has experienced so far, even if the sample has been already excited by other 5000 shots with weaker fluence. The threshold fluence at the onset of the persistent transition is about 4×10^{-7} mJ μm^{-2} pulse^{-1}, and the transition is completed when excited with pulses more powerful than 8×10^{-7} mJ μm^{-2} pulse^{-1}. This value is consistent in order of magnitude with the previous report that applied a nanosecond green laser as the excitation source [106].

7.3.2 Time-resolved diffuse reflection spectroscopy in PIPT from β to λ phase

Temporal evolution of ΔDR

The PIPT dynamics from β to λ phases was investigated first. Figures 7.4(a) and 7.4(b) show the temporal evolution of the transient diffuse reflectance (ΔDR) probed at 633 nm after optical excitation. Here, the excitation fluence was adjusted to 2×10^{-7} mJ μm^{-2} pulse^{-1}, which is about one half of the threshold where the persistent transition starts. The overall dynamics of the ΔDR shown in Figs. 7.4(a) and 7.4(b) can be split into the following five processes:

(i) Just after excitation, the ΔDR decreases about 17% within a few hundreds of femtoseconds.

(ii) Subsequently, the ΔDR increases about 7% within the next 1 ps.

(iii) The ΔDR decreases again, gradually but substantially, for about 10 ps.

(iv) Within the next 20 ns, the ΔDR relaxes exponentially to 10% its initial value.

(v) Finally, the ΔDR attenuates non-exponentially over several hundreds of microseconds, and the sample returns to its initial state.

In Fig. 7.5, the ΔDR curve till 100 ns is shown in a linear time scale with the fitting result. Here, (iv) the exponential decay component with a lifetime of about 20 ns is clearly seen. This suggests that processes (iv) and (v) should be explained by different relaxation mechanisms.
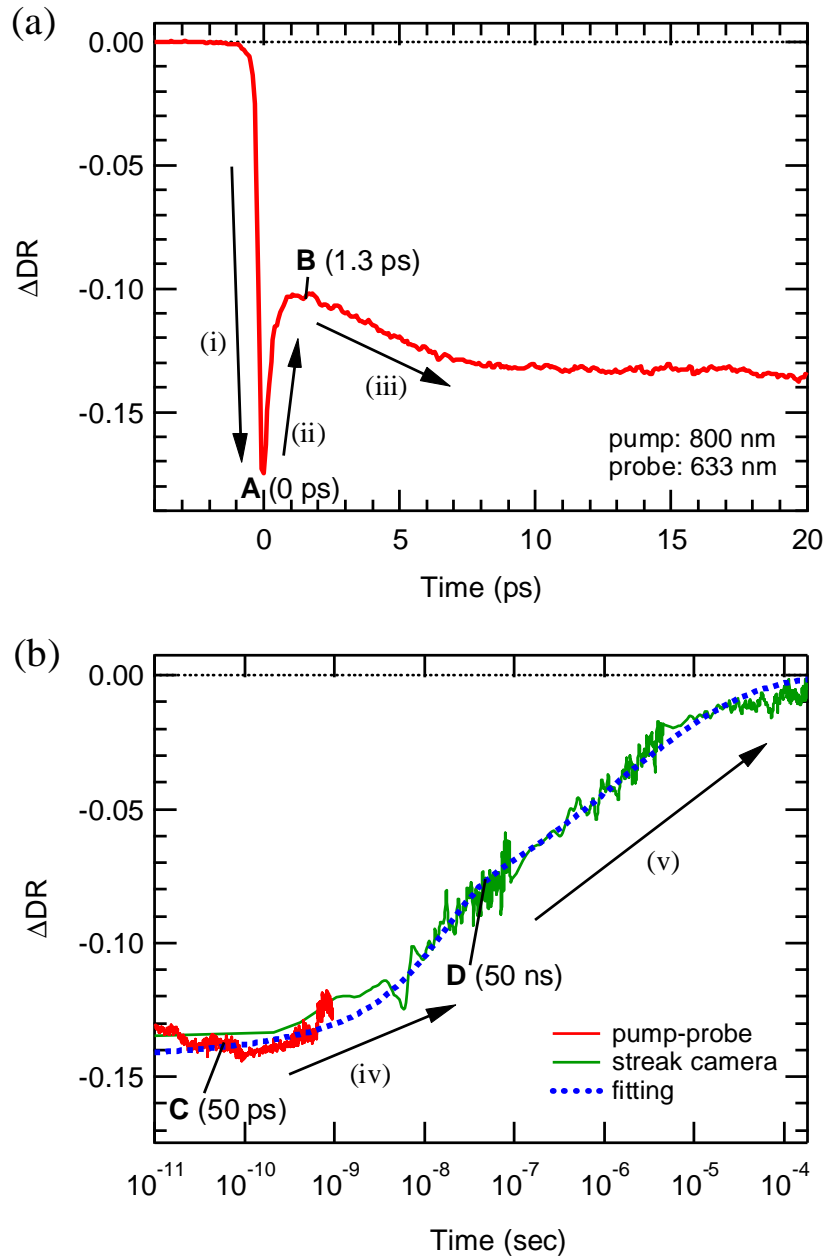
Fig. 7.4: (a) Temporal evolution of the transient diffuse reflectance (ΔDR) probed at 633 nm after pumping at 800 nm. The tip of the sharp decline is referred to as the time origin (0 ps) throughout this chapter, though the true excitation time may be slightly earlier within temporal resolution. (b) The ΔDR curve probed at 633 nm in the range from 10 ps to 200 μs in a logarithmic scale, which is obtained by pump-probe measurement in the earlier stage (red) and by streak camera in the later stage (green). The blue dotted line is a fitting curve (see Fig. 7.5 for detail). The Roman indices (i)-(v) represent the characteristic five processes in the transition, while the capital letters, A (0 ps), B (1.3 ps), C (50 ps), and D (50 ns), represent the typical relaxation stages between these processes.

103
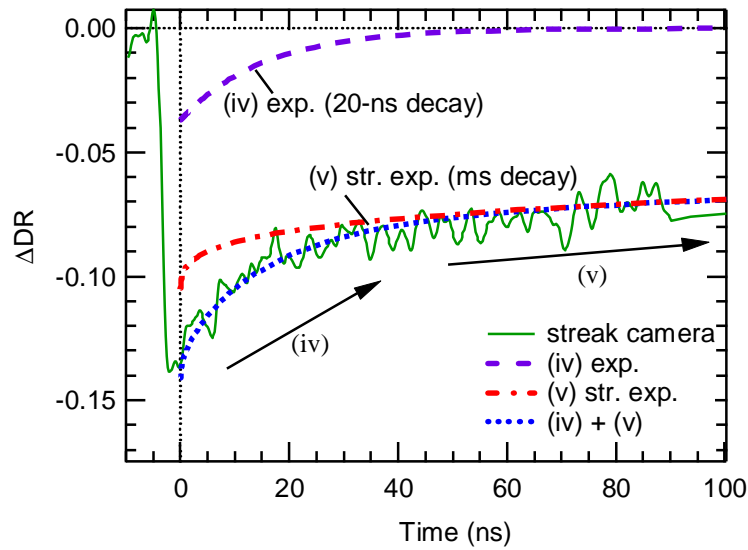
Fig. 7.5: The ΔDR curve till 100 ns rescaled from Fig. 7.4(b) in a linear scale. The fitting curve is composed of two decay components: (iv) an exponential function with a time constant of ~20 ns and (v) a stretched exponential function with an averaged time constant of ~20 μs and a β factor of ~0.3.
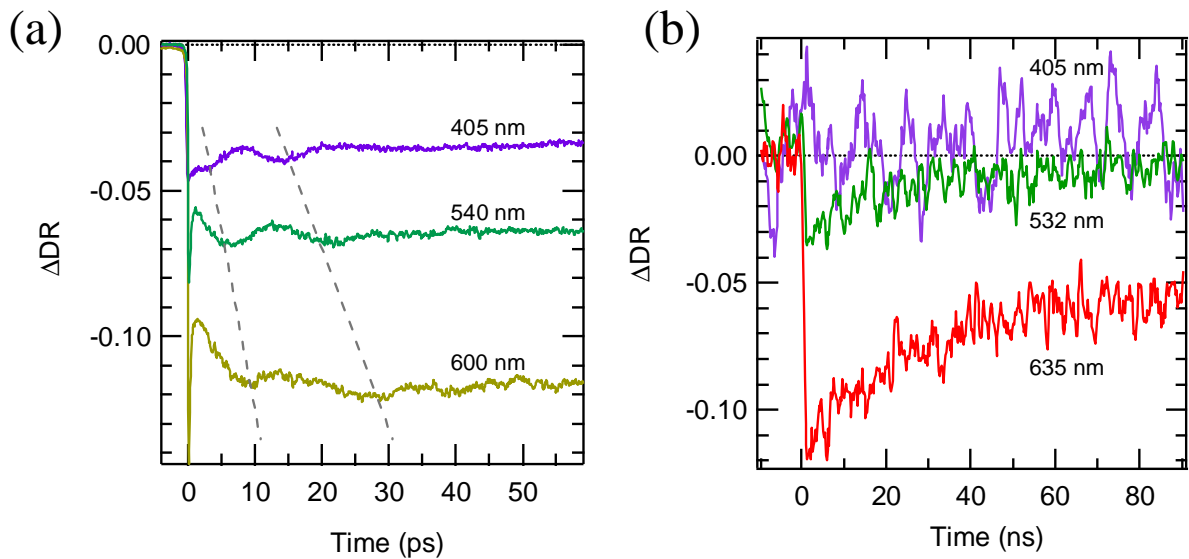
Fig. 7.6: (a) The ΔDR curves till 60 ps probed at 405, 540, and 600 nm, and (b) those till 90 ns probed at 405, 532, and 635 nm. The dashed lines shown in (a) are visual guides to show the variation of the periods of the oscillations.

Spectral analysis

In order to understand the relaxation processes, we examined the probe wavelength dependence of the temporal behavior. First, Fig. 7.6(a) shows the ΔDR curves till 60 ps probed at 405, 540,
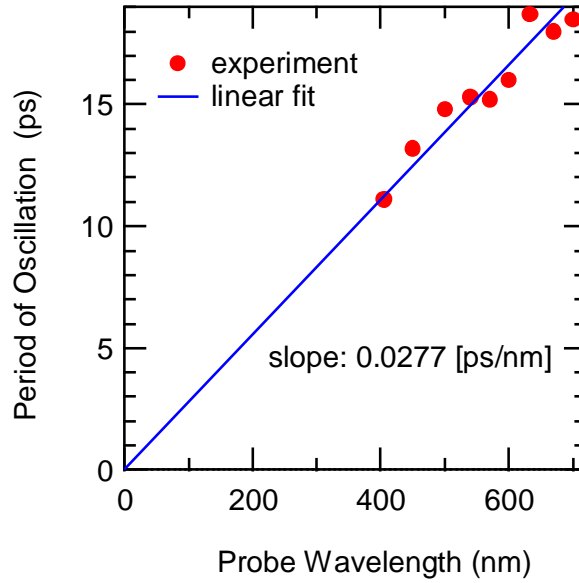
Fig. 7.7: Period of the phonon-induced oscillation of ΔDR depending on the probe wavelength shown in Fig. 7.6(a).

and 600 nm in the pump-probe measurement. Here, it is found that the amplitude of ΔDR greatly depending on the probe wavelength; generally, the amplitude increased as the probe wavelength became longer.

In Fig. 7.6(a), damped oscillations with a lifetime of several tens of picoseconds are also observed. Since the period of the oscillation is proportional to the probe wavelength as shown in Fig. 7.7, this component is attributed to the interference between probe pulses reflected at the front surface of the microcrystals and those reflected from the wavefront of acoustic phonon wave packets propagating into the microcrystals. The acoustic phonon burst originates with impulsive lattice expansion, which may be associated with the phase transition. Similar periodic reflectivity modulation associated with PIPT has been often observed in transient reflection measurements [142, 143]. Although these reports were performed with bulk crystals, the similar concept can be adopted to the present case as inter-nanoparticle propagation of the elastic wave. Here, the periods were evaluated from the time interval between the first two local minima in the damped oscillations. The plot includes a linear fit, with a slope of 0.0277 ps nm^{-1}. If a typical refractive index of 2.2-2.5 in β-Ti$_3$O$_5$ is assumed, the sound velocity is estimated to be 8.2-7.2 km s^{-1}. In the following analyses, as the amplitude of the oscillation is smaller than the typical magnitude of the ΔDR, we ignore this oscillation component.

Next, in Fig. 7.6(b), we show the ΔDR curves till 90 ns probed at 405, 532, and 635 nm
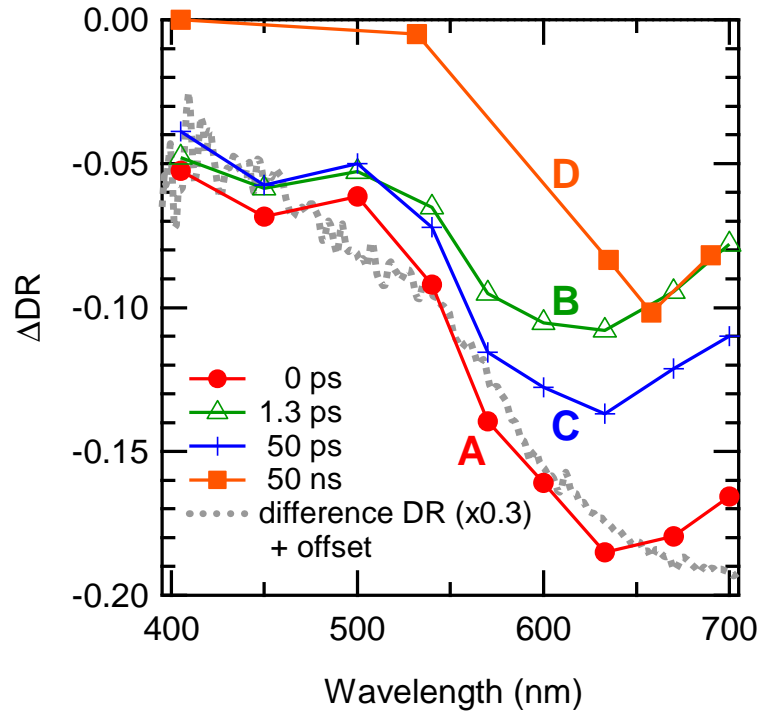
Fig. 7.8: ΔDR spectra at 0 ps (red filled circles), 1.3 ps (green open triangles), 50 ps (blue crosses), and 50 ns (orange filled squares). Behind the spectrum at 0 ps, the difference DR spectrum ($DR_{\beta \to \lambda}$) shown in Fig. 7.2(b) is replotted with a coefficient of 0.3 and an offset for comparison (gray dotted curve). The capital letters A-D correspond to those defined in Fig. 7.4.

in the streak-camera measurement. In this long time range, the similar spectral tendency as shown in Fig. 7.6(a), the larger ΔDR amplitude at larger probe wavelength, was observed.

In Fig. 7.8, the spectral information obtained from Figs. 7.6(a) and 7.6(b) is summarized. Figure 7.8 shows four typical ΔDR spectra characterizing the relaxation stages. The corresponding stages and delay times used in Fig. 7.8 are noted in Fig. 7.4 using four capital letters, A (0 ps), B (1.3 ps), C (50 ps) and D (50 ns). First, the ΔDR spectrum at 0 ps (stage A, red filled circles) is plotted in Fig. 7.8. Behind it, $DR_{\beta \to \lambda}$ is plotted again with an appropriate coefficient (=0.3) and an offset for comparison (gray dotted curve). Comparing these, the spectrum at 0 ps is well represented by the spectral variation associated with the phase transition and a constant component. We ascribe the latter to Drude absorption, which is expected to be nearly flat in this wavelength range. This suggests that just after excitation, the charge ordering in the semiconductor β phase is dispersed within a few hundreds of femtoseconds, and that not only excited free carriers but also metallic λ phases are generated through the process

(i). Here, the "free carrier" is attributed to the carrier excited to the conduction band of the semiconducting β phase. According to the coefficient (0.3) multiplied with the $DR_{\beta \to \lambda}$ in Fig. 7.8, the λ fraction gained here is approximately 30%. Judging from this rapid response, this phase transition is likely to be non-thermal.

Second, the ΔDR spectrum at 1.3 ps (stage B, green open triangles) is plotted in Fig. 7.8, which corresponds to the final state of the process (ii). By comparing this spectrum with that plotted at 0 ps, it is found that the λ component ($DR_{\beta \to \lambda}$) decreases, while the Drude component remains almost constant. This is attributed to the partial disappearance of the metastable λ phase. The ΔDR spectrum at 50 ps (stage C, blue crosses) is also plotted in Fig. 7.8, which corresponds to the final state of the process (iii). By comparing this spectrum with that at 1.3 ps, interestingly, we find that the λ component again increases gradually, over about 10 ps.

Third, the ΔDR spectrum at 50 ns (stage D, orange filled squares), which corresponds to the final state of the process (iv), is shown in Fig. 7.8. By comparing the spectrum with that at 50 ps, we find that only the flat component (the Drude component) disappears. Since the residual ΔDR spectrum at 50 ns resembles the λ component, the state at 50 ns is ascribed to long-surviving metastable λ domains. From these facts, process (iv) is attributed to the extinction of the excited free carriers. As shown in Fig. 7.5, this component exponentially annihilates within 20 ns.

Based on the interpretations so far, the final process (v) over several hundreds of microseconds can be ascribed to shrinking and annihilation of the metastable λ domains. As shown in Fig. 7.4(b), this non-exponential decay curve can be reproduced by a stretched exponential function: $\exp[-(t/\tau)^{\beta}]$, where τ is the time constant and β is the stretching factor $(0 < \beta < 1)$. From the fitting analysis between about 10^{-9} and 10^{-4} s, the average lifetime $< \tau >$ and β are estimated to be ~20 μs and ~0.3, respectively. This result indicates that various relaxation processes with lifetimes distributed over several orders of magnitude, centered at tens of microseconds are involved. It may be ascribed to the wide distribution of the domain size of the metastable λ phase.

Excitation fluence dependences

Next, we focus on the excitation fluence dependence of the ΔDR. Figure 7.9 shows the fluence dependence of ΔDR probed at 633 nm at stages A-D. First, we can find that the ΔDR at 0 ps (stage A, red filled circles) decreases linearly below about 1.0×10^{-7} mJ μm^{-2} pulse^{-1} and
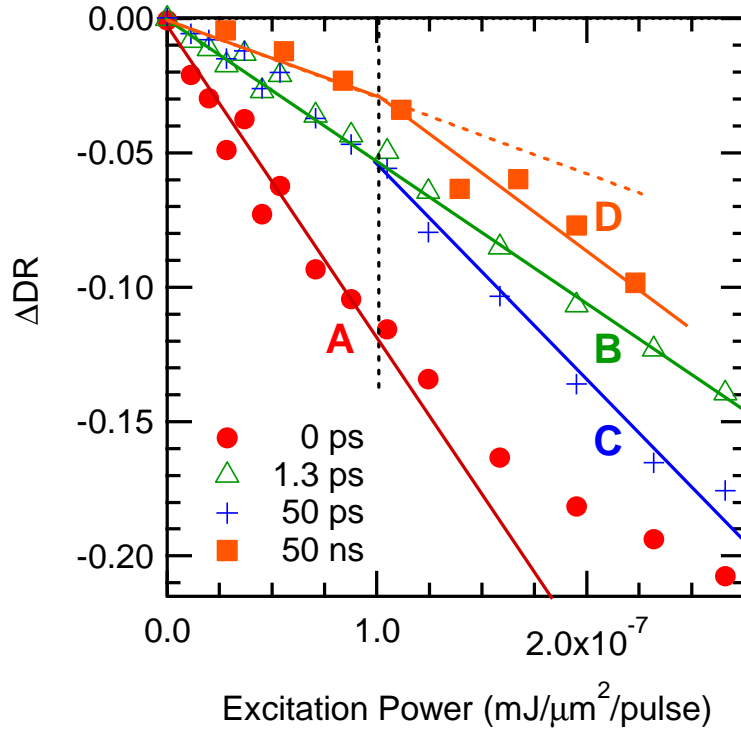
Fig. 7.9: Excitation power dependence of the ΔDR probed at 633 nm at 0 ps (red filled circles), 1.3 ps (green open triangles), 50 ps (blue crosses), and 50 ns (orange filled squares). The capital letters A-D correspond to those in Figs.7.4 and 7.8. The lines are visual guides for easier discrimination of the threshold behaviors.

starts saturating around this fluence, while the ΔDR at 1.3 ps (stage B, green open triangles) does not show such a tendency.

These fluence dependences can be interpreted as follows. When electrons in the initial β phase are locally excited by photons, the charge ordering in the β phase is disturbed around the excited sites, and metallic λ phase domains appear. In general, domains must be larger than some critical size to survive and maintain stability; domains smaller than the critical size annihilate quickly. Therefore, in the weaker excitation range ($< 1.0 \times 10^{-7}$ mJ μm^{-2} pulse^{-1}), the locally generated small metallic λ phase fragments should disappear in a short time. In addition, the amount of the transiently created λ phase fractions is expected to be proportional to the excitation fluence.

On the other hand, the saturating behavior observed in the stronger excitation range ($> 1.0 \times 10^{-7}$ mJ μm^{-2} pulse^{-1}) can be explained as follows. When the already generated λ phase domains are excited again by photons that come later, the extent of the λ phase will not increase. Consequently, as the excitation fluence increases, the quantum efficiency of
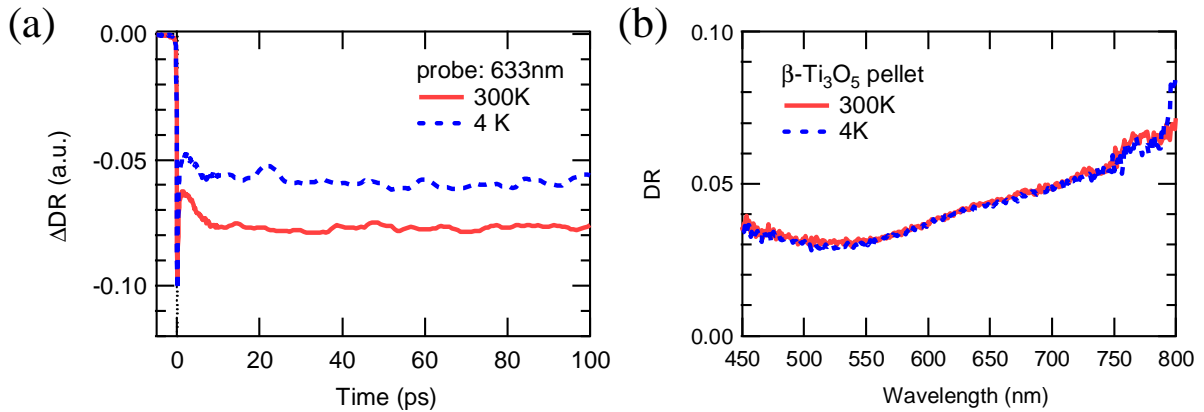
Fig. 7.10: (a) Time evolution of ΔDR in PIPT from β to λ phases observed at 300 and 4 K. (b) DR spectra of β-Ti$_3$O$_5$ measured at 300 and 4 K.

nucleation decreases, resulting in the saturating behavior. Such saturation is expected to be observable when each domain is generated closely enough together to cause overlapping. Hence, the threshold fluence around 1.0×10^{-7} mJ μm^{-2} pulse^{-1} can be interpreted as the critical condition where each λ phase nucleus begins to overlap.

Second, the ΔDR at 1.3 ps decreases linearly without a threshold, while that at 50 ps (stage C, blue crosses) changes evidently in slope at 1.0×10^{-7} mJ μm^{-2} pulse^{-1}. This threshold behavior suggests that the process (iii), the delayed increase of the λ phase fraction, may involve some cooperating mechanism. We also find that the fluence dependence at 50 ns (stage D, orange filled squares) exhibits a similar threshold behavior. This suggests that the λ phase domains existing at 50 ns share an origin with those found at 50 ps.

The threshold behavior at 50 ps can be understood as follows. The λ phase fraction increases due to the growth of the λ phase domains via cooperative interactions during process (iii). Such a domain growth process via cooperative interactions has been reported in other PIPT materials [7, 144]. The λ phase domains existing at 1.3 ps, which correspond to the initial stage of the domain growth, have domain sizes large enough to survive avoiding the fast annihilation process. The response time of about 10 ps may correspond to the time required for growth to achieve a maximum size. The grown domains at this stage are sufficiently large and survive for hundreds of microseconds. These interpretations that include domain growth can explain the threshold tendency observed at 50 ps.

Here, in order to examine the effect of laser heating in the ΔDR curves, the temperature dependences of DR and ΔDR were studied. As shown in Fig. 7.10(b), the static DR was

109
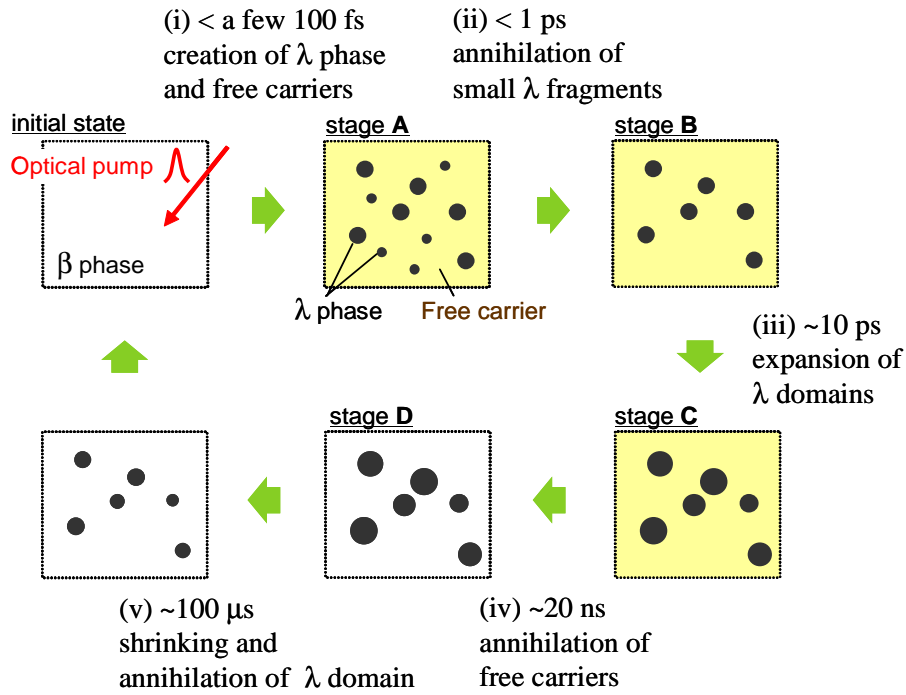
Fig. 7.11: Schematic drawing of the relaxation dynamics in the case that β-Ti$_3$O$_5$ is excited below the threshold for the persistent transition. The yellow-masked background represents the excited free carriers.

constant within a small margin of variation when the temperature was changed from 300 K to 4 K. Hence, if the ΔDR observed at 300 K is originated from a thermal effect, such transient response should not be observed at a much-lower temperature of 4 K. However, as shown in Fig. 7.10(a), a similar ΔDR waveform was measured at 4 K, whose amplitude was of the same order to that observed at 300 K. These facts indicate that the slow response through processes (iii)-(v) is attributed to non-thermal process, and the effect of laser heating is discarded in this experiment.

Scenario of the semiconductor-to-metal phase transition in nano-granular Ti$_3$O$_5$

Based on the discussions so far, a model of the photoinduced phase transition dynamics under excitation fluence that remains below the threshold is proposed as summarized in Fig. 7.11.

 (i) When the β phase is optically pumped, excited free carriers and λ phase fractions are generated within a few hundreds of femtoseconds.

 (ii) The small λ phase fragments vanish within the next 1 ps.

(iii) The surviving metastable λ phase domains expand via cooperative interactions for about 10 ps.

(iv) The excited free carriers are annihilated within 20 ns.

(v) The metastable λ phase domains shrink and annihilate within several hundreds of microseconds.

In this model shown in Fig. 7.11, the domain growth is assumed in the nanoparticles, because the inter-particle interaction involving the domain growth would not be expected naturally. The accurate estimation of the size of the created domain is difficult only from this experiment, however, it can be roughly estimated from the material properties given in the previous researches: The size of the nanoparticle is 25 ± 15 nm as shown in Sec. 7.2.1, and that of the unit cell is ~1 nm as shown in Table 5.1. Therefore, it can be expected that there are fraction-like small domains showing the fast annihilation and large domains composed of ~10^4 Ti ions at most.

Here, the "excited free carriers" are assumed to be the carriers accumulated at the bottom of the conduction band in the semiconducting β phase. Although the effect of the carriers trapped at the nanoparticle's surface and/or defects may be included to the Drude component, the separation of the phenomena should be difficult only by the present experiment.

Furthermore, note that in process (v) the lifetime has a wide distribution that reflects the fluctuating size of the metastable λ phase domains. As the sample is excited with higher fluences, the average size of the λ phase domains created around 10 ps becomes larger, and some of them will attain large enough sizes to persist, leading to a permanent phase transition.

7.3.3 Dynamics in PIPT from λ to β phase

Next, the PIPT dynamics in the inverse direction (λ to β phases) was investigated by probing ΔDR at 633 nm with the same experimental setups.

Experimental conditions

The λ phase was prepared from the β-Ti_3O_5 pellet by the PIPT with 800-nm pulse irradiation. Here, the excitation density of the irradiated light was 8.5×10^{-7} mJ μm^{-2} pulse^{-1}, which was large enough to convert the pellet to λ phase persistently as we can see from the inset in Fig.
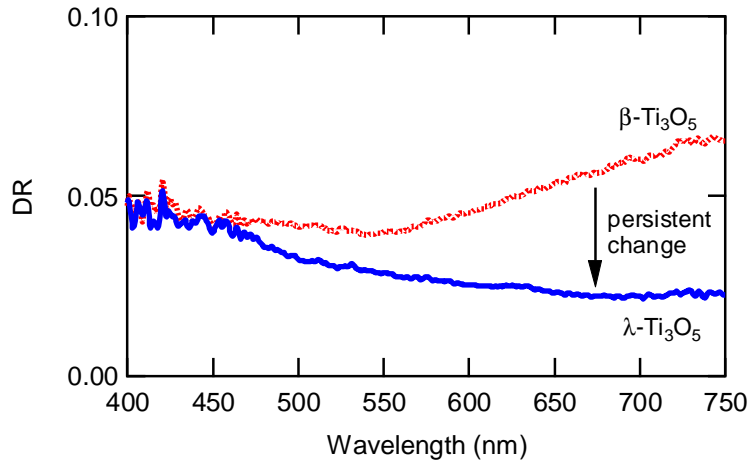
Fig. 7.12: Static DR spectrum of the initial state in λ phase (blue solid line) prepared from the β phase (red dotted line) by light irradiation (800 nm, 8.5×10^{-7} mJ μm^{-2} pulse^{-1}).

7.2(a). Figure 7.12 shows the DR spectrum of the prepared λ phase. The conversion from β to λ phases was confirmed from the spectral shapes in Fig. 7.12.

In nano-granular Ti$_3$O$_5$, the λ phase can be transferred to the β phase by strong light irradiation as shown in Fig. 5.5(c). (Please remember that this material has the two thresholds involved in the reversible PIPT. Here, the PIPT from λ to β phases, which is related to the higher threshold, is discussed.) In the time-resolved measurement, the pump power was set to 8.5×10^{-7} mJ μm^{-2} pulse^{-1}. Although the persistent PIPT from λ to β phases does not occur with this excitation condition, the transient phase change is expected to be measured.

When the sample was excited with slightly higher power than 8.5×10^{-7} mJ μm^{-2} pulse^{-1}, the sample surface got whitened and deteriorated during experiment; the maximum excitation power was limited by this deterioration. We speculate this is caused by the laser-induced dielectric breakdown and/or the laser heating at the sample surface . Since we could not measure the dynamics in the experiment with the streak camera due to the low signal intensity with this condition, we only performed the pump-probe measurement observing till 1 ns.

Temporal evolution of ΔDR

The temporal evolution of ΔDR in PIPT from λ to β phases was probed at 633 nm, and the result is shown in Fig. 7.13. Here, a very complicated response where positive and negative changes are overlapping can be found, and careful observation reveals the following four main features:
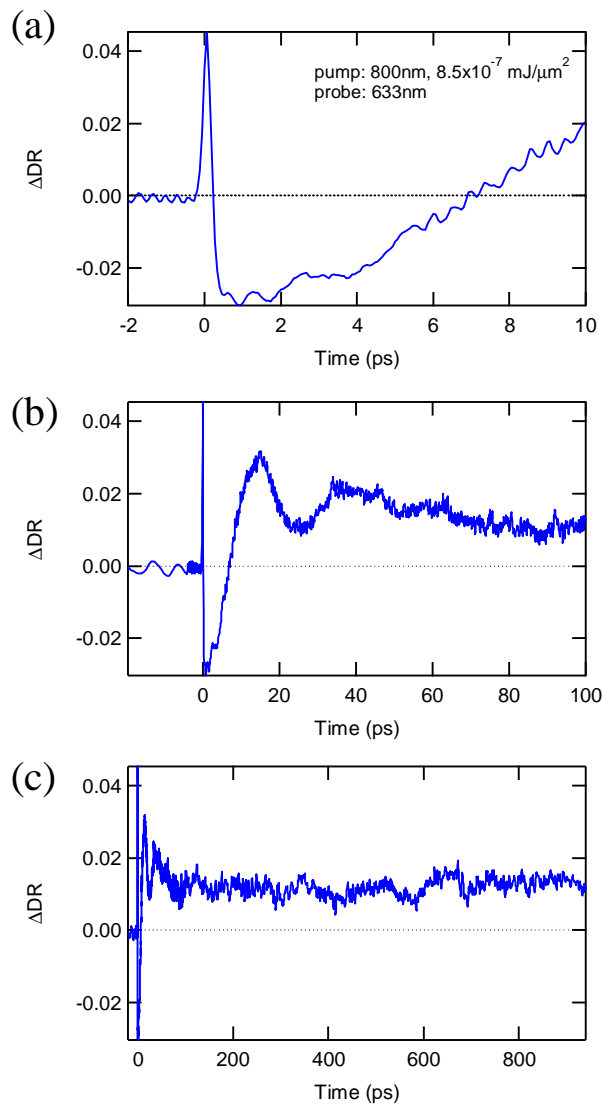
Fig. 7.13: Temporal evolution of the ΔDR in the PIPT from λ to β phases: (a) till 10 ps, (b) till 100 ps, and (c) till ~1 ns.

  (i) Just after excitation, the ΔDR increased to about 4 % within a few 100 fs, which was limited by the system time resolution.

  (ii) Subsequently, the ΔDR turned to negative to about -3% within 1 ps.

 (iii) Within the next several ps, the ΔDR gradually increased again. The ΔDR turned to positive around 7 ps, and reaches about 3% around 15 ps. This state, having positive ΔDR, lasted longer than 1 ns.
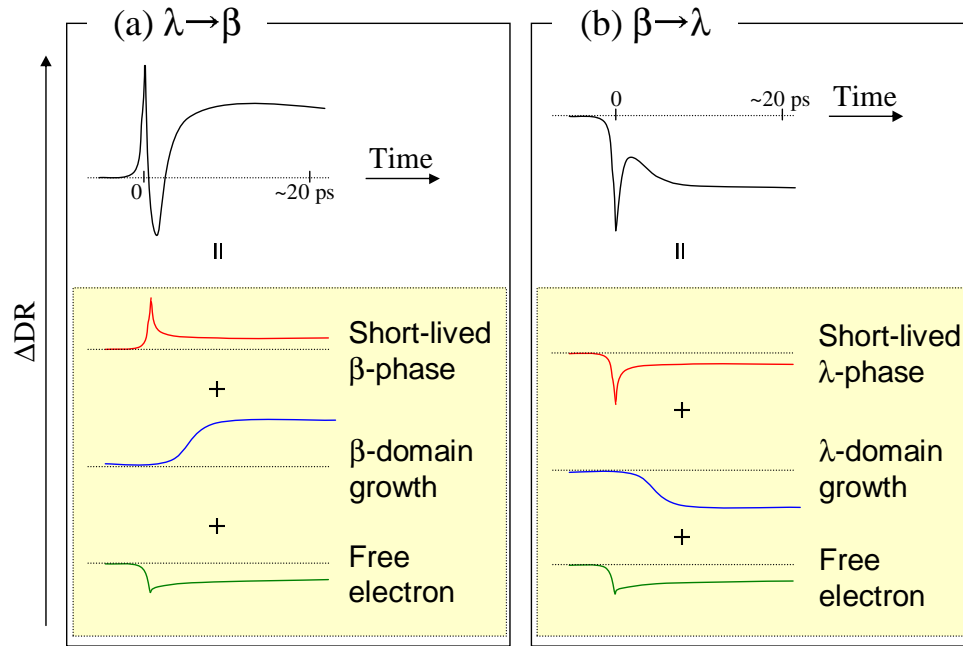
Fig. 7.14: Illustrations about the interpretation of ΔDR waveforms in the ps region in (a) λ → β and (b) β → λ phase transitions. Here, the oscillation component observed around several tens of ps was removed, because this component was attributed to the acoustic phonon burst, which does not directly relate to the PIPT.

(iv) Around 10-50 ps, a damped oscillation component, whose amplitude was about 2 % at maximum, was overlapped on the ΔDR curve. The period of the oscillation was about 20 ps, which was almost the same as that found in the inverse PIPT (Fig. 7.6(a)).

The increase of ΔDR basically corresponds to the increase of the β phase. Therefore, this result roughly indicates that the β phase is created in such a ultrafast time range.

It is interesting to compare these ΔDR waveforms with those observed in the inverse PIPT dynamics (β → λ) shown in Fig. 7.4. Figure 7.14 shows the illustrations of ΔDR waveforms in ps region in (a) λ → β and (b) β → λ phase transitions. Here, the oscillation component observed around several tens of ps was removed, because this component was attributed to the acoustic phonon burst, which does not directly relate to the PIPT. As shown in Fig. 7.14(b), from the discussion in the previous section (Sec. 7.3.2), it has been found that the ΔDR in ps region in β → λ phase transition can be decomposed into the three components, the short-lived λ phase creation, the λ-domain growth, and the free electron creation. Comparing this analysis with the ΔDR in λ → β phase transition shown in Fig. 7.14(a), we speculate that it is composed of the following three components; short-lived β phase creation, β-domain growth, and free

114

electron creation[3]. Note that the ΔDR due to β phase creation is opposite to that due to λ phase creation, while ΔDR due to free electron creation is negative regardless of the direction of PIPT.

Based on this discussion, the relaxation processes extracted from Fig. 7.13 are interpreted, and the following PIPT scenario is proposed:

(i) The sharp ΔDR increase around 0 ps (Fig. 7.13(a)) is ascribed to the temporal creation of β phase. This rapid response indicates that this phase transition is a non-thermal process.

(ii) The decrease of ΔDR observed within 1 ps (Fig. 7.13(a)) is attributed to the decrease of the small β phase fraction and creation of the excited free carriers.

(iii) The gradual ΔDR increase taking about 10 ps (Fig. 7.13(a)) is attributed to the gradual expansion of the metastable β phase domain. The transiently created β phase domain lasts longer than 900 ps (Fig. 7.13(c)).

(iv) The damped oscillation component observed around 10-50 ps (Fig. 7.13(b)) is attributed to the acoustic phonon burst, which is the same phenomenon occurred in the inverse process as discussed for Fig. 7.7.

Although detailed characterization is difficult due to the complex overlapping of the multiple components, the PIPT dynamics from λ to β phases could be roughly interpreted in this way. Particularly, the dynamics around 7 ps is unclear, where the two components, (ii) the relaxation of excited free carriers and (iii) the onset of gradual increase of β phase, are overlapping. In order to disentangle these complex phenomena, further studies are required.

Anyway, the most significant indication obtained from this experiment was that the creation of the β phase occurs in this fast time range: (i) transient creation of β-Ti_3O_5 within a few 100 fs and (iii) gradual creation of β-Ti_3O_5 taking about 10 ps. As it is found in Fig. 7.13(c), the positive ΔDR component, corresponding to the creation of β-Ti_3O_5, was clearly observed. In other words, the onset of this metal-to-semiconductor PIPT lies in these very fast time scales as well as the PIPT in the inverse direction.

---

[3]Here, the "free electron" is tentatively attributed to the carriers excited in the λ-Ti_3O_5 having the long life time because of the trapping at the surface and/or the defects. As another possibility, the free electron component can be attributed to the free carriers located on the conduction band of the small amount of β-Ti_3O_5.

7.4 Summary

In conclusion, we characterized the PIPT dynamics in nano-granular Ti_3O_5 by time-resolved diffuse reflection spectroscopy, over a wide range of time scales, from femtoseconds to microseconds[4].

The semiconductor-to-metal phase transition (β to λ phases) was mainly investigated in detail. From the excitation fluence dependences, we found several threshold behaviors characteristic of the photoinduced phase transition. In addition, from the spectral analysis, we proposed a PIPT model that the transient phase transition occurs within a few hundreds of femtoseconds and that 40% of the converted λ phase fractions revert to the β phase within 1 ps. This fast response indicates that this phase transition is a non-thermal process. Carriers are generated instantaneously and disappear within 20 ns. The delayed increase of the λ phase from 1 ps to 10 ps is ascribed to the growth of the metallic domain. The decay components having time constants spread widely between 10^{-9} and 10^{-4} s are well represented by a stretched exponential function and ascribed to shrinking and annihilation processes of the size-distributed metallic domains.

The ultrafast dynamics in the inverse process (λ to β phases) was also investigated with the pump-probe measurement. From the comparison with the case of the inverse PIPT, the transient changes were roughly characterized, and the PIPT model was proposed. It was indicated that the β phase is transiently created within a few 100 fs, and the β phase domain gradually increase taking about 10 ps. The metastable β phase lasts longer than 1 ns.

In both of these PIPTs, the fast onset within a few hundreds of femtoseconds and the subsequent stabilization process within 10 ps were suggested. This observation indicates the applicability of this material to ultrafast photo-switching.

---

[4]In actuality, at the same time as our study, a single-shot time-resolved reflectivity measurement at 800 nm in ns time scale has been reported by Ould-Hamouda *et al.* [112]. In this report, they insisted that the λ-to-β PIPT occurs within 900 ns due to both laser induced shock wave and heating, while the β-to-λ PIPT occurs within 20 ns due to laser heating. Although the interpretation is different from ours, the given data are consistent with and complementary to our experiment.

Part III

Conclusion

Chapter 8

Conclusion

8.1 Conclusion

In this thesis, we investigated the PIPT dynamics in the two optical switching materials, $RbMn[Fe(CN)_6]$ and nano-granular Ti_3O_5.

In Chapter 3, the dynamics of the reversible PIPTs between LTP and PIHTP in $RbMn[Fe(CN)_6]$ was investigated by time-resolved CN vibration spectroscopy. By monitoring the CN stretching vibration modes, which are sensitive to the valence states of the adjacent metal ions, we quantified not only LTP (Fe^{2+}-CN-Mn^{3+}) and PIHTP (Fe^{3+}-CN-Mn^{2+}) but also the domain boundary configurations (Fe^{2+}-CN-Mn^{2+} and Fe^{3+}-CN-Mn^{3+}). By analyzing with the phenomenological spectral fitting model, we observed not only the instantaneous charge transfer but also the fast generation of large amount of the boundary configuration, suggesting that relatively small domains are created at the early stage of the transition. This is the first demonstration detecting the nucleation process by directly observing phase domain boundaries.

In Chapter 4, the magnetic dynamics in the charge transferred PIPT in $RbMn[Fe(CN)_6]$ was investigated by time-resolved Faraday rotation spectroscopy. Here, the PIPT from LTP to HTP observed around hysteresis was characterized. By comparing the results from those of time-resolved absorption spectroscopy, it was suggested that the paramagnetic spin system follows the instantaneous changes in the electronic system, while the lattice system slowly relaxes taking about 90 ps. From these experiments, the electronic, structural, and spin dynamics in the picosecond region in $RbMn[Fe(CN)_6]$ were seperately characterized.

In Chapter 6, the THz conductivity in nano-granular Ti_3O_5 was investigated by THz-TDS.

This information is important because the conductivity in nanoparticles is well characterized in the THz frequency range, and because Ti_3O_5 shows metal-semiconductor transition. In this experiment, the THz conductivities in both of metallic λ-Ti_3O_5 and semiconducting β-Ti_3O_5 were observed. From fitting analyses, the THz optical conductivity obtained from the nano-granular Ti_3O_5 was well reproduced by the Drude-Smith model, which is an extended Drude model where carrier backscattering at the grain boundary is taken into account. The results indicated that carrier localization in nanocrystals plays an important role in the THz conductivity of nano-granular Ti_3O_5.

In Chapter 7, the PIPT dynamics in nano-granular Ti_3O_5 was investigated by time-resolved diffuse reflection spectroscopy. Here, the dynamics of the semiconductor-to-metal transition (β-$Ti_3O_5 \rightarrow \lambda$-$Ti_3O_5$) was mainly characterized. With time-resolved measurement conducted over a wide range of time scales, from femto- to microseconds, the entire transient behavior was revealed. From the spectral analysis, we proposed the PIPT model that the semiconductor-to-metal phase transition occurs within a few hundreds of femtoseconds, and the created λ phase domain expands and stabilizes within ~10 ps. The transient state lasts till several hundreds of microseconds. In the inverse PIPT (λ-$Ti_3O_5 \rightarrow \beta$-$Ti_3O_5$), the transient creation of β phase domain was indicated. Based on the proposed PIPT model, the time response of the domain creation process was expected to be similar to that of λ phase creation in the semiconductor-to-metal transition.

In this way, the PIPT dynamics of $RbMn[Fe(CN)_6]$ and nano-granular Ti_3O_5 were characterized by using the various measurement methods. The knowledge obtained from this research will lead not only to the deeper insight for the dynamical mechanisms of the reversible phenomena in these two optical switching materials but also to the understanding of the microscopic dynamics involving the domain growth. This comprehension will further promote the research field of PIPT.

From the viewpoint of the research on the PIPT dynamics in optically switching functional materials, the following results should be particularly significant. First, in Chapter 3, the bi-directional PIPT dynamics in $RbMn[Fe(CN)_6]$ was characterized, which is the important information to understand its switching mechanism. Furthermore, in this experiment, we successfully observed the transient responses of the persistent phase transitions by applying the reversing CW light to avoid the accumulation of the photoinduced phase. This method can be applied to other switching materials which show persistent phase changes, provided the phase can be reversed by irradiating at different wavelengths. Thus, our present experiment

should be a good demonstration investigating the PIPT dynamics in optical switching materials. In addition, in Chapter 7, the bi-directional PIPT dynamics was characterized in the nano-granular Ti_3O_5, and the plausible PIPT models were proposed. This knowledge is the firstly obtained information about the transient responses in this material and should be the fundamental data for the future researches on this switching phenomenon. We particularly note that the ultrafast PIPT onset and the subsequent phase stabilization process of faster than 10 ps was suggested, indicating the high applicability of this material to ultrafast photo-switching devices.

8.2   Future prospects

In the present study, the various measurement methods (CN vibration spectroscopy, Faraday rotation spectroscopy, THz time domain spectroscopy, diffuse reflection spectroscopy, etc.) have revealed the important properties of the reversible PIPTs in $RbMn[Fe(CN)_6]$ and nano-granular Ti_3O_5. For example, in Chapter 3, the CN vibration spectroscopy successfully extracted the information about the charge transfer processes in the PIPTs in $RbMn[Fe(CN)_6]$. In Chapter 7, the diffuse reflection spectroscopy effectively probed the overall dynamics of the metal-semiconductor phase transitions in the nano-granular Ti_3O_5. However, the mechanisms of these reversible PIPTs have not been completely elucidated only by employing these probe methods, because the assignments given in the proposed PIPT models are not fully ensured. In order to achieve more detailed and accurate understanding, it is essential to perform additional measurements providing information about the PIPT dynamics from other aspects. As a candidate, direct observation of the lattice dynamics is particularly needed, because our present experiments did not directly probe the structural information. Such an experiment will be achieved by time-resolved x-ray diffraction spectroscopy, for example. In addition, it should be also important to perform additional theoretical studies, a thermodynamical simulation of phase transitions involving the domain creation process, for example. By carefully comparing the theoretical results with the experimental ones, it is expected that the microscopic mechanism of the PIPT dynamics can be understood. By performing such further experimental and theoretical studies, the assignments given in our research will be supported and/or improved.

In the spectral analysis using the Drude-Smith model discussed in Chapter 6, there was a problem that the electron density n could not be accurately evaluated because of the c

parameter too close to -1. In such a strongly localized system like the nano-granular Ti_3O_5, this conventionally used type of the Drude-Smith model seems to be limited to give a qualitative insight about the carrier localization. For solving this problem, as mentioned in Chapter 6, the model should be improved to include the effect of the c_n in higher orders, meaning the multi-reflection of the carriers at the domain boundary. Such a new conduction model should be useful in analyzing the THz conductivity not only in the nano-granular Ti_3O_5 but also in other strongly carrier-localized materials.

In Chapter 7, the nano-granular Ti_3O_5 was selected as the sample to observe the reversible PIPT dynamics, because the switching phenomenon occurs (the metallic λ phase can stably exist) only in the nanoparticles (not occur in a bulk). However, since the environment in such a nano-granular sample is generally inhomogeneous, the understanding of the microscopic picture of the PIPTs is apt to be difficult. For more detailed discussion about the PIPT mechanism, it may be useful to perform the similar time-resolved experiment also for a bulk Ti_3O_5 in the semiconducting β phase, trying to observe the transient creation of the λ phase-like state. This experiment will give an insight about the PIPT mechanism without the contribution of the nanoparticle's geometry, and will reinforce the discussions obtained in this thesis with the nano-granular sample.

In addition, it should be also important to study PIPTs in other cyano-complexes and titanium oxides. $RbMn[Fe(CN)_6]$ and Ti_3O_5 have many family materials showing unique PIPTs as explained in Sec. 2.1 and Sec. 5.1. However, there are actually few reports about their PIPT dynamics. By systematically examining the dynamics, general insights of the PIPTs in the family of materials are expected to be obtained. It will lead to the construction of the useful guidelines for developing optical functional materials having great functionalities.

References

[1] P. Papon, J. Leblond, and P. H. E. Meijer, *The Physics of Phase Transitions*, 2nd edition (Springer, 2006).

[2] K. Nasu, *Photoinduced Phase Transitions*, (World Scientific Publishing, 2004).

[3] R. Yabuki and K. Nasu, Phys. Rev. A **320**, 289 (2004).

[4] S. Decurtins, P. Gutlich, C. P. Kohler, H. Spiering, and A. Hauser, Chem. Phys. Lett. **105**, 1 (1984).

[5] S. Koshihara, Y. Tokura, Y. Mitani, G. Saito, and T. koda, Phys. Rev. B **42**, 6853 (1990).

[6] S. Iwai, S. Tanaka, K. Fujinuma, H. Kishida, H. Okamoto, and Y. Tokura, Phys. Rev. Lett. **88**, 5 (2002)

[7] H. Okamoto, Y. Ishige, S. Tanaka, H. Kishida, S. Iwai, and Y. Tokura, Phys. Rev. B **70**, 165202 (2004)

[8] S. Koshihara, Y. Tokura, K. Takeda, and T. Koda, Phys. Rev. Lett. **68**, 1148 (1992).

[9] S. Koshihara, Y. Tokura, K. Takeda, and T. Koda, Phys. Rev. B **52**, 6265 (1995).

[10] K. Miyano, T. Tanaka, Y. Tomioka, and Y. Tokura, Phys. Rev. Lett. **78**, 4257 (1997).

[11] M. Fiebig, K. Miyano, Y. Tomioka, and Y. Tokura, Science **280**, 1925 (1998).

[12] M. Collet, L. Guerin, N. Uchida, S. Fukaya, H. Shimoda, T. Ishikawa, K. Matsuda, T. Hasegawa, A. Ota, H. Yamochi, et. al, Science **307**, 86 (2005).

[13] K. Onda, S. Ogihara, K. Yonemitsu, N. Maeshima, T. Ishikawa, Y. Okimoto, X. Shao, Y. Nakano, H. Yamochi, G. Saito, and S. Koshihara, Phys. Rev. Lett. **101**, 067403 (2008).

[14] A. Cavalleri, Cs. Tóth, C. W. Siders, and J. A. Squier, Phys. Rev. Lett. **87**, 23 (2001).

[15] A. Cavalleri, Th. Dekorsy, H. H. W. Chong, J. C. Kieffer, R. W. Schoenlein, Phys. Rev. B **70**, 161102 (2004).

[16] D. J. Hilton, R. P. Prasankumar, S. Fourmaux, A. Cavalleri, D. Brassard, M. A. El Khakani, J. C. Kieffer, A. J. Taylor, R. D. Averitt, Phys. Rev. Lett. **99**, 226401 (2007).

[17] V. I. Kudinov, A. I. Kirilyuk, N. M. Kreines, R. Laiho and E. Lähderanta, Phys. Lett. A **151**, 358 (1990).

[18] V. Peña, T. Gredig, J. Santamaria, and I. K. Schuller, Phys. Rev. Lett. **97**, 177005 (2006).

[19] M. Rini, R. Tobey, N. Dean, J. Itatani, Y. Tomioka, Y. Tokura, R. W. Schoenlein, and A. Cavalleri, Nature **449**, 72 (2007).

[20] T. Kawamoto, Y. Asai, and S. Abe, Phys. Rev. B **60**, 12990 (1999).

[21] T. Kawamoto, Y. Asai, and S. Abe, Phys. Rev. Lett. **86**, 348 (2001).

[22] H. Ohnishi, and K. Nasu, Phys. Rev. B **79**, 054111 (2009).

[23] J. Kanasaki, E. Inami, K. Tanimura, H. Ohnishi, and K. Nasu, Phys. Rev. Lett. **102**, 087402 (2009).

[24] M. Nishino and S. Miyashita, Phys. Rev. B **88**, 014108/1-14 (2013).

[25] M. Nishino, C. Enochescu, S. Miyashita, P. A. Rikvold, K. Boukheddaden, and F. Varrel, Sci. Rep. **1**, 162/1-5 (2011).

[26] M. Nishino, C. Enachescu, S. Miyashita, K. Boukheddaden, and F. Varret, Phys. Rev. B **82**, 020409 (2010).

[27] H. Aoki, N. Tsuji, M. Eckstein, M. KOllar, T. Oka, and P. Werner, Rev. Mod. Phys. **86**, 779-837 (2014).

[28] O. Sato, J. Photochemistry and Photobiology C: Photochemistry Reviews, **5**, 203-223 (2004).

[29] O. Sato, Acc. Hem. Res. **36**, 692-700 (2003).

[30] O. Sato, J. Tao, and Y. Z. Zhang, Angew. Chem. Int. Ed. **46**, 2152-2187 (2007).

[31] N. Yamada, E. Ohno, K. Nishiuchi, N. Akahira, and M. Takao, J. Appl. Phys. **69**, 2849-2856 (1991).

[32] A. V. Kolobov, P. Fons, A. I. Frenkel, A. L. Ankudinov, J. Tomonaga, and T. Uruga, Nat. Mater. **3**, 703-708 (2004).

[33] O. A. Aktsipetrov, A. A. Fedyanin, A. V. Melnikov, E. D. Mishima, and T. V. Murzina, Jpn. J. Appl. Phys. **37**, 122-127 (1998).

[34] M. Irie, T. Fukaminato, T. Sasaki, N. Tamai, and T. Kawai, Nature **420**, 759-760 (2002).

[35] P. Gülich, A. Hauser, and H. Spiering, Angew. Chem. Int. Ed. Engl. **33**, 2024-2054 (1994).

[36] O. Kahn and C. J. Martinez, Science **279**, 44-48 (1998).

[37] M. Verdaguer, Science **272**, 698-699 (1996).

[38] H. Tokoro, T. Matsuda, T. Nuida, Y. Moritomo, K. Ohoyama, E. D. L. Dangui, K. Boukheddaden, and S. Ohkoshi, Chem. Mater. **20**, 423-428 (2008).

[39] S. Ohkoshi and H. Tokoro, Acc. Chem. Res. **45**, 1749-1758 (2012).

[40] O. Sato, T. Iyoda, A. Fujishima, K. Hashimoto, Science **272**, 704 (1996).

[41] O. Sato, Y. Einaga, T. Iyoda, a. Fujishima, and K. Hashimoto, J. Electrochim. Soc **144**, 1 (1997).

[42] O. Sato, S. Hayami, Y. Einaga, Z.Z. Gu, Bull.Chem. Soc. Jpn. **76**, 443 (2003).

[43] S. Ohkoshi, H. Tokoro, T. Hozumi, Y. Zhang, K. Hashimoto, C. Mathonière, I. Bord, G. Rombaut, M. Vereist, C. C. dit Moulin, and F. Villain, J. Am. Chem. Soc. **128**, 270-277 (2006).

[44] F. Tuna, S. Golhen, L. Ouahab, J. P. Sutter, C. R. Chimie **6**, 377-383 (2003).

[45] Y. Umeta, H. Tokoro, N. Ozaki, and S. Ohkoshi, AIP Adv. **3**, 042133/1-6 (2013).

[46] Y. Arimoto, S. Ohkoshi, Z. J. Zhong, H. Seino, Y. Mizobe, K. Hashimoto, J. Am. Chem. Soc. **125**, 9240 (2003).

[47] R. Le Bris, C. Mathonière, J. F. Lètard, J. F. Chem. Phys. Lett. **426**, 380 (2006).

[48] S. Ohkoshi, S. Ikeda, T. Hozumi, T. Kashiwagi, K. Hashimoto, J. Am. Chem. Soc. **128**, 5320 (2006).

[49] S. Ohkoshi, Y. Hamada, T. Matsuda, Y. Tsunobuchi, and H. Tokoro, Chem. Mater **20**, 3048-3054 (2008).

[50] S. Ohkoshi, S. Takano, K. Imoto, M. Yoshikiyo, A. Namai, and H. Tokoro, Nat. Photon. **8**, 65-71 (2014).

[51] L. Egan, K. Kamenev, D. Papanikolaou, Y. Takabayashi, and S. Margadonna, J. Am. Chem. Soc. **128**, 6034-6035 (2006).

[52] S. Ohkoshi, K. Arai, Y. Sato, and K. Hashimoto, Nat. Mat. **3**, 857-861 (2004).

[53] X. Liu, Y. Moritomo, T. Matsuda, H. Kamioka, H. Tokoro, and S. Ohkoshi, J. Phys. Soc. Jpn. **78**, 1 (2009).

[54] S. Margadonna, K. Prassides, and A. N. Fitch, Angew. Chem. Int. Ed. **43**, 6316-6319 (2004).

[55] T. Mahfoud, G. Molnár, S. Bonhommeau, S. Cobo, L. Salmon, P. Demont, H. Tokoro, S. Ohkoshi, K. Boukheddaden, and A. Bousseksou, J. Am. Chem. Soc. **131**, 15049-15054 (2009).

[56] S. Ohkoshi, H. Tokoro, T. Matsuda, H. Takahashi, H. Irie, and K. Hashimoto, Angew. Chem. Int. Ed. **46**, 3238-3241 (2007).

[57] T. Matsuda, J. E. Kim, K. Ohoyama, and Y. Moritomo, Phys. Rev. B **79**, 172302 (2009).

[58] S. Ohkoshi, S. Saito, T. Matsuda, T. Nuida, and H. Tokoro, J. Phys. Chem. C **112**, 13095-13098 (2008).

[59] H. Tokoro, K. Nakagawa, K. Imoto, F. Hakoe, and S. Ohkoshi, Chem. Mater. **24**, 1324-1330 (2012).

[60] Y. Moritomo, K. Kato, A. Kuriki, M. Takata, M. Sakata, H. Tokoro, S. Ohkoshi and K. Hashimoto, J. Phy. Soc. Jpn. **71**, 9 (2002).

[61] E. J. M. Vertelman, E. Maccallini, D. Gournis, P. Rudolf, T. Bakas, J. Luzon, R. Broer, A. Pugzlys, T. T. A. Lummen, P. H. M. van Loosdrecht, and P. J. van Koningsbruggen, Chem. Mater. **18**, 1951-1963 (2006).

[62] S. Cobo, R. Fernández, L. Salmon, G. Molnár, and A. Bousseksou, Eru. J. Inorg. Chem. **2007**, 1549-1555 (2007).

[63] S. Ohkoshi, H. Tokoro, K. Hashimoto, Coord. Chem. Rev. **249**, 1830-1840 (2005).

[64] S. Ohkoshi, H. Tokoro, M. Utsunomiya, M. Mizuno, M. Abe, and K. Hashimoto, J. Phys. Chem. B **106**, 10 (2002).

[65] T. Yokoyama, H. Tokoro, S. Ohkoshi, K. Hashimoto, K. Okamoto, and T. Ota, Phys. Rev. B **66**, 184111 (2002).

[66] H. Osawa, T. Iwazumi, H. Tokoro, S. Ohkoshi, K. Hashimoto, H. Shoji, E. Hirai, T. Nakamura, S. Nanao, and Y. Isozumi, Solid State Commun. **125**, 237-241 (2003).

[67] H. Yun, T. Guodong, L. Fupei, H. Yanjun, H. Mali, J. Alloys Compd. **438**, 52-55 (2007).

[68] M. Pregelj, A. Zorko, D. Arčon, S. Margadonna, K. Prassides, H. van Tol, L. C. Brunel, A. Ozarowski, J. Magn. Magn. Mater. **316**, 680-683 (2007).

[69] K. Kato, Y. Moritomo, M. Takata, M. Sakata, M. Umekawa, N. Hamada, S. Ohkoshi, H. Tokoro, and K. Hashimoto, Phys. Rev. Lett. **91**, 25 (2003).

[70] K. Kato, Y. Moritomo, H. Tanaka, H. Tokoro, S. Ohkoshi, and M. Takata, J. Phys. Soc. Jpn. **76**, 12 (2007).

[71] M. Umekawa, N. Hamada, A. Kodama, and Y. Moritomo, J. Phys. Soc. Jpn. **73**, 2 (2004).

[72] C. Tian, E. Kan, C. Lee, and M. H. Whangbo, Inorg. Chem. **49**, 3086-3088 (2010).

[73] Y. Nanba and K. Okada, J. Phys. Soc. Jpn. **80**, 074710 (2011).

[74] H. Tokoro, S. Miyashita, K. Hashimoto, and S. Ohkoshi, Phys. Rev. B **73**, 172415 (2006).

[75] S. Ohkoshi, T. Matsuda, H. Tokoro, and K. Hashimoto, Chem. Mater **17**, 81-84 (2005).

[76] C. P. Slichter, and H. G. Drickamer, J. Chem. Phys. **56**, 5 (1972).

[77] H. Tokoro, S. Ohkoshi, T. Matsuda, T. Hozumi, K. Hashimoto, Chem. Phys. Lett. **388**, 379-383 (2004).

[78] Y. Moritomo, M. Hanawa, Y. Ohishi, K. Kato, M. Takata, A. Kuriki, E. Nishibori, M. Sakata, S. Ohkoshi, H. Tokoro, K. Hashimoto, Phys. Rev. B **68**, 144106 (2003).

[79] H. Tokoro, T. Matsuda, S. Miyashita, K. Hashimoto, and S. Ohkoshi, J. Phys. Soc. Jpn. **75**, 8 (2006).

[80] M. F. A. El-Sayed, and R. K. Sheline, J. Inorg. Nucl. Chem. **6**, 187-193 (1958).

[81] E. J. M. Vertelman, T. T. A. Lummen, A. Meetsma, M. W. Bouwkamp, G. Molnar, P. H. M. van Loosdrecht, and P. J. van Koningsbruggen, Chem. Mater **20**, 1236-1238 (2008).

[82] R. Fukaya, M. Nakajima, H. Tokoro, S. Ohkoshi, and T. Suemoto, J. Chem. Phys. **131**, 154505 (2009).

[83] E. D. Loutete-Dangui, E. Codjovi, H. Tokoro, P. R. Dahoo, S. Ohkoshi, and K. Boukheddaden, Phys. Rev. B **78**, 014303 (2008).

[84] S. Ohkoshi, T. Nuida, T. Matsuda, H. Tokoro, and K. Hashimoto, J. Mater. Chem. **15**, 3291-3295 (2005).

[85] Y. Moritomo, A. Kuriki, K. Ohoyama, H. Tokoro, S. Ohkoshi, K. Hashimoto and N. Hamada, J. Phys. Soc. Jpn. **72**, 2 (2003).

[86] H. Tokoro, and S. Ohkoshi, Appl. Phys. Lett. **93**, 021906 (2008).

[87] H. Tokoro, T. Matsuda, K. Hashimoto, and S. Ohkoshi, J. Appl. Phys **97**, 10M508/1-3 (2005).

[88] T. Suemoto, K. Ohki, R. Fukaya, M. Nakajima, H. Tokoro, and S. Ohkoshi, J. Lumin. **129**, 1775-1778 (2009).

[89] R. Fukaya, A. Asahara, S. Ishige, M. Nakajima, H. Tokoro, S. Ohkoshi, and T. Suemoto, J. Chem. Phys. **139**, 084303/1-7 (2013).

[90] A. Asahara, M. Nakajima, R. Fukaya, H. Tokoro, S. Ohkoshi, and T. Suemoto, Acta Physica Polonica A **121**, 375-378 (2012).

[91] H. Watanabe, S. Ishige, A. Asahara, H. Tokoro, S. Ohkoshi, and T. Suemoto, J. Lumin. **152**, 108-111 (2014).

[92] H. Kamioka, Y. Moritomo, W. Kosaka and S. Ohkoshi, Phys. Rev. B **77**, 180301 (2008).

[93] H. Kamioka, Y. Moritomo, W. Kosaka and S. Ohkoshi, J. Phys. Soc. Jpn. **77**, 9 (2008).

[94] W. Kosaka, M. Tozawa, K. Hashimoto, S. Ohkoshi, Inorg. Chem. Commun. **9**, 920-922 (2006).

[95] A. Asahara, M. Nakajima, R. Fukaya, H. Tokoro, S. Ohkoshi, and T. Suemoto, Phys. Rev. B **86**, 195138/1-9 (2012).

[96] A. Asahara, M. Nakajima, R. Fukaya, H. Tokoro, S. Ohkoshi, and T. Suemoto, Phys. Stat. Sol. (b) **248**, 491-494 (2011).

[97] K. Ishida and K. Nasu, Phys. Lett. A **378**, 382-387 (2014).

[98] T. Suemoto, H. Nagase, M. Nakajima, M. Isobe and Y. Ueda, J. Phys.: Condens. Matter **19**, 076207 (2007).

[99] A. Kirilyuk, A. V. Kimel and T. Rasing, Rev. Mod. Phys. **82**, 2731 (2011).

[100] O. Carp, C. L. Huisman, and A. Reller, Prog. Solid State Ch. **32**, 33-177 (2004).

[101] H. J. Zeiger, T.K. Cheng, E. P. Ippen, J. Vidal, G. Dresselhaus, and M. S. Dresselhaus, Phys. Rev. B **54**, 105-123 (1996).

[102] T. K. Cheng, L. H. Acioli, J. Vidal, H. J. Zeiger, G. Dresselhaus, M. S. Dresselhaus, and P. Ippen, Appl. Phys. Lett. **62**, 1901 (1993).

[103] M. Watanabe, M. Miyahara, and K. Tanaka, J. Phys.: Conference Series **148**, 012017 (2009).

[104] M. Watanabe, W. Ueno, and T. Hayashi, J. Lumin. **122**-**123**, 393-395 (2007).

[105] M. Abbate, R. Potze, G. A. Sawatzky, H. J. Lin, L. H. Tjeng, C. T. Chen, D. Teehan, and T. S. Turner, Phys. Rev. B **51**, 10150-10153 (1995).

[106] S. Ohkoshi, Y. Tsunobuchi, T. Matsuda, K. Hashimoto, A. Namai, F. Hakoe, and H. Tokoro, Nat. Chem. **2**, 539 (2010).

[107] R. Makiura, Y. Takabayashi, A. N. Fitch, H. Tokoro, S. Ohkoshi, and K. Prassides, Chem. Asian J. **6**, 1886-1890 (2011).

[108] T. Nasu, H. Tokoro, K. Tanaka, F. Hakoe, A. Namai, and S. Ohkoshi, IOP Conf. Series: Materials Science and Engineering **54**, 012008/1-8 (2014).

[109] S. Ohkoshi, S. Sakurai, J. Jin, and K. Hashimoto, J. Appl. Phys. **97**, 10K312 (2005).

[110] R. Liu and J.-X. Shang, Modelling Simul. Mater. Sci. Eng. **20**, 035020 (2012).

[111] R. Liu, J.X. Shang, and F.H. Wang, Comput. Mater. Sci. **81**, 158-162 (2014).

[112] A. O.-Hamouda, H. Tokoro, S. Ohkoshi, and E. Freysz, Chem. Phys. Lett. **608**, 106-112 (2014).

[113] R.F. Bartholomew and D.R. Frankl, Phys. Rev. **187**, 828 (1969).

[114] M. Onoda, J. Sol. Stat. Chem. **136**, 67-73 (1998).

[115] C. N. R. Rao, S. Ramdas, R. E. Loehman, and J. M. Hong, J. Sol. Stat. Chem **3**, 83-88 (1971).

[116] L. K. Keys and L. N. Mulay, Appl. Phys. Lett. **9**, 248 (1966).

[117] S. Åsbrink and A. Magnéli, Acta Cryst. **12**, 575 (1959).

[118] W. H. Zachariasen, J. Less-Common Metals **62**, 1-7 (1978).

[119] J. F. Houlihan and L. N. Mulay, Phys. Stat. Sol. (b) **65**, 513 (1974).

[120] J. F. Baumard, D. Panis and A. M. Anthony, J. Sol. Stat. Chem. **20**, 43-51 (1977).

[121] N. Stem, E. F. Chinaglia, S. G. dos S. Filho, Mater. Sci. and Eng. B **176**, 1190-1196 (2011).

[122] P. Kubelka, J. Opt. Soc. Am. **38**, 448 (1948).

[123] P. H. Siegel, IEEE Trans. Microw. Theory Techn. **50**, 910-928 (2002).

[124] B. Ferguson, and X.-C. Zhang, Nat. Mater. **1**, 26-33 (2002).

[125] D. Grischkowsky, S. Keiding, M. van Exter, and Ch. Fattinger, J. Opt. Soc. Am. B **7**, 2006-2015 (1990).

[126] N. Kida, M. Hangyo, and M. Tonouchi, Phys. Rev. B **62**, R11 965-968 (2000).

[127] N. V. Smith, Phys. Rev. B **64**, 155106/1-6 (2001).

[128] J. L.-Hughes, and T.-I. Jeon, J. Infrared Millim. Te. **33**, 871/1-54 (2012).

[129] F. A. Hegmann, D. G. Cooke, and M. Walther, Proceedings of Optical Terahertz Science and Technology (OTST), Florida, Optical Society of America, p. TuA1 (2007).

[130] D. G. Cooke, A. N. MacDonald, A. Hryciw, J. Wang, Q. Li, A. Meldrum, and F. A. Hegmann, Phys. Rev. B **73**, 193311/1-4 (2006).

[131] T. L. Cocker, L. V. Titova, S. Fourmaux, H. -C. Bandulet, D. Brassard, J. -C. Kieffer, M. A. El Khakani, and F. A. Hegmann, Appl. Phys. Lett. **97**, 221905/1-3 (2010).

[132] T. L. Cocker, L. V. Titova, S. Fourmaux, G. Holloway, H. -C. Bandulet, D. Brassard, J. -C. Kieffer, M. A. El Khakani, and F. A. Hegmann, Phys. Rev. B **85**, 155120/1-11 (2012).

[133] J. B. Baxter, and C. A. Schmuttenmaer, J. Phys. Chem. B **110**, 25229-25239 (2006).

[134] M. Walther, D. G. Cooke, C. Sherstan, M. Hajar, M. R. Freeman, and F. A. Hegmann, Phys. Rev. B **76**, 125408/1-9 (2007).

[135] M. C. Beard, J. L. Blackburn, and M. J. Heben, Nano Lett. **8**, 4238-4242 (2008).

[136] T. Unuma, K. Fujii, H. Kishida, and A. Nakamura, Appl. Phys. Lett. **97**, 033308/1-3 (2010).

[137] J. Kim, I. Maeng, J. Jung, H. Song, J.-H. Son, K. Kim, J. Lee, C.-H. Kim, G. Chae, M. Jun, Y. Hwang, S. J. Lee, J.-M. Myong, and H. Choi, Appl. Phys. Lett. **102**, 011109/1-4 (2013).

[138] H. Němec, P. Kužel, and V. Sundström, Phys. Rev. B **79**, 115309/1-7 (2009).

[139] K. Shimakawa, T. Itoh, H. Naito, and S. O. Kasap, Appl. Phys. Lett. **100**, 132102/1-3 (2012).

[140] L. K. Keys, J. Phys. Soc. Jpn. **23**, 478-479 (1967).

[141] A. Asahara, H. Watanabe, H. Tokoro, S. Ohkoshi, and T. Suemoto, Phys. Rev. B **90**, 014303/1-7 (2014).

[142] K. Tanimura and I. Akimoto, J. Lumin. **94-95**, 483 (2001).

[143] M. Fiebig, K. Miyano, Y. Tomioka, and Y. Tokura, Appl. Phys. B **71**, 211 (2000).

[144] M. Nakajima, N. Takubo, Z. Hiroi, Y. Ueda, and T. Suemoto, J. Lumin. **129**, 1802 (2009).

Related Publications

1. <u>A. Asahara</u>, H. Watanabe, H. Tokoro, S. Ohkoshi, and T. Suemoto, "Ultrafast dynamics of photoinduced semiconductor-to-metal transition in the optical switching nano-oxide Ti_3O_5", Phys. Rev. B **90**, 014303/1-7 (2014).

2. <u>A. Asahara</u>, M. Nakajima, R. Fukaya, H. Tokoro, S. Ohkoshi, and T. Suemoto, "Ultrafast dynamics of reversible photoinduced phase transitions in rubidium manganese hexacyanoferrate investigated by midinfrared CN vibration spectroscopy", Phys. Rev. B **86**, 195138/1-9 (2012).

3. <u>A. Asahara</u>, M. Nakajima, R. Fukaya, H. Tokoro, S. Ohkoshi, and T. Suemoto, "Photo-induced phase switching dynamics in $RbMn[Fe(CN)_6]$ probed by accumulation free mid-infrared spectroscopy", Phys. Stat. Sol. (b) **248**, 491-494 (2011).

4. T. Suemoto, R. Fukaya, <u>A. Asahara</u>, M. Nakajima, H. Tokoro, and S. Ohkoshi, "Dynamics of photoinduced phase transitions in hexacyanoferrate studied by infrared and Raman spectroscopy", Phys. Stat. Sol (b) **248**, 477-481 (2011).

Acknowledgments